Mechanical Properties of Perovskite and Related Oxides for Energy Conversion Devices

著者	Kimura　Yuta
学位授与機関	Tohoku University
学位授与番号	11301甲第16519号
URL	http://hdl.handle.net/10097/61330

博士学位論文

Mechanical Properties of Perovskite and Related Oxides for Energy Conversion Devices
(エネルギー変換デバイス用ペロブスカイト関連酸化物の機械的特性)

東北大学大学院環境科学研究科
環境科学専攻
学籍番号　B2GD1202
氏名　　　　木村　勇太

Contents

Chapter 3 Influence of oxygen defects on the mechanical properties of perovskite and related oxides…69

Chapter 4 Influence of ferroelasticity on the mechanical properties of perovskite and related oxides…83

Chapter 1

General introduction

1.1 Current energy trend in the world

Our energy utilization is rapidly increasing year by year. Moreover, most of the energy we use is fossil origin. This is because fossil fuels are still the most inexpensive and most convenient energy sources [1.1]. Figure 1.1 (a) and (b) clearly show these facts [1.2]. The world total energy supply has doubled in four decades since 1973 and more than 80 % of our energy comes from fossil fuel. In the future, the total rate of the energy utilization can be further accelerated, because of the current intense effort of less developed countries to catch up with developed ones, and the rapid growth in the planetary population. This can present difficult problems in many aspects, *e.g.* economy, politics, and environment. Most of the easily accessible sources of oil and gas have already been tapped and thus the cost to extract the leftover will be progressively more expensive. Also, most of the fuel used by developed countries is imported. In Japan, the dependence on foreign fossil fuel has been increased after the great east Japan earthquake and it accounts for 92.2% in 2012 [1.3]. This is because the dependence on nuclear energy has been decreased after the Fukushima nuclear accident. Therefore, in the future, the energy security can be a significant problem for nations poor in natural resources. And most importantly, the increase in the energy utilization contributes to significant global warming. The IPCC fifth assessment report has concluded that it is extremely likely that human influence has been the dominant cause of the observed warming since the mid-20th century, and continued emissions of greenhouse gases will cause further warming [1.4]. Thus, setting aside the political correctness, the technologies to reduce the concentration of atmospheric greenhouse gases are highly required in order to prevent the global warming. This can, in principle, be achieved by reducing emissions or by preventing emitted greenhouse gases from releasing into the air. Emissions can be reduced by decreasing the energy consumption, by employing alternative energy sources, by increasing the efficiency of energy use, and by switching to fuels that yield more energy per unit amount of carbon emitted [1.1].

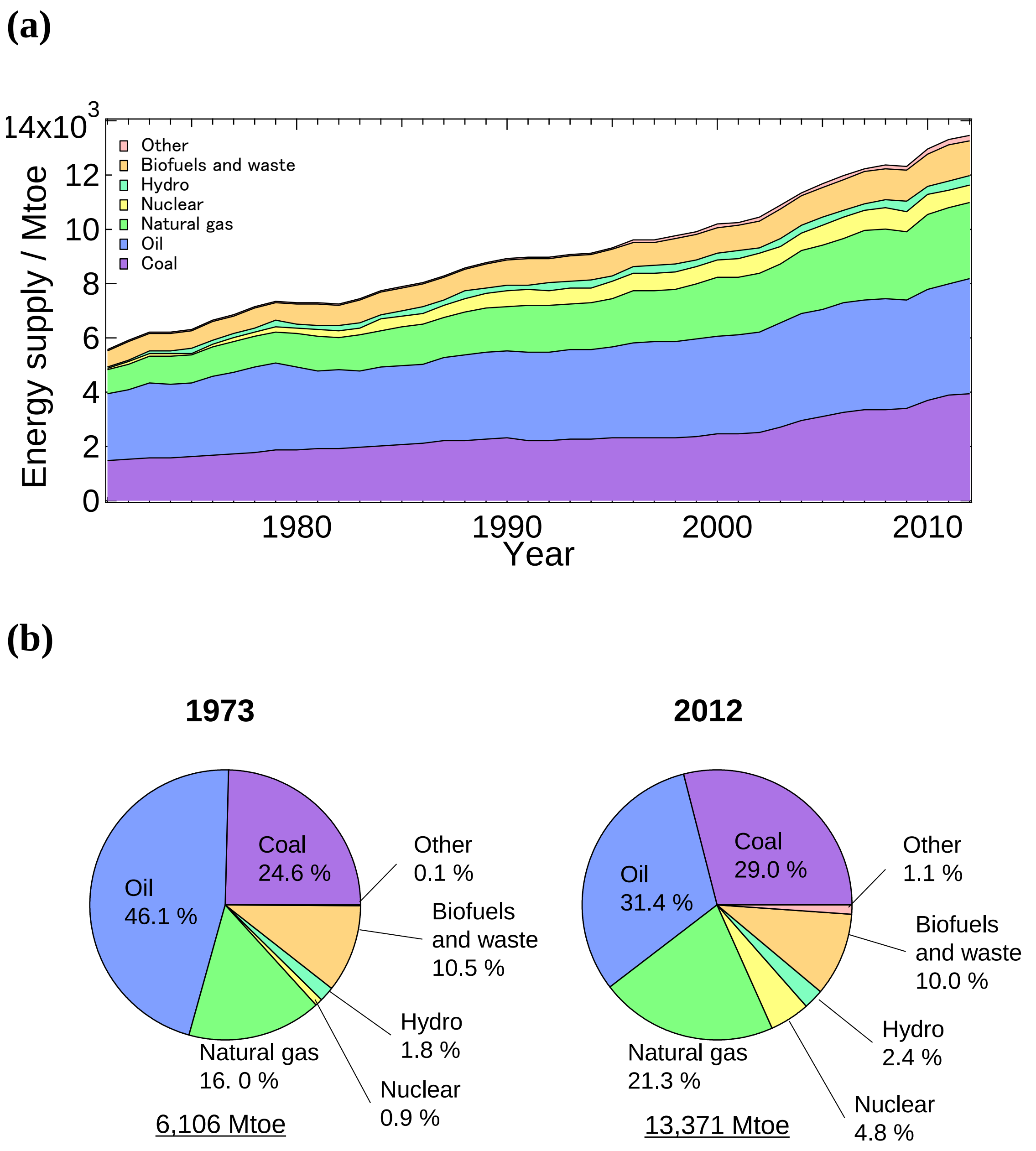

Fig.1.1 (a) the world total primary energy supply from 1973 to 2012 and (b) the fuel shares of world total primary energy supply in 1973 and 2012 [1.2].

1. 2. High temperature energy conversion devices

One of the promising technologies which meet the above need is the high temperature energy conversion devices. Whereas mechanical heat engines generally convert the heat, which is released by the combustion of a chemical substance, into mechanical energy, the high temperature energy conversion devices such as fuel cells convert chemical energy directly into electricity. Thus this conversion generally has higher efficiency than mechanical heat engines without the limitation of the Carnot efficiency [1.5]. Also, hydrogen is expected to be an alternative energy carrier of the next generation. High temperature energy conversion devices such as fuel cells, solid oxide electrolyzer, and gas separation membranes can play a central role in the future hydrogen base energy system [1.6].

In this section, the principles of some high temperature energy conversion devices are briefly reviewed.

Fuel cells

Fuel cells are the energy conversion devices which directly produce electricity by an electrochemical reaction between a fuel and an oxidant [1.5]. As previously mentioned, the efficiency of the fuel cells is not limited by the Carnot efficiency. Thus the fuel cells generally have high energy conversion efficiency. Furthermore, compared with conventional power generation devices, fuel cells have several merits such as minimal siting restriction, potential for cogeneration, and much lower production of pollutants [1.5].

Figure 1.2 shows the schematic diagram of a single fuel cell. A fuel cell consists of cathode, anode, and electrolyte. Fuel is fed to the anode. Then the fuel is oxidized and simultaneously electrons are released to the external circuit. On the cathode side, oxidant is reduced and electrons are accepted from the external circuit. The electrolyte conducts ions between the anode and cathode. The fuel cells can be classified according to the electrolyte material. So far, aqueous alkaline solution, phosphoric acid, molten carbonate, polymer membrane, and solid oxides have been used as an electrolyte of the fuel cells [1.1].

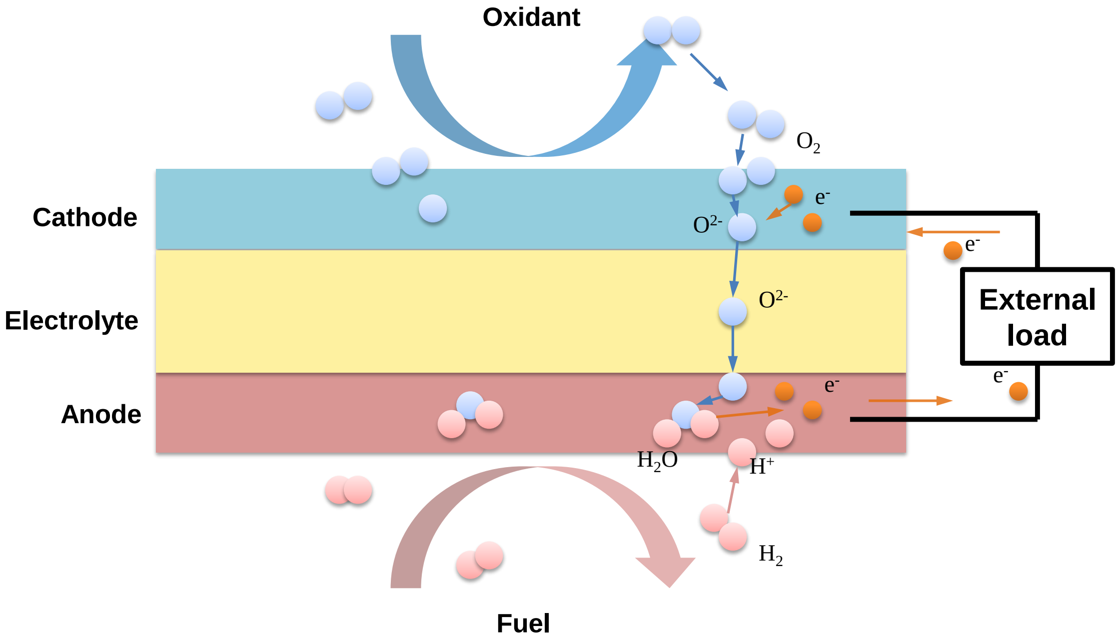

Figure 1.2 Schematic diagram of a single fuel cell

Solid oxide fuel cells (SOFCs)

The fuel cell whose electrolyte is a solid oxide, namely, solid oxide fuel cell (SOFC) has several distinct advantages compared with other types of fuel cells. For instance, SOFCs do not need to use precious materials and liquid. Moreover, SOFCs are generally operated at high temperatures. This high temperature operation promotes rapid reaction kinetics, enables internal reforming of hydrocarbon fuels, and also enables us to utilize high quality waste heat which is suitable for congeneration [1.5]. The fuel cell combined cycle with a gas turbine is regarded to be able to achieve the efficiency of 70 % [1.5]. Therefore, SOFCs can be simple and more efficient than the other types of the fuel cells and many other technologies [1.5]. Also, they can cover wide range of power output and can be applied from medium scale power generation systems to small generators for household use (Fig. 1. 3) [1. 7].

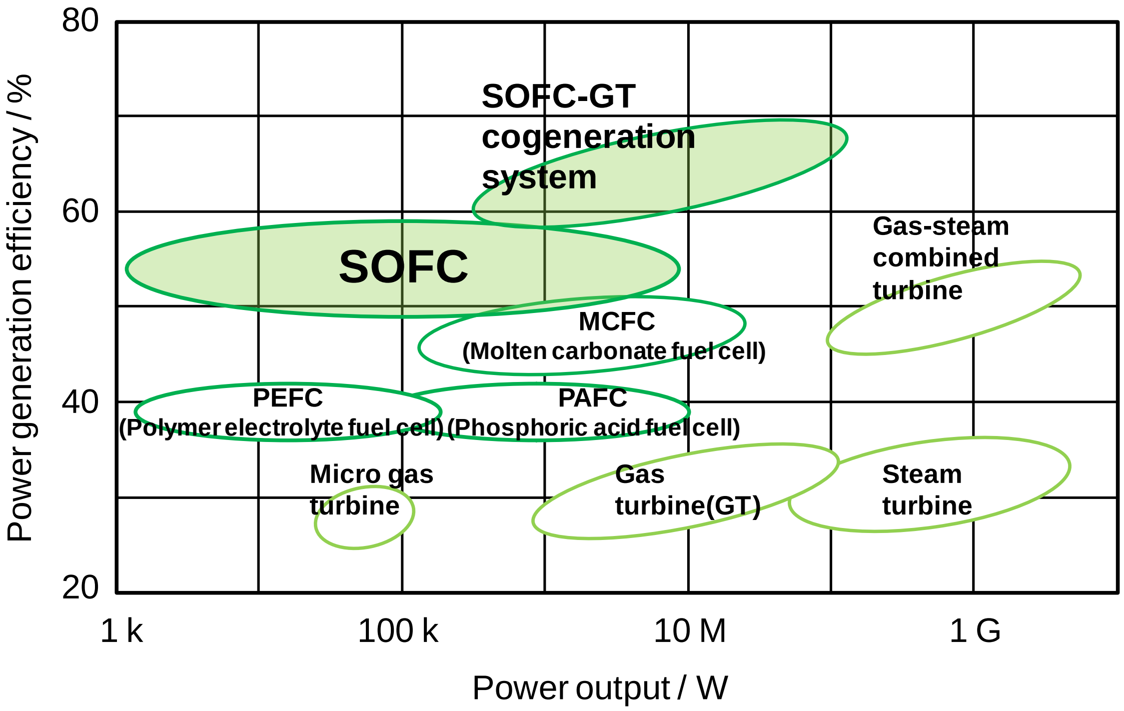

Fig. 1.3 A comparison of efficiencies of various power generation systems [1. 7].

Solid oxide electrolyzer cells (SOECs)

Solid oxide electrolyzer cell is a device which converts water and DC electricity into gaseous hydrogen and oxygen, that is to say, the reverse of an SOFC [1.6, 1.8]. Thus the fundamental components of a single SOEC are similar to those of SOFC; cathode, anode, and electrolyte although the materials used for cathode and anode are opposite of those of SOFCs. The schematic diagram of a single SOEC is shown in Fig. 1.4. Steam is fed to the cathode. When required electrical potential is applied to the SOEC, water molecules are dissociated to form hydrogen gas and oxygen ions at the cathode - electrolyte interface. The produced hydrogen gas on the cathode side is collected. The electrolyte conducts oxygen ions from the cathode to the anode. On the anode side, the oxygen ions are oxidized to oxygen gas.

The total energy demand (ΔH) for SOEC hydrogen production is expressed as follows [1.6, 1.8];

$$\Delta H = \Delta G + T\Delta S \qquad [1.1]$$

where ΔG is the electrical energy demand (Gibbs free energy change) and $T\Delta S$ is the thermal energy demand (J/mol H_2). Figure 1.5 shows the calculated energy demands as a function of temperature [1.6, 1.8]. Although the total energy demand slightly increases with increasing temperature, the electrical energy demand more noticeably decreases with increasing temperature. Thus, the cost can be further reduced if the thermal energy demand is fulfilled by an external heat source such as nuclear power, renewable energy, or waste heat from high-temperature industrial processes [1.6, 1.8]. Therefore, SOECs can produce hydrogen at a higher chemical reaction rate with a lower electrical energy requirement, compared with low-temperature proton exchange membrane (PEM) electrolysers and alkaline electrolysers.

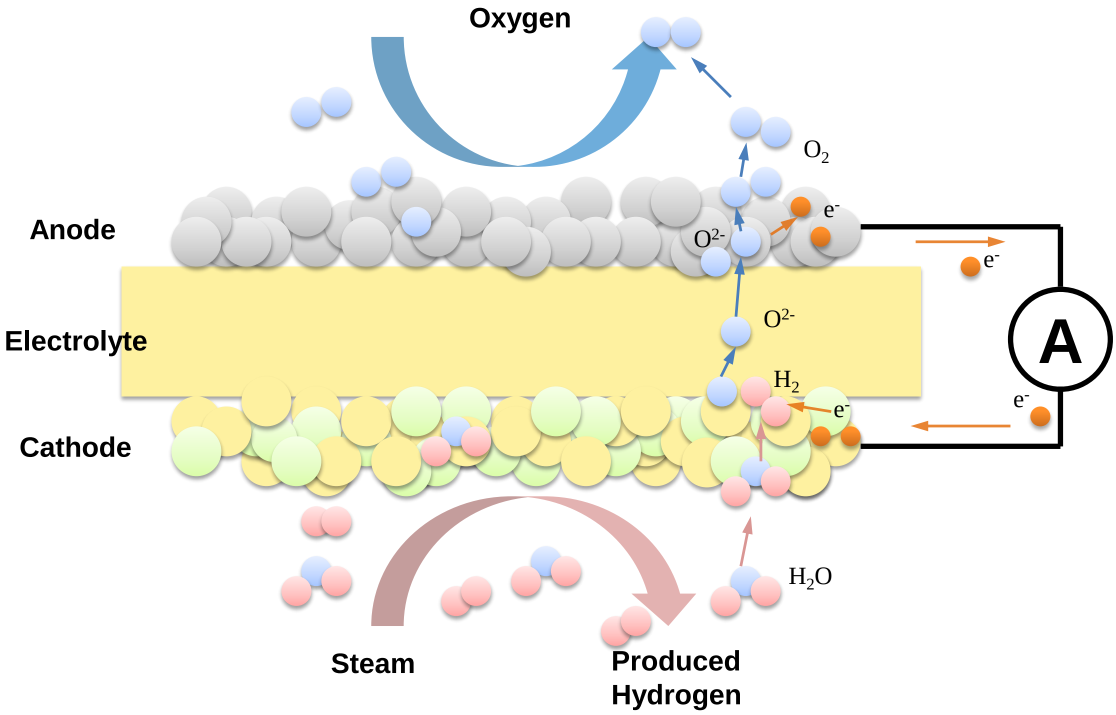

Fig. 1.4 Schematic diagram of a single solid oxide electrolyzer cell (SOEC).

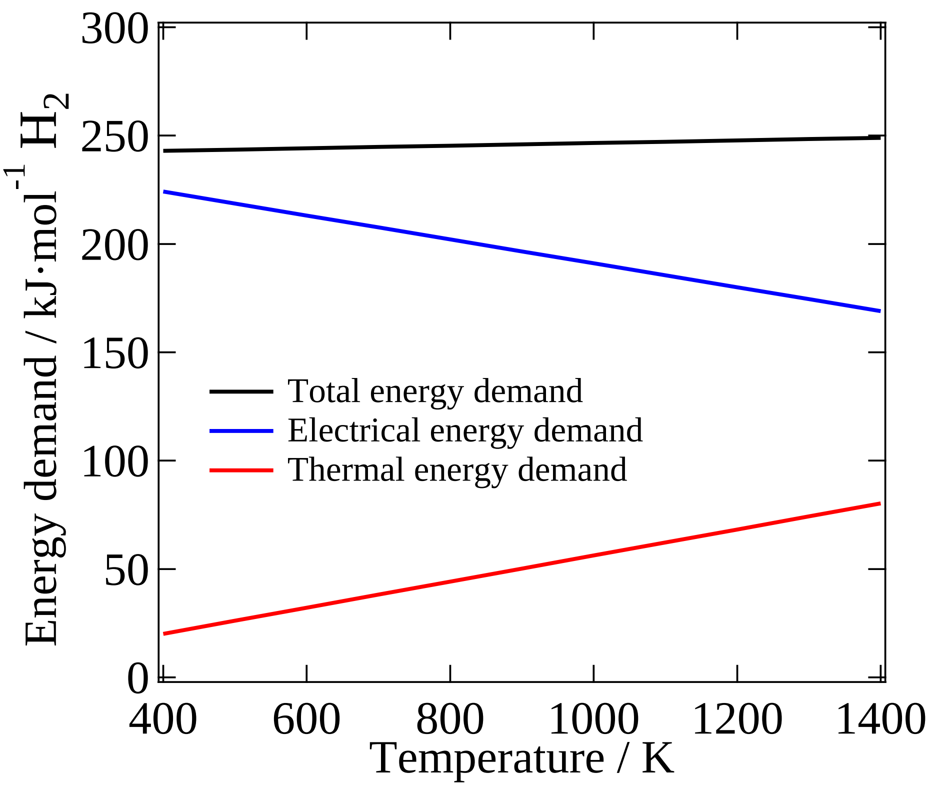

Fig. 1.5 Calculated energy demands as a function of temperature [1.6].

Gas separation membranes

Gas separation membranes can selectively separate a specific gas from a mixture gas. One of the simplest cases of the gas separation membranes is oxygen separation membranes. There are two main types of the oxygen separation membranes; pure oxygen conducting membranes and mixed ionic–electronic conducting (MIEC) membranes [1.9]. Figures 1.6 (a) and (b) show the schematic diagrams of the pure oxygen conducting membranes and the MIEC membranes, respectively. The difference between these two types of membranes is the driving force for the oxygen permeation. In both types of the membranes, the electric neutrality has to be always satisfied. Therefore, when oxygen ions move through the membrane, electrons have to move to the opposite direction to fulfill the electric neutrality. The pure oxygen conducting membranes need electrodes to transport electrons. In this system, the driving force is an electrical potential. The advantage of this system is that the amount of the generated oxygen can be controlled by changing the applied electric current. On the other hand, the MIEC membranes require no electrodes since electrons can also move in the membrane. The driving force of this system is a chemical potential gradient *i.e.* gas component partial pressure.

In addition to separating oxygen, those membranes can also be integrated in catalytic membrane reactors. For instance, the catalytic membrane reactors, which can carry out both separation and a petrochemistry process such as oxidative coupling of methane to ethylene and/or ethane (OCM), partial oxidation of methane to syngas (POM), partial oxidation of heptane to hydrogen (POH), selective oxidation of ethane to ethylene (SOE), and selective oxidation of propane to propylene (SOP), have been studied so far [1.10, 1.11]. Figure 1.7 shows the principle of the partial oxidation of methane to syngas ($CO+H_2$). In this system, oxygen ions which migrate to the fuel side partially oxidize methane and produce syngas.

Furthermore, it is possible to separate hydrogen by using the same technology with proton conducting ceramics such as $BaCe_{1-x}M_xO_3$ and $SrCe_{1-x}M_xO_3$ (M is some rare earth element) [1.12-1.14].

Therefore, gas separation membranes not only have great potential to meet the needs of the oxygen market but also have the possibility to contribute to the future hydrogen society.

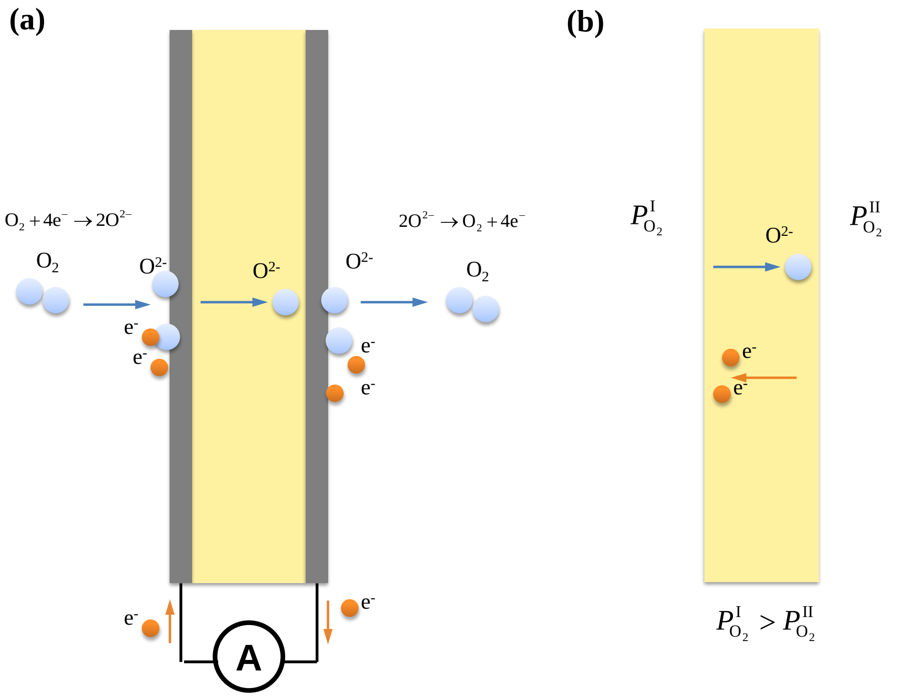

Fig.1.6 (a) Schematic diagrams of the pure oxygen conducting membranes and (b) MIEC membranes [1.9].

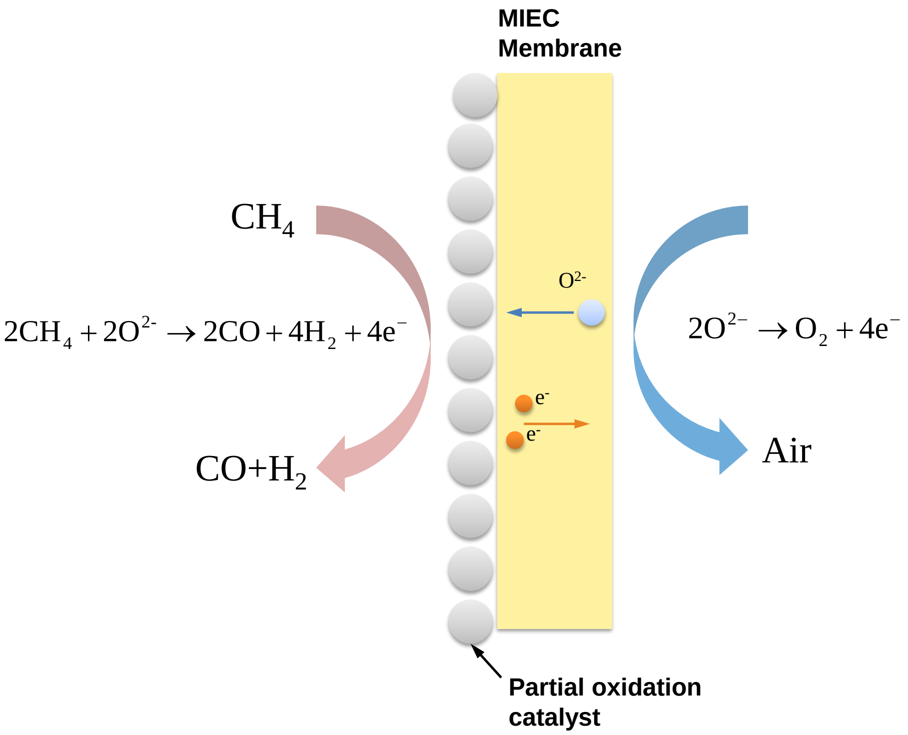

Fig.1.7 Principle of the partial oxidation of methane to syngas (CO+H_2) [1.11].

1.3 Perovskite and related oxides - Components of high temperature energy conversion devices

The components of high temperature energy conversion devices require high ionic conductivity at high temperatures. For this reason, perovskite and related oxides are commonly used for the components. The ideal cubic structure of the perovskite oxides is based on mixed fcc packing of three O^{2-} anions and one A cation [1.15]. Figure 1.8 shows the ideal cubic structure of the perovskite type oxides. The A cations are located at the corners, and the B cations at the center of the cube. The O^{2-} anions are placed at the centers of the eight cube planes. The B cations are octahedrally coordinated by O^{2-} and the A cations are 12-fold coordinated by O^{2-}. There also exist oxides which are called perovskite related oxides. One of typical perovskite related oxides are layered perovskites [1.16]. They consist of alternate stacking of the perovskite structure and another structure such as rock salt structure. As an example, Fig. 1.9 shows the crystal structure of $La_4Ni_3O_{10}$, which is the n = 3 phase of the Ruddlesden-Popper type layered perovskites, $[A_{n+1}B_nO_{3n+1}]$ [1.17]. This material is composed of the alternate stacking of the rock salt layer and *n* perovskite layers.

The perovskite and related oxides are known to have comparatively large flexibility in their composition, as long as their composition satisfies the electrical neutrality, phase equilibria, and defect equilibria [1.18]. For example, A and B cations can be partially substituted by other metal ions ($A^*$and B^*), which can be expressed with a general chemical formula, $A_{1-x}A^*_xB_{1-y}B^*_yO_3$. Also, defects of ions can be generated at any site of A and B cations and O^{2-}. Among them, oxygen defects are the most commonly observed in perovskite and related oxides. $LaCoO_3$ based perovskites are stable over a comparatively wide oxygen nonstoichiometry range [1.19]. It is known that oxygen ions can migrate via oxygen vacancies at high temperatures [1.20]. Layered perovskites, such as La_2NiO_4 can accommodate the excess oxygen in its interstitial sites. J. D. Jorgensen *et al.* found that the interstitial oxygen exist at the center of La pseudo-tetrahedron in the rock salt layer of La_2NiO_4 [1.21]. The interstitial oxygen can migrate in the oxides at high temperatures. Therefore, some perovskite and related oxides have high ionic conductivity and often applied to the electrode of fuel cells and chemical sensors [1.22, 1.23].

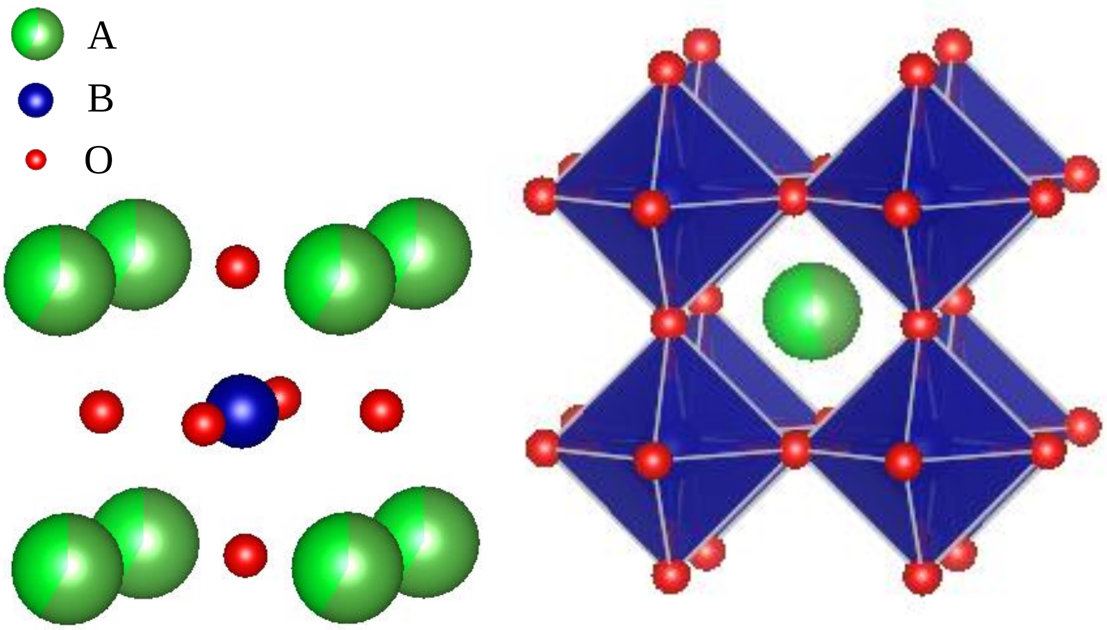

Fig.1.8 Ideal cubic structure of the perovskite type oxides.

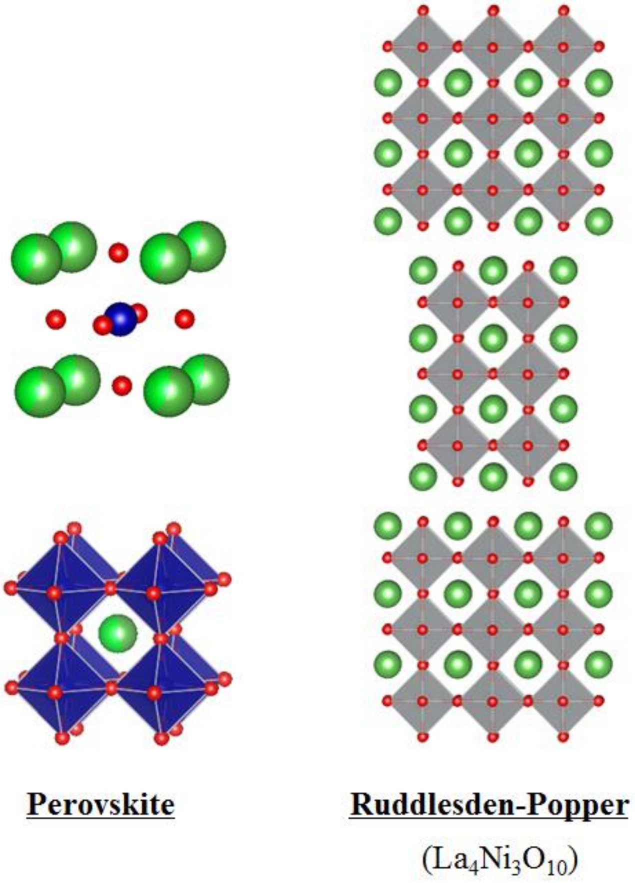

Fig. 1.9 Structures of layered perovskites, $La_4Ni_3O_{10}$, (n = 3 phase of the Ruddlesden-Popper series) [1.17].

1.4 Development of high temperature energy conversion devices - SOFCs

As mentioned in the previous section, SOFCs have the higher efficiency compared to conventional gas turbine systems and other types of fuel cells. Also, they can cover wide range of power output and can be applied to various scale systems from small generators for household use to large scale power generation plants [1. 24]. Moreover its high operating temperature makes it possible to develop a combined system with a gas turbine [1.25, 1.26]. Therefore, a great deal of efforts has been made to commercialize SOFCs throughout the world. In this section, the development status of SOFCs is briefly reviewed.

1.4.1 Development status of SOFCs in the U.S., Europe, and Japan

In the U.S., the development of advanced power generation system which is based on SOFC technology has been promoted under the Solid State Energy Conversion Alliance (SECA) program [1.27]. This program is managed by the National Energy Technology Laboratory. Since the largest domestic energy resource in the U. S. is coal, they are aiming to develop coal-fueled SOFCs for central-station (>100MW) application, which simultaneously provide for effective carbon capture and lower pollutant emissions (Hg, NO_x, and SO_x). In the private sector, Bloom Energy Corporation in the U. S. achieved the practical use of SOFCs and already shipped their SOFCs to a lot of companies such as Google, eBay, Walmart, FedEx, The Coca-Cola Company, etc.[1.28]. Their SOFC, Energy server, is a 200-kW SOFC and it has achieved the electric efficiency of over 50 % (AC net, LHV) [1.29]. In 2013, the Bloom Energy Corporation established a joint venture, Bloom Energy Japan Ltd., with SoftBank Corporation in Japan and opened up a new market in Japan [1.30].

A number of European research institutes and companies also work enthusiastically on the development of SOFCs [1.31-1.34]. Forschungszentrum Jülich in Germany, for instance, has almost twenty year history in SOFC development [1.31]. Recently, their long term tests with short stacks successfully reached 50,000h of continuous operation with a mean voltage degradation of 0.8 %/kh [1.32]. Hexis. Ltd. in Switzerland and Germany has develop Galileo 1000N, which is an SOFC-based combined heat and power system for single family homes. It has achieved total efficiency of 95% (LHV) and electrical efficiency of around 35% (AC net, LHV) [1.33]. Also, an international collaborative project, Real-SOFC, was conducted from 2004 to 2008 with twenty six European institutions, aiming at the improvement of the durability of planar SOFC stacks [1.34]. Their planar stacks successfully achieved more than 10,000 hour operation and over 100 thermal cycles and so on [1.34].

In Japan, New Energy and Industrial Technology Development Organization (NEDO) has been promoting the development project of SOFCs under cooperation with domestic companies and universities. [1. 35] From the analysis of the data collected from the demonstrative research and earlier endurance tests, [1. 36] it was revealed that the commercialization of SOFCs required a further advancement of their performances, a cost reduction and the improvement of their durability and reliability. [1.36, 1.37] Therefore, in order to overcome those challenges, the NEDO project, “Development of System and Elemental Technology on Solid Oxide Fuel Cell” were conducted for five years from

2008. [1.35, 1.38] The main theme of this project was the basic research for improving the durability and reliability of SOFCs, targeting the duration time of over 40,000 hours, the tolerability of 250-time startup and stop operations, and voltage decrease rate less 0.25 % / 1000 hours. Also it aimed at the technological development for improving practical utility. In October 2011, the first stationary SOFCs for household use, ENE-FARM type S went on sale from JX Nippon Oil and Energy Corporation [1. 39]. Following JX Nippon Oil and Energy Corporation, Osaka Gas Co., Ltd., AISIN SEIKI Co., Ltd., KYOCERA Corporation, CHOFU SEISAKUSHO Co., Ltd., and TOYOTA MOTOR Corporation began selling the stationary SOFCs on April, 2012 [1.40]. Since then, although JX Nippon Oil and Energy Corporation have decided to cease the development of SOFCs at the end of March, 2015 [1.41], the number of sales of SOFCs has been steadily increasing and it achieved a hundred thousand in 2014 [1.42]. Also, in 2014, the new model of ENE-FARM type S was released from Osaka Gas Co., Ltd., AISIN SEIKI Co., Ltd., KYOCERA Corporation, and CHOFU SEISAKUSHO Co., Ltd. [1.43]. This new model achieved cost reduction of about six hundred thousand yen, and it enabled the self-sustained operation in case of power outage [1.43]. The SOFCs are expected to continuously become prevailed in the future all over the world.

1.4.2 Challenges for further commercialization of SOFCs

In the NEDO project, “Development of System and Elemental Technology on Solid Oxide Fuel Cell” from 2008 to 2013, the degradation factors of six types of cell stacks (including sealless tubular cells made by TOTO and disk-type planer cells made by Mitsubishi Materials Corp. and Kansai Electric Power Co.) were precisely examined after durability tests. Table 1.1 summarizes the six types of cell stacks, which was taken from literature [1.44]. This examination was conducted by means of thermodynamic, chemical and mechanical analysis under the cooperation in academia, industry and AIST [1.44, 1.45]. From this examination, the specific degradation mechanisms in each cell stacks, and also the general degradation factors in different types of the cell stacks were successfully identified [1.44, 1.45]. For example, it was revealed that NiO which was dissolved in YSZ electrolyte promoted the phase transition of YSZ from cubic to tetragonal symmetry and led to the conductivity lowering [1.46-1.48]. As an example of the specific degradation mechanisms, the Cr poisoning in cathode was found to be the main degradation factor of the segment-in-series cells by Mitsubishi Heavy Industries, Ltd. (MHI) [1.49]. Cr was mixed in from alloy tubes and deposited on the three phase boundary (TPB) areas. After preventing Cr from mixing into the air, the cathode performance was well improved and essentially no degradation occured [1.50]. A small amount of $LaCrO_3$ was also found at the interface between cathode and (La, Sr)(Ga, Mg)O_3 (LSGM) electrolyte in the microtubular cells by TOTO and caused the cathode degradation. Mechanical degradation was also found to be one of the strong factors in preventing the durability and reliability of SOFCs [1.44]. The mechanical degradation was caused by the stress, which was associated with the thermal and/or chemical volume expansion of components [1.44]. Therefore, in the NEDO project, the fundamental properties of the materials for SOFC components were systematically evaluated as function of temperature and oxygen partial pressure in order to predict the stress/deformation in components. The fundamental properties, which were evaluated in the project, included oxygen nonstoichiometry, chemical expansion coefficient, and mechanical properties. A part of studies in this thesis was made as a part of this project. After the examination on the degradation mechanisms in each cell stacks, the cell stacks were improved and their degradation rates were significantly suppressed. Table 1.2 shows the final degradation rate and the start and shut down degradation of each cell stack [1.45]. Indeed, the flatten-tubular cell stacks from KYOCERA Corporation, which were examined in this project, were actually employed in ENE-FARM Type S released by JX Nippon Oil and Energy Corporation in 2011 and AISHIN SEIKI Co., Ltd. [1.45]. Therefore, it can be said that this project achieved a measure of success in improving the durability and reliability of SOFCs.

On the other hand, H. Yokokawa pointed out that there appeared to be other degradation mechanisms which were still needed to be investigated [1.44]. Some degradation in cell stacks were caused by complicated interactions among various chemical and electrochemical process in SOFC stacks. Therefore, in order to more correctly predict the life time of SOFC stacks, it is necessary to model the stack behavior both locally and globally, considering the various phenomena in the stack such as overpotential, electrochemical reaction, heat, current, and stress distribution, operation history and so on. Therefore, in 2013, NEDO launched a new project “Technology Development for promoting SOFC commercialization” in order to establish a new systematic approach to predict the life time of SOFC and actually achieve the long life time [1.45].

Table 1.1 The six types of cell stacks, which were examined in the the NEDO project, “Development of System and Elemental Technology on Solid Oxide Fuel Cell” from 2008 to 2013 [1.44].

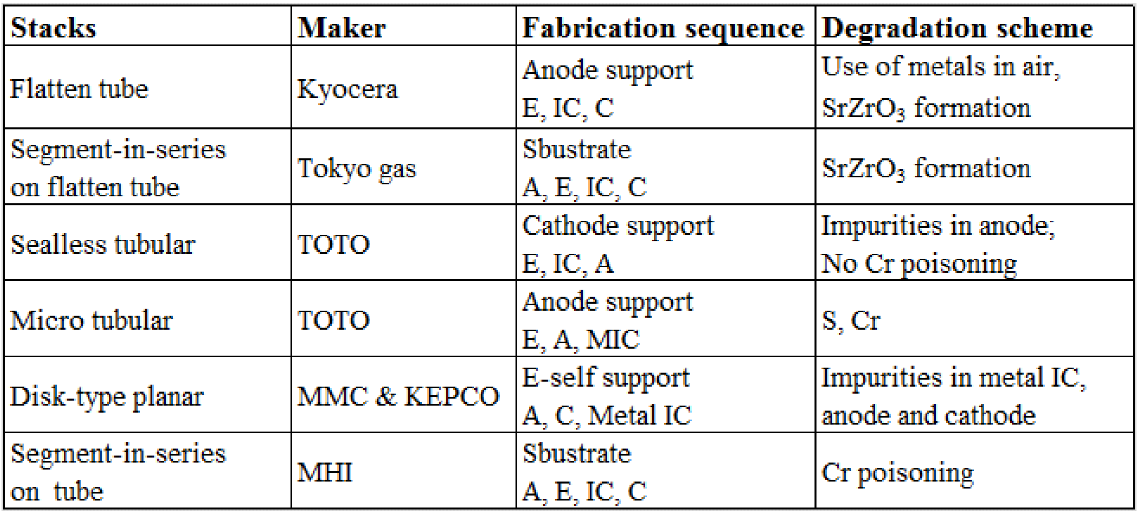

Stacks	**Maker**	**Fabrication sequence**	**Degradation scheme**
Flatten tube	Kyocera	Anode support E, IC, C	Use of metals in air, $SrZrO_3$ formation
Segment-in-series on flatten tube	Tokyo gas	Sbustrate A, E, IC, C	$SrZrO_3$ formation
Sealless tubular	TOTO	Cathode support E, IC, A	Impurities in anode; No Cr poisoning
Micro tubular	TOTO	Anode support E, A, MIC	S, Cr
Disk-type planar	MMC & KEPCO	E-self support A, C, Metal IC	Impurities in metal IC, anode and cathode
Segment-in-series on tube	MHI	Sbustrate A, E, IC, C	Cr poisoning

Table 1.2 Final degradation rate and the start and shut down degradation of six types of cell stacks [1.45].

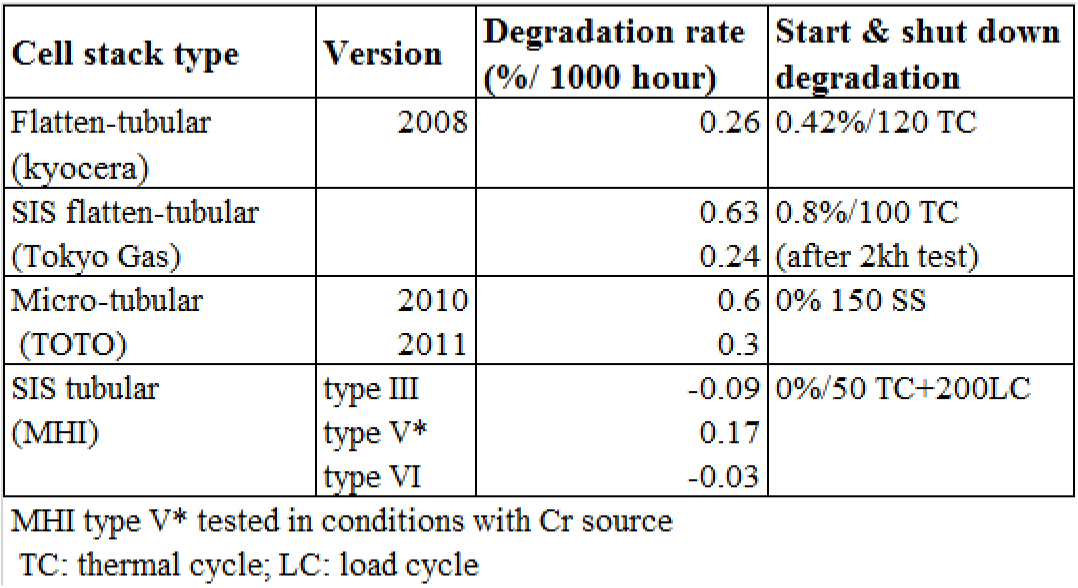

Cell stack type	**Version**	**Degradation rate (%/ 1000 hour)**	**Start & shut down degradation**
Flatten-tubular (kyocera)	2008	0.26	0.42%/120 TC
SIS flatten-tubular (Tokyo Gas)		0.63 0.24	0.8%/100 TC (after 2kh test)
Micro-tubular (TOTO)	2010 2011	0.6 0.3	0% 150 SS
SIS tubular (MHI)	type III type V* type VI	-0.09 0.17 -0.03	0%/50 TC+200LC

MHI type V* tested in conditions with Cr source

TC: thermal cycle; LC: load cycle

1.4.3 Mechanical degradation and chemomechanical coupling phenomena in SOFCs

Since SOFCs use nonstoichiometric, ionically conductive ceramic materials [1.51], chemomechanical coupling phenomena are often observed in the SOFC operating conditions. For instance, when those materials are exposed to oxygen potential gradient, their oxygen defect concentrations vary with oxygen potential. The increase/decrease of oxygen defect concentration induces the lattice expansion/shrinkage due to the change in valence of cations and the repulsive force between cations [1. 52-1.55]. Figure 1. 10 shows the oxygen nonstoichiometry of $La_{0.8}Sr_{0.2}Ga_{0.8}Mg_{0.15}Co_{0.05}O_3$ (LSGMC) as a function of oxygen partial pressure ($P(O_2)$) [1.56]. LSGMC is one of promising electrolyte materials of SOFCs because of its high ionic conductivity at intermediate temperatures [1.57]. As this figure shows, the oxygen vacancy concentration in LSGMC increases with decreasing $P(O_2)$. When LSGMC is used as an electrolyte, it is exposed to an oxygen potential gradient. This means that there is a gradient of oxygen vacancy concentration in LSGMC. Kawada *et al.* calculated the oxygen vacancy concentration profile in LSGMC under the open circuit condition and at the terminal voltage of 0.7 V, by integrating local internal transport fluxes of ions and electrons [1.58]. It was estimated that when LSGMC was used as an electrolyte and exposed to the terminal voltage of 0.7 V, the oxygen vacancy concentration, δ, at the cathode side was approximately 0.17 but it increased to approximately 0.20 at the anode side (Fig. 1. 11). As mentioned above, the increase in the oxygen vacancy concentration causes the lattice expansion. This increase in the oxygen vacancy concentration from 0.17 to 0.20 changes the lattice constant of LSGMC approximately from 3.94 to 3.95 Å [1.56]. Given this expansion is caused by the thermal expansion, it corresponds to the temperature difference of about 200 K between cathode and anode sides [1.56]. Thus the impact of the chemical lattice expansion is significant and can be a critical problem for the mechanical stability of SOFCs.

Moreover, although cathode materials are generally exposed to only air, there can still exist an oxygen potential gradient in the cathode materials due to the overpotential. The overpotential in cathode can be associated with oxygen reduction reaction. Figure 1.12 shows the several oxygen reduction reaction processes which are considered to occur in the cathode. The oxygen reduction reaction consists of several reaction processes such as (a) diffusion of oxygen molecules in a gas phase, (b) adsorption of oxygen molecules to the cathode surface, (c) dissociation of oxygen molecules, (d) diffusion of oxygen ions on the surface or in the bulk, and (e) transportation of oxygen ions to an electrolyte. Since the driving force of these reaction processes is oxygen potential, the oxygen potential varies in a cathode as schematically described in Fig. 1. 11 [1.24]. Thus there can exist an oxygen potential gradient in the cathode material. Further, in the actual cathode, the porosity forms a complicated geometry, and it makes the oxygen potential distribution more complex [1.59-1.61]. Also, there exits the triple phase boundary (TPB) of gas phase, an electrode and an electrolyte at the boundary between an electrode and an electrolyte. The oxygen reduction reaction most actively proceeds at TPB [1.62, 1.63]. Therefore, oxygen potential is considered to drastically change in the vicinity of TPB. [1.64, 1.65] Thus it is possible that even if the cathode material is exposed to the air, there can locally exist a steep oxygen potential gradient in the cathode, and hence, a steep stress gradient due to the chemical expansion. In order to model the above mentioned stress distribution, which is caused by the chemomechanical and sometimes the electro-chemo-mechanical coupling phenomena, firstly it is necessary to acquire reliable data on material properties such as the ionic and electronic conductivities, the expansion coefficients, oxygen nonstoichiometry, and the mechanical properties as functions of temperature and $P(O_2)$. However, whereas the ionic and electronic conductivities, the expansion coefficients, oxygen nonstoichiometry have been extensively studied [1.5, 1.191, 1.52, 1.53, 1.54, 1.56, 1.57], the mechanical properties of component materials, especially under operating conditions, are still poorly available.

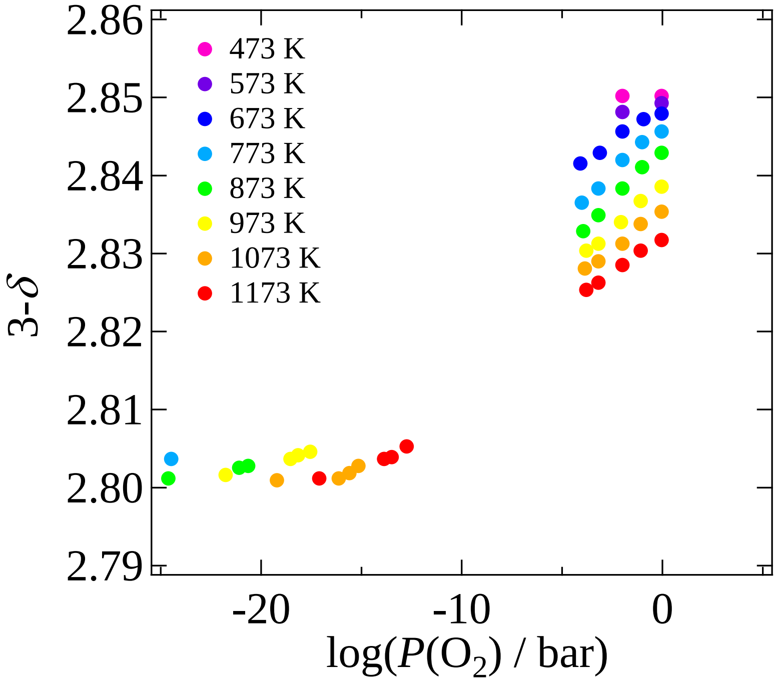

Fig. 1.10 Oxygen nonstoichiometry of $La_{0.8}Sr_{0.2}Ga_{0.8}Mg_{0.15}Co_{0.05}O_3$ (LSGMC) as a function of oxygen partial pressure ($P(O_2)$) [1.56].

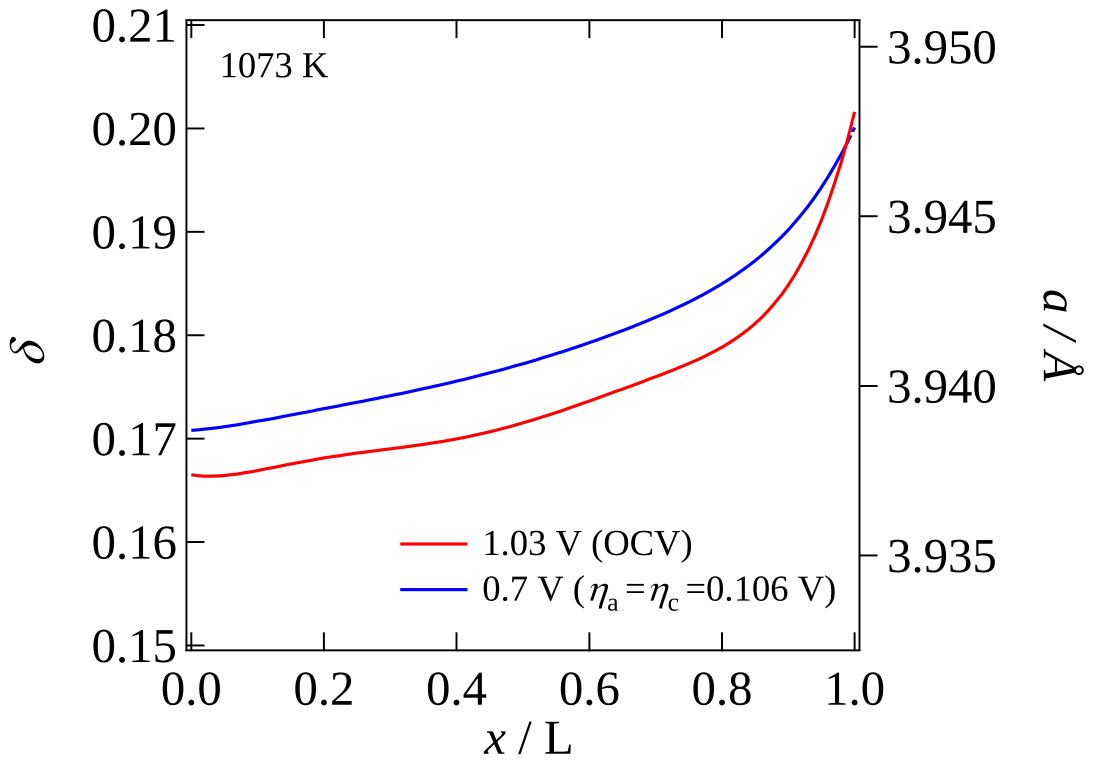

Fig. 1.11 Oxygen vacancy concentration profile in LSGMC under the open circuit condition and at the terminal voltage of 0.7 V [1.58].

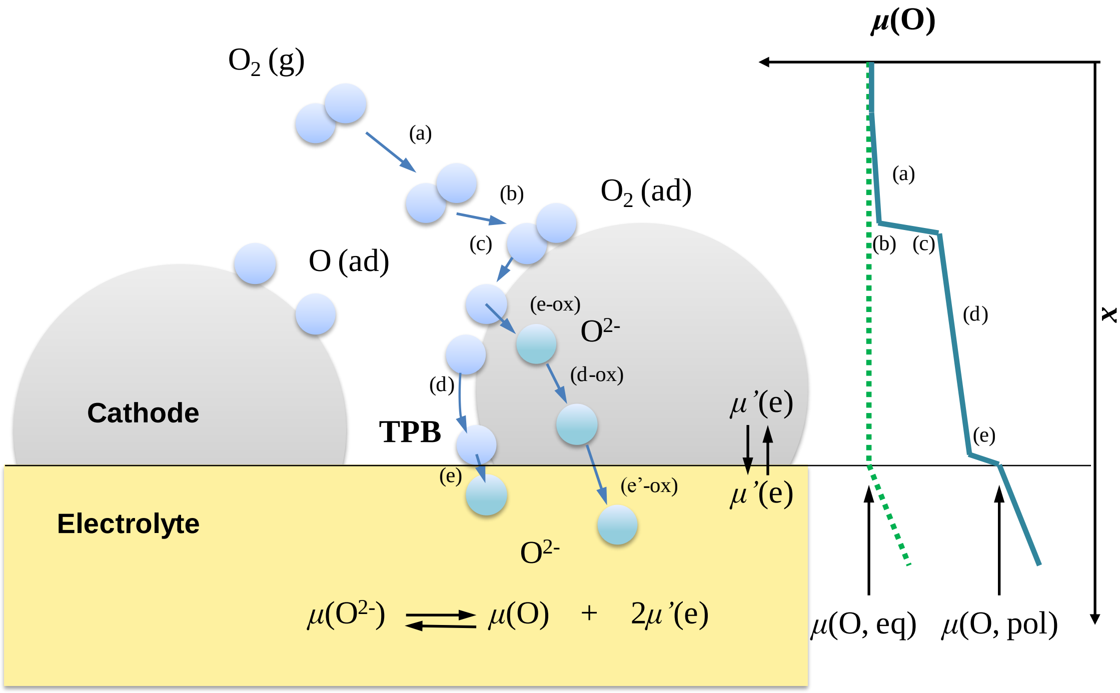

Fig. 1.12 Schematic diagram of the oxygen reaction path and oxygen potential distribution on a cathode side [1.24].

1.5 Mechanical properties of perovskite and related oxides for high temperature energy conversion devices

As mentioned above, one of the important applications of the perovskite and related oxides is high temperature energy conversion devices, such as SOFCs. However, the mechanical properties of the perovskite and related oxides, especially under operating conditions, are still poorly available. This makes it difficult to predict the mechanical degradation in SOFCs and hence obstructs the further commercialization of SOFCs. In this section, the reported mechanical properties of perovskite and related oxides for SOFC components are briefly reviewed. This section mainly focuses around the elastic modulus, which is an essential data in predicting the stress distribution in SOFCs.

1.5.1 $LaMnO_3$ based oxides

Y. Shirai systematically evaluated the temperature dependence of the Young's modulus of Sr-substituted $LaMnO_3$ based oxides, $La_{1-x}Sr_xMnO_3$ (LSM, $x = 0.2$~0.7) [1.66]. Their measurements were performed by using a resonance method with dense samples (relative density: 91.6-98.0 %) in the temperature range between 298 and 1273 K under $P(O_2)$ of 1.0 x 10^{-4} bar. Figure 1.15 shows their results. The Young's modulus of LSM with $x = 0.2$ and 0.3 gradually decreased with increasing temperature up to 673 and 1023 K, respectively. Above those temperatures, it gradually increased with increasing temperature. The Young's modulus of LSM with $x = 0.4$, 0.5, 0.6 gradually decreased with increasing temperature up to 973, 673, 423 K, respectively. Then it drastically increased above those temperatures. After the drastic increase, the Young's modulus again gradually decreased with increasing temperature. On the other hand, the Young's modulus of LSM with $x = 0.7$ gradually increased with increasing temperature up to 723 K and then slightly decreased. At further higher temperatures, it again gradually increased with increasing temperature. The temperature, at which the drastic increase in the Young's modulus of LSM with $x = 0.4$, 0.5, 0.6 was observed, agreed with the phase transition temperature from rhombohedal to cubic structure [1.67, 1.68]. Thus it is possible that the drastic increase was related with the phase transition. However, the phase transition temperatures of LSM with $x = 0.2$ and 0.3 are reported to be 1508-1598 [1.69], 1123-1273 K [1.70], respectively. Thus the temperature at which the gradual increase in the Young’s modulus was observed was not agreed with the phase transition temperature. Further, the crystal structure of LSM with x = 0.7 is cubic over the temperature range from room temperature to 1273 K [1.67]. Therefore, the gradual increase which was observed with LSM with x =0.7 at high temperatures cannot be explained by the phase transition.

S. Giraud *et al.* also evaluated the mechanical properties of LSM with x = 0.2 and with different porosities as a function of temperature in pure argon atmosphere by using impulse excitation technique (IET) [1.71]. Their results are also plotted in Fig. 1.15. LSM 1-1, LSM 2-1, LSM 3-1, and LSM 4-1 have different open and closed porosities. The open porosities of LSM 1-1, LSM 2-1, LSM 3-1, and LSM 4-1 are 29, 9, 0, and 0 %, respectively. The close porosities of those materials are 0, 2.5, 9, and 3-4 %, respectively. Thus LSM 4-1 is the densest sample and LSM 1-1 is the opposite. The absolute values of the Young’s modulus of those samples are different from each other. This difference is considered to be due to the difference in open and closed porosities. The temperature dependence of LSM is significantly different depending on their porosity. The Young’s modulus of LSM with totally or partially opened porosity (LSM 1-1 and LSM 2-1) is almost constant over the measuring temperature range. On the other hand, the Young’s modulus of LSM with a fully closed porosity (LSM 3-1 and LSM 4-1) is strongly dispersed below 873 K and not shown in Fig.1.14. Above 873 K, the Young’s modulus monotonically increased with increasing temperature in common with the results of Y. Shirai. Although they reported the peculiar temperature dependence of the Young’s modulus of LSM, they do not provide for any explanation for this behavior.

Also, it is reported that LSM and Ca-substituted $LaMnO_3$ based oxides show an elastic anomaly at around the Curie temperature, which is possibly related to the phase transition from paramagnetic to ferromagnetic phase [1.72, 1.73] or the distortion of oxygen ochtahedra [1.74].

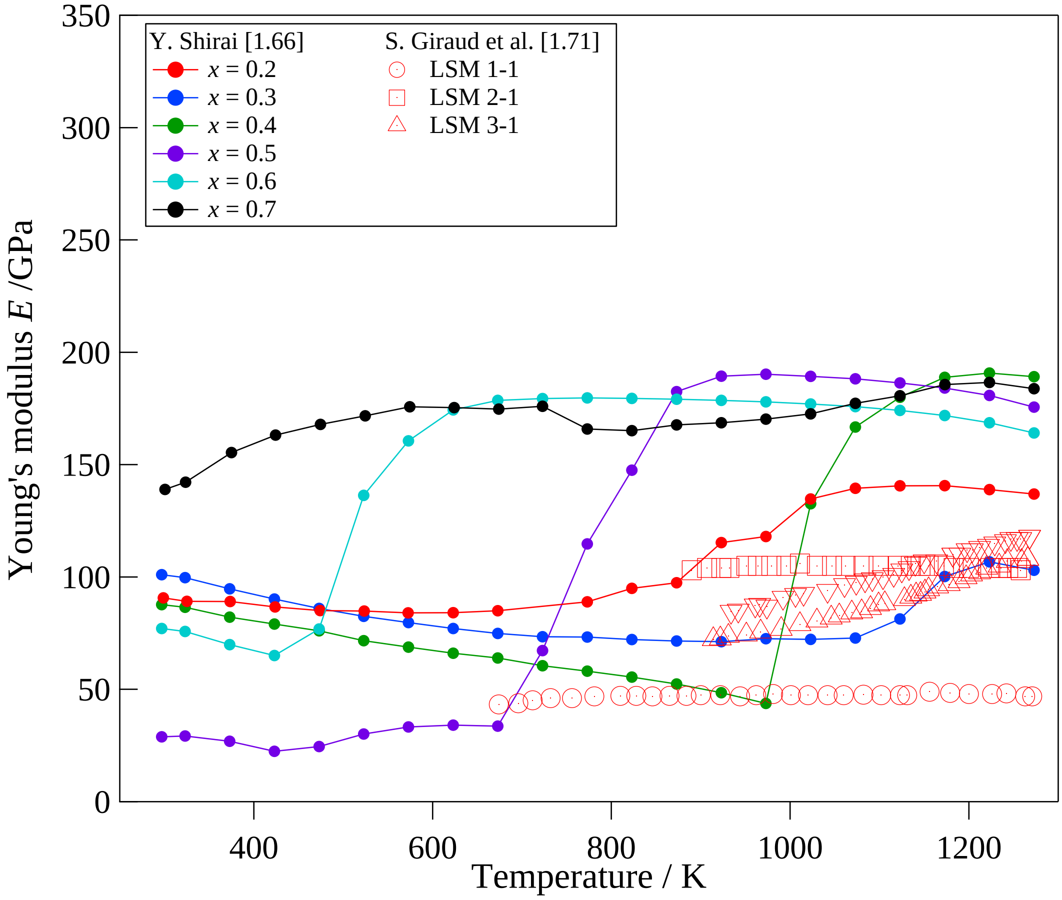

Fig. 1.13 Temperature dependence of the Young's modulus of Sr-substituted $LaMnO_3$ based oxides, $La_{1-x}Sr_xMnO_3$ (LSM, x = 0.2~0.7) [1.66] and $La_{0.8}Sr_{0.2}MnO_3$ with different open and closed porosities [1.71].

1.5.2 $LaCoO_3$ based oxides

The Young's modulus of $LaCoO_3$ has been measured by several researchers at room temperature. Figure 1.16 shows the Young's modulus of $LaCoO_3$ reported in literatures. K. Kleveland *et al.* measured the Young's modulus by uniaxial compression tests and the value is ~110 GPa [1.75]. S. Pathak *et al.* measured the Young's modulus using three different methods, namely, IET, four point bending tests, and uniaxial compression tests at room temperature and 1073 K [1.76]. In Fig.1.16, the Young's modulus measured by IET was only plotted because they believe it is the most accurate value among the values measured by the three methods [1.76]. The value measured by IET is 76 GPa at room temperature and 101 GPa at 1073 K. N. Orlovskaya *et al.* measured the Young's modulus by four point bending tests and it is 47.8 ± 7.8 GPa [1.77]. Z. Zhang *et al.* measured the Young's modulus of $LaCoO_3$ below room temperature by resonance ultrasound spectroscopy (RUS) [1.78]. The Young's modulus gradually decreases with increasing temperature and the value at around 280 K is 36.7 GPa. The difference in the value reported in the above literatures is possibly due to the porosity of the samples. The porosities of the samples of K. Kleveland *et al*. is around 7.4 % [1.75], of S. Pathak *et al.* is around 10.2 % [1.76], of N. Orlovskaya *et al.* is around 16 % [1.77], and of Z. Zhang *et al.* is around 30 % [1.78]. Thus the value of the Young's modulus is negatively correlated with the porosity.

H. L. Lein *et al.* reported the temperature dependence of the Young's modulus of 50 % Sr-substituted $LaCoO_3$ which was measured using RUS in the temperature range between 273 and 1473 K [1.79]. Over the measuring temperature range, The Young's modulus monotonically decreases with increasing temperature regardless of the measuring atmospheres.

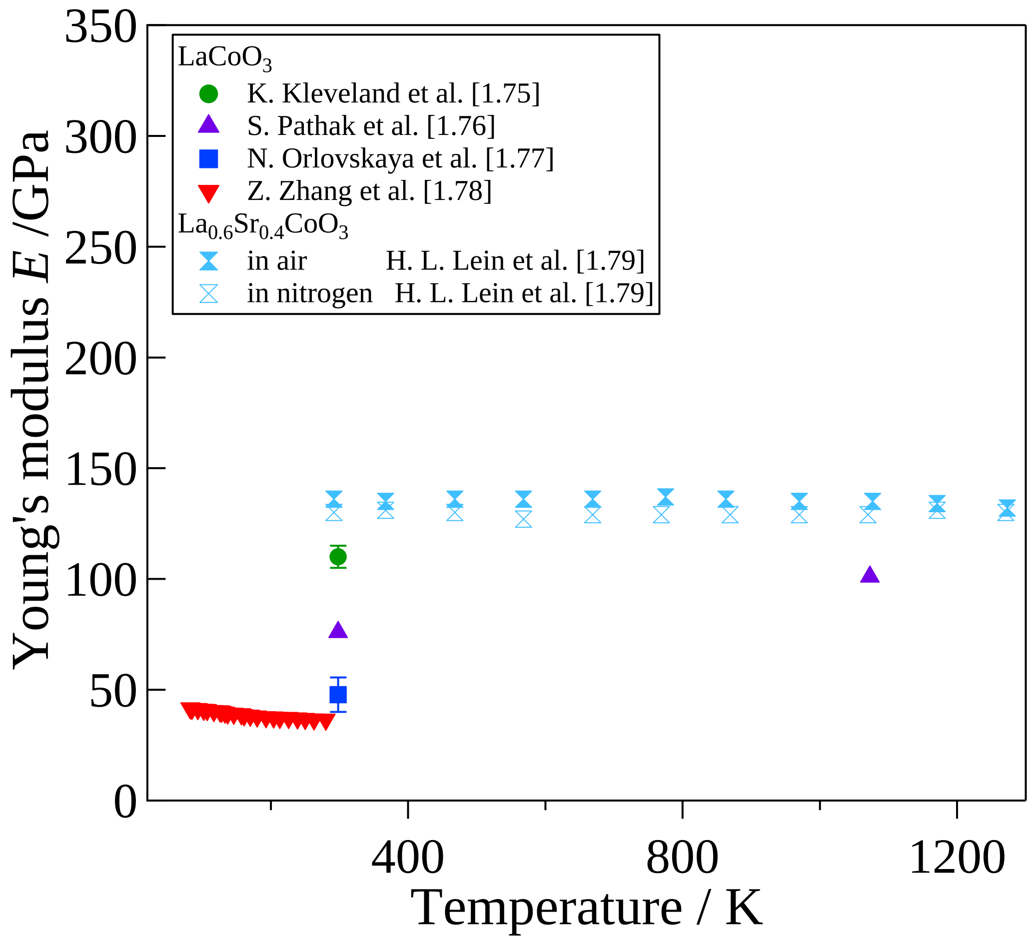

Fig. 1.14 Young's modulus of $LaCoO_3$ based oxides which are taken from literatures [1.75-1.79].

1.5.3 $LaFeO_3$ based oxides

A. Fossdal *et al.* reported the Young's modulus of $LaFeO_3$ measured by four point bending tests and uniaxial compression tests at room temperature and 1073 K [1.80]. The Young's modulus measured by the four point bending tests at room temperature is 213 ± 14 GPa while the one measured by the uniaxial compression tests is 195 ± 5 GPa, which is within the uncertainty of the one measured by the four point bending tests (Fig. 1.17). N. Orlovskaya *et al.* measured the Young's modulus of 40 % Sr-substituted $LaFeO_3$ based oxides, $La_{0.6}Sr_{0.4}FeO_3$, at room temperature by uniaxial compression tests [1.81]. They report the Young's modulus of $La_{0.6}Sr_{0.4}FeO_3$ is 131 GPa.

A. Julian *et al.* evaluated the temperature dependence of the Young's modulus of $La_{0.8}Sr_{0.2}FeO_{3-\delta}$ (LSF821) and $La_{0.8}Sr_{0.2}Fe_{0.7}Ga_{0.3}O_{3-\delta}$ (LSFG8273) in the temperature range from room temperature to 1373 K in air and pure nitrogen atmosphere by using ultrasonic pulse echo technique [1.82]. The measurements were performed both upon heating and cooling. Their results are also plotted in Fig. 1.17. The Young's modulus of LSF821 decreases by 38 % of the initial value with increasing temperature up to 613 K. Then it increases by 19 % from the minimum value up to 1073 K and again decreases by 3 % in air and 7 % in nitrogen at higher temperatures. The Young's modulus of LSCF8273 decreases by 33 % of the initial value with increasing temperature up to 543 K, then increases by 15% up to 1133 K in air and 1073 K in nitrogen. Then the Young's modulus decreases by 3.5 % in air and 5 % in nitrogen. On cooling, the similar temperature dependence is observed but the onsets of the decrease and the increase in the Young's modulus of both LSF821 and LSFG8273 are observed at different temperatures. They attribute the cause of the decrease observed at lower temperature to the distortion of oxygen octahedra. Also, they reported that the temperature at which the increase in the Young's modulus of both materials agreed with the phase transition temperature. Thus the increase in the Young's modulus may be associated with the phase transition. The slight decrease observed at higher temperatures is related with the thermal expansion and a weight loss of the material, according to their explanation. They associate the difference in the temperature dependence of the Young's modulus of LSFG 8273 upon heating and cooling, with the difference in the phase transition temperature, which is caused by the residual oxygen vacancies.

The drastic increase is also observed in the Young's modulus of $La_{1/3}Sr_{2/3}FeO_{3-\delta}$, $Pr_{1/3}Sr_{2/3}FeO_{3-\delta}$, and $(La_{1-x}Pr_x)_{1/3}Sr_{2/3}FeO_{3-\delta}$ [1.83]. Z. C. Xu *et al.* interpret this increase as indicating the phase transition from rhombohedral to cubic [1.83].

A small elastic anomaly is also observed in the Young's modulus of Sr-substituted $LaFeO_3$ based oxides and Ca-substituted $LaFeO_3$ based oxides below the room temperature. This anomaly is explained to be due to a charge ordering transition [1.84-1.87].

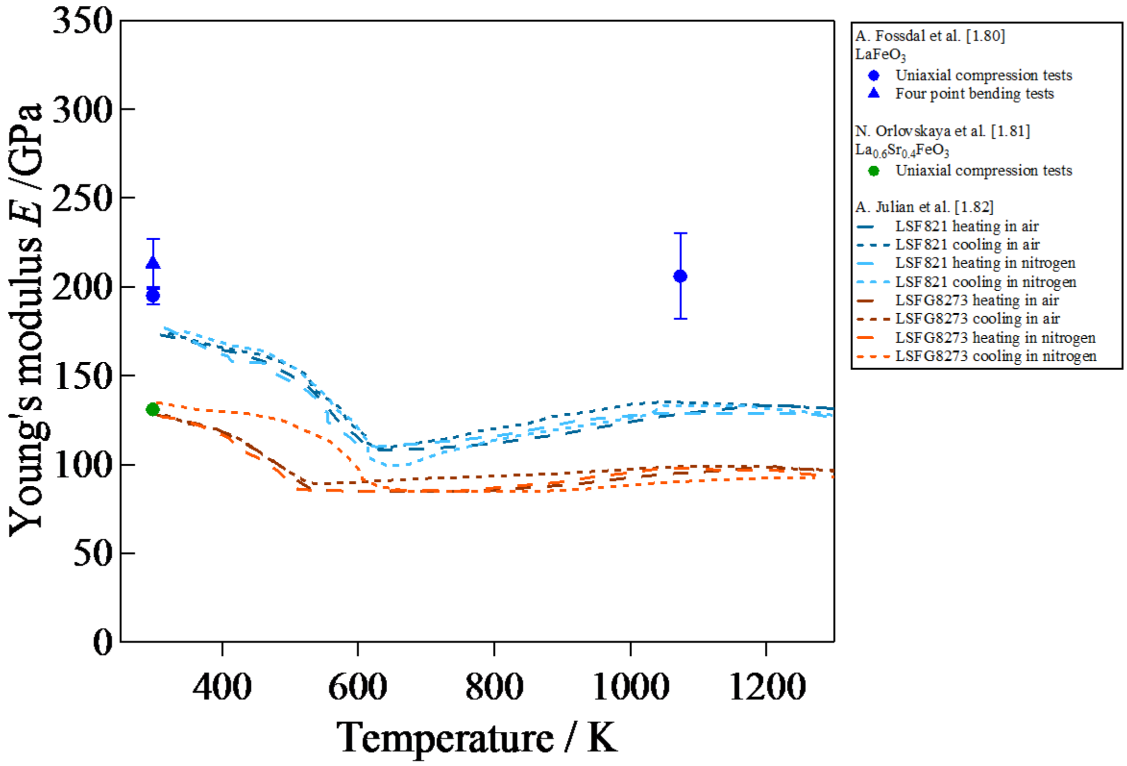

Fig. 1.15 Young's modulus of $LaFeO_3$ based oxides which are taken from literatures [1.80-1.82].

1.5.4 (La, Sr)(Co, Fe)O_3 based oxides

At room temperature, several researchers measured the Young’s modulus of (La, Sr)(Co, Fe)O_3 based oxides (LSCF). Figure 1.18 shows the Young’s modulus of LSCF which are taken from literature [1.79, 1.88-1.90]. Y. S. Chou *et al.* systematically evaluated the Young’s modulus of $La_{1-x}Sr_xCo_{0.2}Fe_{0.8}O_{3-\delta}$ (x = 0.2; LSCF8228, 0.4; LSCF6428, 0.6; LSCF4628, and 0.8; LSCF2828) using ultrasonic pulse echo method [1.88]. The values of LSCF8228, 6428, 4628, and 2828 are 161, 152, 167, and 188 GPa. Thus the Young’s modulus seems to increase with increasing Sr content. The relative densities of those materials are 95.89, 95.36, 96.54, and 94.95 %. Z. Chen *et al.* also measured the Young’s modulus of LSCF6428 using IET. The Young’s modulus and the relative density of Z. Chen *et al.* are 147 ± 3 GPa and 94.78 ± 0.01 %, respectively [1.89]. Thus considering the difference in the relative density, the value of the Young’s modulus measured by Z. Chen *et al.* is comparable to the one by Y. S. Chou *et al.*.

H. L. Lein *et al.* reported the temperature dependence of the Young’s modulus of LSCF5555 as a function of temperature [1.79]. They measured the Young’s modulus by RUS in the temperature range from room temperature and 1473 K in air and nitrogen atmosphere. The Young’s modulus monotonically decreases with increasing temperature and the value is not significantly influenced by the measuring atmosphere. B. X. Huang *et al.* measured the Young’s modulus of $La_{0.58}Sr_{0.4}Co_{0.2}Fe_{0.8}O_3$ as a function of temperature in air and in vacuum by ring-on-ring tests [1.90]. Contrary to the results of H. L. Lein *et al.*, The Young’s modulus initially decreases by approximately 20% of the initial value with increasing temperature. Then it again increases under both conditions, which starts at ~873 K and ~973 K in vacuum and in air, respectively. Upon cooling, the Young’s modulus decreases significantly, but the value is higher than that upon heating. In air, the increase and decrease in the Young’s modulus occurs in a narrow temperature range. In vacuum, a large hysteresis is observed. They also evaluated the temperature dependence of the Young’s modulus of $La_{0.58}Sr_{0.4}Co_{0.2}Fe_{0.8}O_3$ in air by using IET, although the absolute value is not provided [1.91]. Again, the initial drastic decrease and the significant increase in the Young’s modulus at intermediate temperatures are observed. As well as the case of Sr-substituted $LaMnO_3$ reported by Y. Shirai, the significant increase in the Young’s modulus occurs at around the phase transition temperature from rhombohedral to cubic. This suggests that the increase is related with the phase transition. They interpret the difference in the temperature at which the increase starts in air and vacuum to be due to the difference in the oxygen vacancy concentration. They believe that the increase starts at lower temperature in vacuum since cubic symmetry is more stable at high temperature and higher oxygen vacancy concentration. X. S. Wu *et al.* measured the shear modulus of $La_{0.6}Sr_{0.4}Co_{1-x}Fe_xO_3$ ($0 \leq x \leq 0.8$) in the temperature range between 120 and 650 K by the forced-vibration method, changing measuring frequency [1.92]. They also observed the drastic decrease in the Young's modulus above the room temperature. Also the onset of the decrease is observed at different temperature depending on measuring frequency.

B. X. Huang *et al.* evaluated the influence of oxygen potential gradient of mechanical properties [1.93]. They annealed the disc-shaped samples of $La_{0.58}Sr_{0.4}Co_{0.2}Fe_{0.8}O_3$ at 1173 K for 50 h under an oxygen potential gradient. The top surface was exposed to air while the bottom surface was exposed to vacuum ($P(O_2)$ = 2mbar). Then the samples were slowly cooled to room temperature (0.5 K/min) and indentation tests were performed on the cross section of the sample at room temperature. However, the Young's modulus is almost constant along the cross section and no significant dependence on oxygen potential gradient is observed.

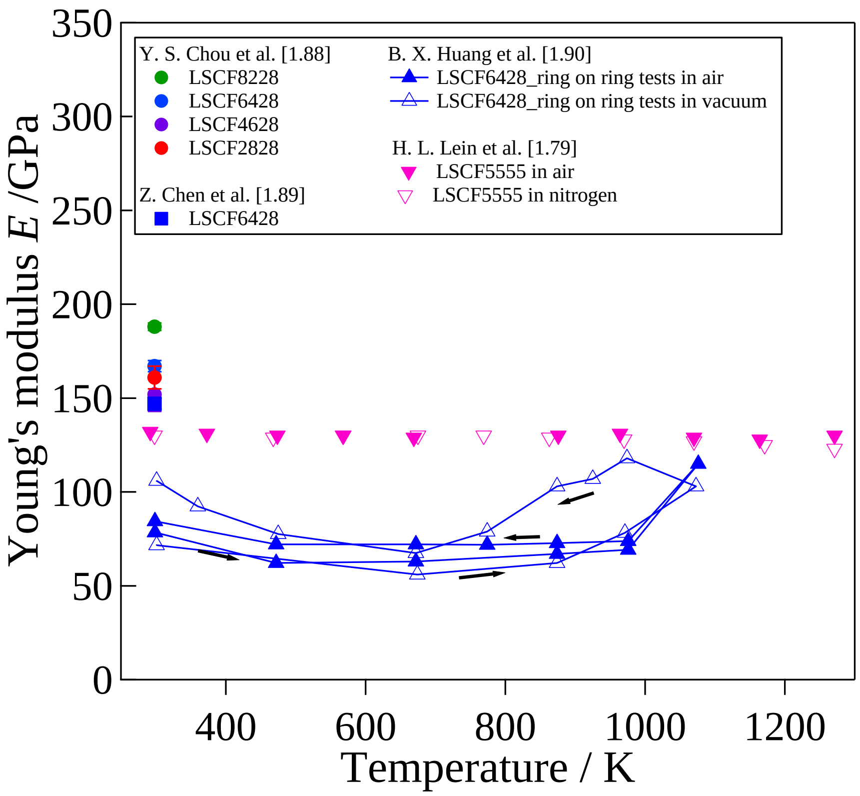

Fig. 1.16 Young's modulus of (La, Sr)(Co, Fe)O_3 based oxides which are taken from literatures [1.79, 1.88-1.90].

1.5.5 $LaGaO_3$ based oxides

A. A. Yaremchenko *et al.* measured the Young's modulus of $LaGa_{0.65}Mg_{0.15}Ni_{0.20}O_{3-\delta}$ at room temperature by three point bending tests, four point bending tests, tension tests, and compression tests [1.94]. Their results are shown in Fig. 1.19. The value is significantly different depending on measuring method but no explanation is provided for the cause of this difference.

T. Okamura *et al.* measured the Young's modulus of $La_{0.9}Sr_{0.1}Ga_{0.8}Mg_{0.2}O_{3-\delta}$ as a function of temperature by resonance method [1.95]. The value at room temperature is 176 GPa. The Young's modulus rapidly decreases with increasing temperature over the temperature range from 473 and 873 K. Then it increases with increasing temperature in the temperature range from 873 to 1173 K and again decreases at further higher temperatures. They attribute the cause of the elastic anomaly to the successive structural change of rhombohedral structure.

A. A. Yaremchenko *et al.* also measured the $P(O_2)$ dependence of the Young's modulus of $LaGa_{0.65}Mg_{0.15}Ni_{0.20}O_{3-\delta}$ at 773 and 1173 K, which is shown in Fig. 1.120[1.94]. At both temperatures, the Young's modulus of $LaGa_{0.65}Mg_{0.15}Ni_{0.20}O_{3-\delta}$ is almost independent of $P(O_2)$.

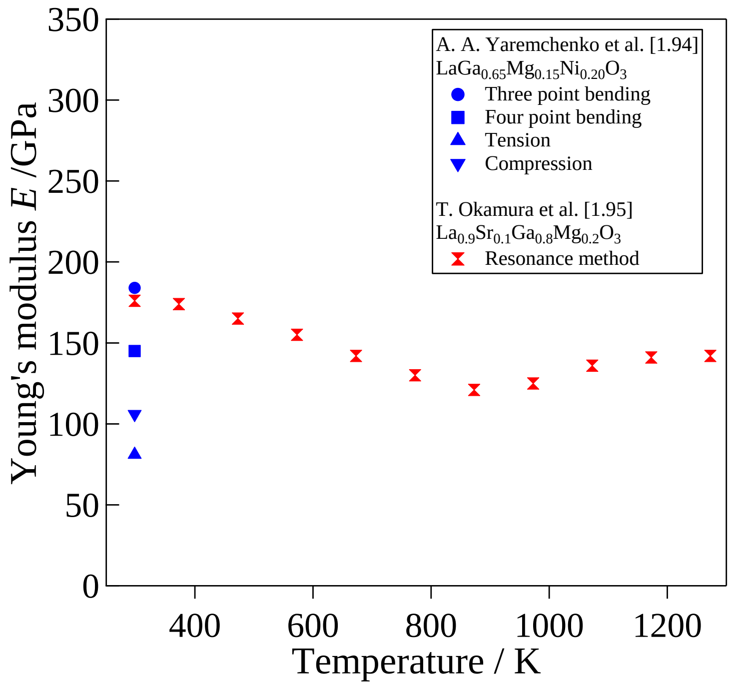

Fig. 1.17 Young's modulus of $LaGaO_3$ based oxides which are taken from literatures [1.94, 1.95].

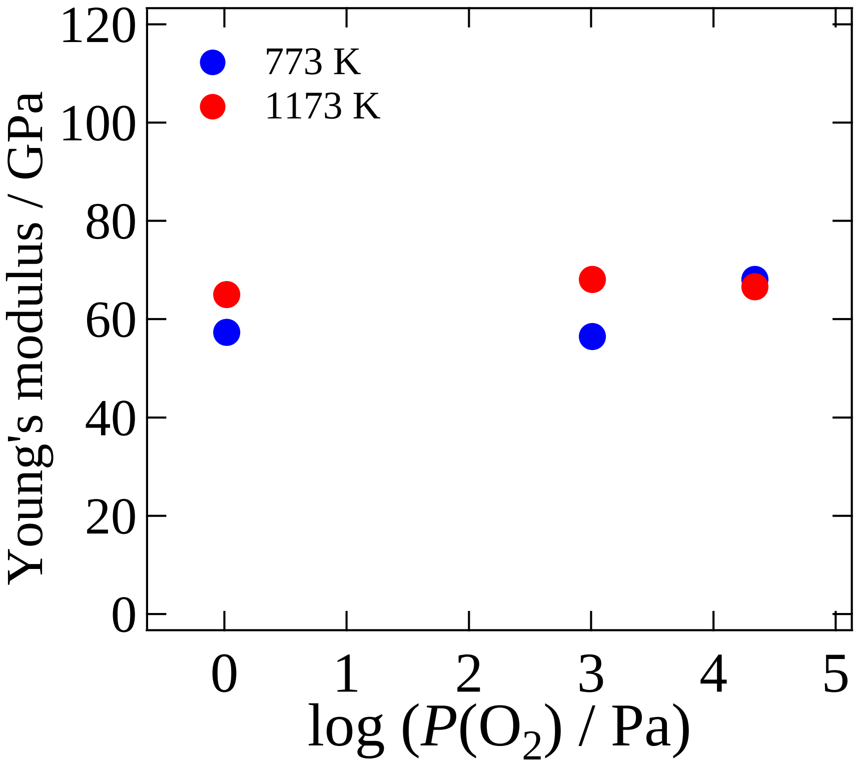

Fig. 1.18 $P(O_2)$ dependence of the Young’s modulus of $LaGa_{0.65}Mg_{0.15}Ni_{0.20}O_{3-\delta}$ at 773 and 1173 K [1.94].

1.5.6 *$LaCrO_3$ based oxides*

Y. S. Chou *et al.* reported the Young’s modulus of $La_{1-x}Sr_xCr_{0.2}Fe_{0.8}O_3$ (LSCrF, x = 0.2: LSCrF8228, x = 0.2: LSCrF6428, x = 0.6: LSCrF4628, x = 0.8: LSCrF2828) at room temperature [1.96]. They measured the Young’s modulus by IET. The results are shown in Fig. 1.21. Contrary to the results of $La_{1-x}Sr_xCo_{0.2}Fe_{0.8}O_{3-\delta}$, the Young’s modulus of LSCrF decreases with increasing Sr content. The relative densities of LSCrF8228, LSCrF6428, LSCrF4628, and LSCrF2828 are 92.9, 96.8, 97.2, and 96.0 %, respectively. Therefore, it is considered that the decrease in the Young’s modulus with increasing Sr content is not related with the relative density. They consider the cause of this decrease is due to the crystal structure. It is said that the Young’s modulus is inversely related to the high power of nearest-neighbor separation [1.97]. They investigated the cubic root of unit volume of LSCrF and found it increased from 3.866

to 3.893-3.896 Å with increasing Sr content. On the other hand, Tai *et al.* reported that the cubic root of unit volume of LSCF decreases with increasing Sr content [1.98]. Thus the Sr content dependence of the Young's modulus of both LSCrF and LSCF can be reasonably explained by considering the high power of nearest-neighbor separation.

S. W. Paulik *et al.* evaluated the $P(O_2)$ dependence of the Young's modulus of $La_{1-x}Ca_xCrO_3$ (x = 0.25: LCC25 and 0.30: LCC30) and $La_{1-x}Sr_xCrO_3$ (x = 0.16: LSC16, 0.20: LSC20, and 0.24: LSC24) which is shown in Fig. 1.22 [1.99]. The Young's modulus was measured by the sonic pulse technique at room temperature after the samples were heat-treated at 1273 K and under various oxygen partial pressures for 2 h. Whereas the Young's modulus of LCC25 and LCC30 is almost independent of $P(O_2)$, the Young's modulus of LSC16, LSC20, and LSC24 significantly increases with decreasing $P(O_2)$ under reducing atmospheres. However, they do not give any clear explanation for the increase in the Young's modulus of LSC16, LSC20, and LSC24. They consider it may arise from changes in the grain-boundary structure.

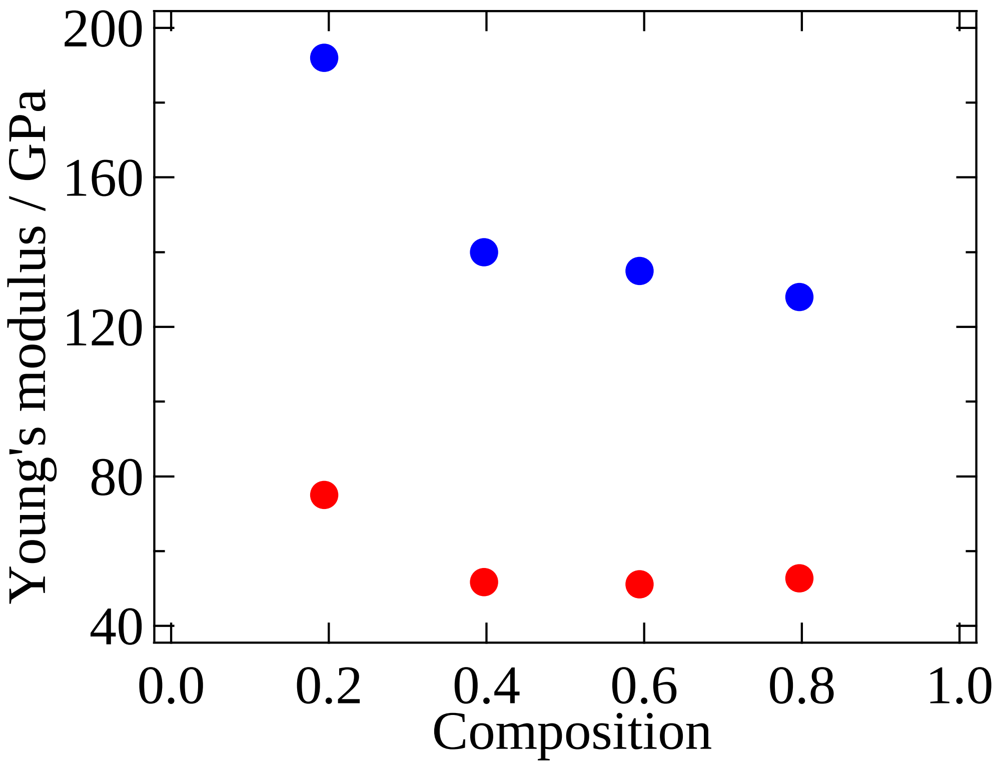

Fig. 1.19 Young's modulus of $La_{1-x}Sr_xCr_{0.2}Fe_{0.8}O_3$ (LSCrF, x = 0.2: LSCrF8228, x = 0.2: LSCrF6428, x = 0.6: LSCrF4628, x = 0.8: LSCrF2828) at room temperature measured by the impulse echo tests [1.96].

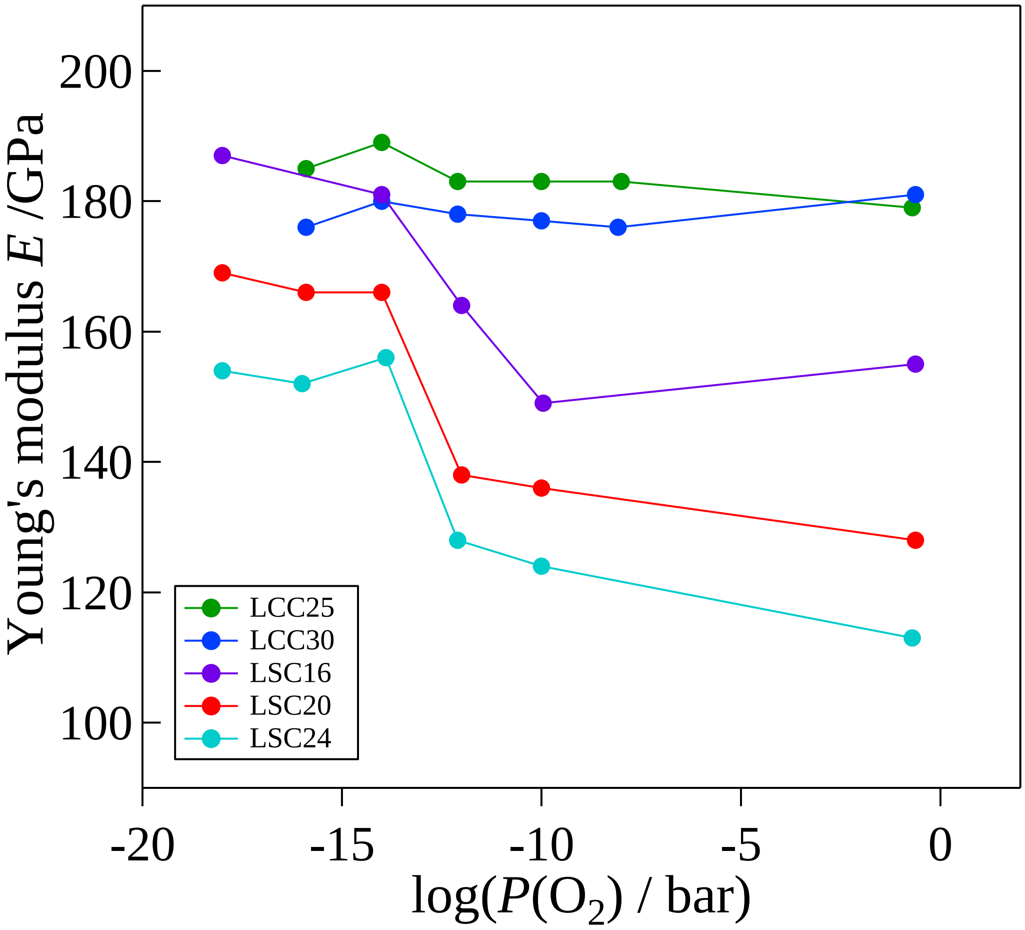

Fig. 1.20 $P(O_2)$ dependence of the Young's modulus of $La_{1-x}Ca_xCrO_3$ (x = 0.25: LCC25 and 0.30: LCC30) and $La_{1-x}Sr_xCrO_3$ (x = 0.16: LSC16, 0.20: LSC20, and 0.24: LSC24) [1.99]. The Young's modulus was measured by the sonic pulse technique at room temperature after the samples were heat-treated at 1273 K and under various oxygen partial pressures for 2 h.

1.5.7 La_2NiO_4 based oxides

B. X. Huang *et al.* evaluated the temperature dependence of the Young's modulus of La_2NiO_4 (LN214) from room temperature to 1173 K [1.100]. They prepared porous samples (relative density ~48 %) and dense samples (~94 %). The Young's modulus of the porous samples was measured by the four point bending tests while the one of the dense samples was measured by IET. The four point bending tests were performed in air and vacuum while the IET measurements were performed in air. Figure 1.23 shows their results. The values of the Young's modulus of the porous samples are significantly lower than that of the dense samples due to the larger porosity. The Young's modulus of the porous samples is essentially independent of temperature within the limits of uncertainty. The value of the Young's modulus measured at 1073 K and in vacuum appears to be slightly higher than the value in air. The Young's modulus of LN214 measured by IET decreases by 10 % with increasing temperature up to 373 K and then slightly decreases with increasing temperature. They attribute the cause of the 10 % decrease in the Young's modulus below 373 K to the phase transition from orthorhombic to tetragonal.

T. M. Brill *et al.* evaluated the temperature dependence of the elastic constants of single-crystal LN214 by using rf-pulse-echo method [1.101]. Figure 1.24 shows their results. They also reported the elastic anomaly in the elastic constant, especially c_{66}, at around 360 K, at which the phase transition from orthorhombic to tetragonal is considered to occur.

T. Nakamura *et al.* measured the Young's modulus of LN214 at 1073 K and under $P(O_2)$ of 1.0 and 1.0 x 10^{-4} bar by small punch tests as shown in Fig. 1.25 [1.102]. However, from their data, it is difficult to judge if the Young's modulus of LN214 depends on $P(O_2)$, since the data contain large uncertainty.

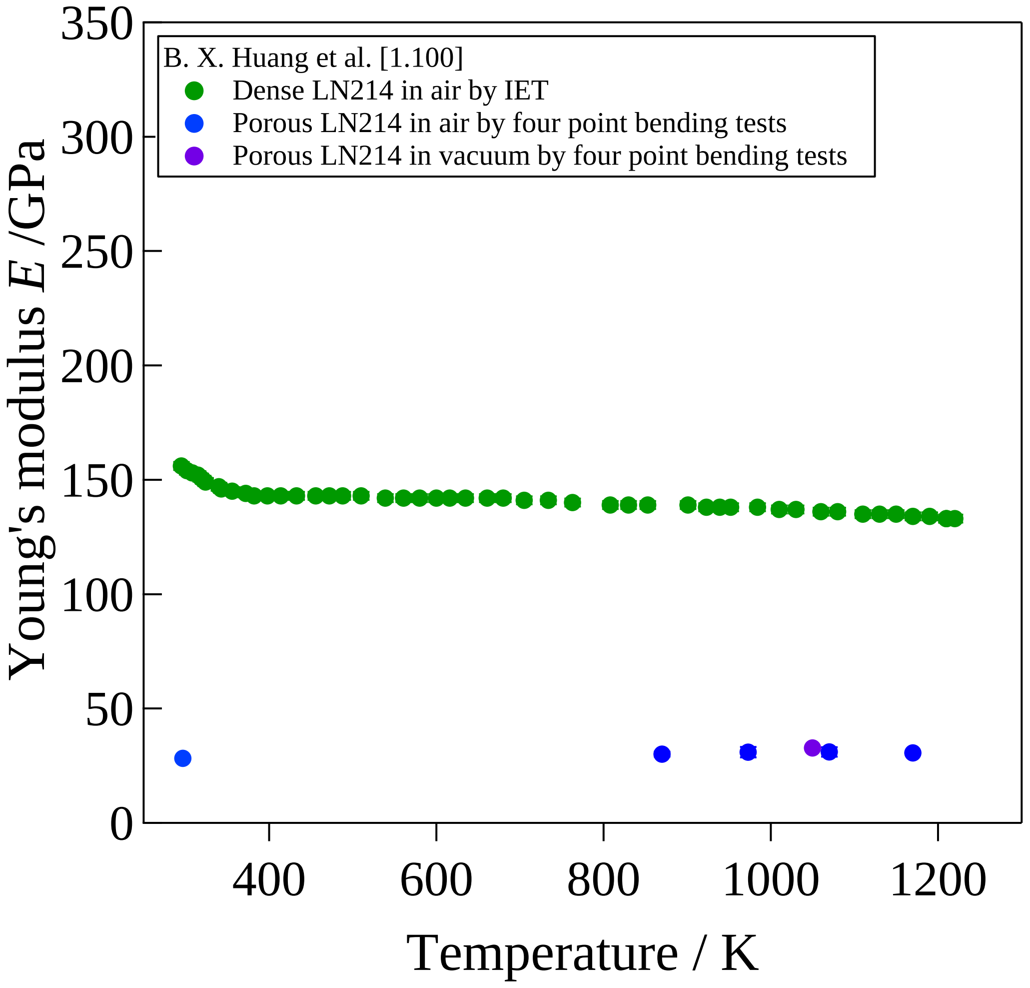

Fig. 1.21 Temperature dependence of the Young’s modulus of porous samples (relative density ~48 %) and dense samples (~94 %) of La_2NiO_4 (LN214) from room temperature to 1173 K [1.100]. Young’s modulus of the porous samples was measured by the four point bending tests while the one of the dense samples was measured by IET.

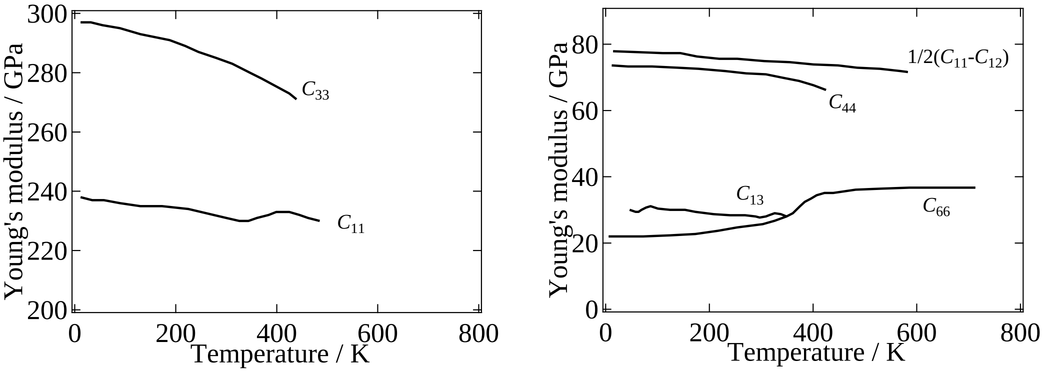

Fig. 1.22 Temperature dependence of the elastic constants of single-crystal La_2NiO_4 (LN214) measured by using rf-pulse-echo method [1.101].

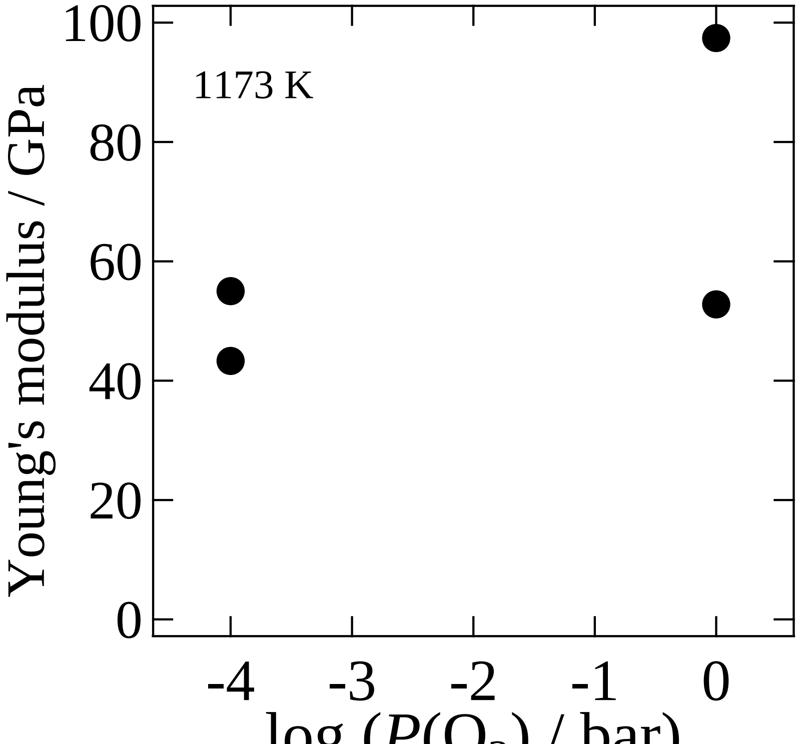

Fig. 1.23 Young's modulus of LN214 at 1073 K and under $P(O_2)$ of 1.0 and 1.0 x 10^{-4} bar measured by small punch tests [1.102].

1.5.8 Nonelastic behavior of rhombohedral perovskite oxides at low temperatures

At low temperatures, some perovskite oxides with rhombohedral symmetry are reported to exhibit a nonelastic behavior. This behavior is observed with $LaCoO_3$ based oxides [1.75, 1.103-1.108], $LaFeO_3$ based oxides [1.81], (La, Sr)(Co, Fe)O_3 based oxides [1.109-1.111], (Ba, Sr)(Co, Fe)O_3 based oxides [1.112], $LaMnO_3$ based oxides [1.113], $LaCrO_3$ based oxides [1.114].

Whereas the stress-strain relationship of conventional ceramics such as alumina is linear until the fracture occurs, N. Orlovskaya *et al.* reported that $La_{0.6}Sr_{0.4}FeO_3$ with rhombohedral symmetry shows a nonlinear stress-strain relationship as shown in Fig. 1.26 [1.81]. Thus the apparent elastic modulus of $La_{0.6}Sr_{0.4}FeO_3$ with rhombohedral symmetry, which is determined from the slope of the stress-strain relationship, depends on the applied stress.

M. Lugovy *et al.* reported the creep-like time dependent strain of $LaCoO_3$ under constant stress at room temperature (Fig. 1.27) [1.104]. This creep-like strain has a characteristic different from the one of the high temperature creep. The strain of the high temperature creep, which is a function of stress, time, temperature, grain size, shape, microstructure, defect mobility, and other material parameters, continues to increase and eventually leads to a fracture of a sample if a constant stress is applied. On the other hand, the strain of the low temperature creep-like behavior reported by Lugovy *et al.* has an equilibrium value at a given stress.

Those nonelastic behaviors of perovskite oxides with rhombohedral symmetry are considered to be caused by ferroelastic domain switching [1.110]. This effect should be taken into account when the Young’s modulus of rhombohedral perovskite oxides is evaluated.

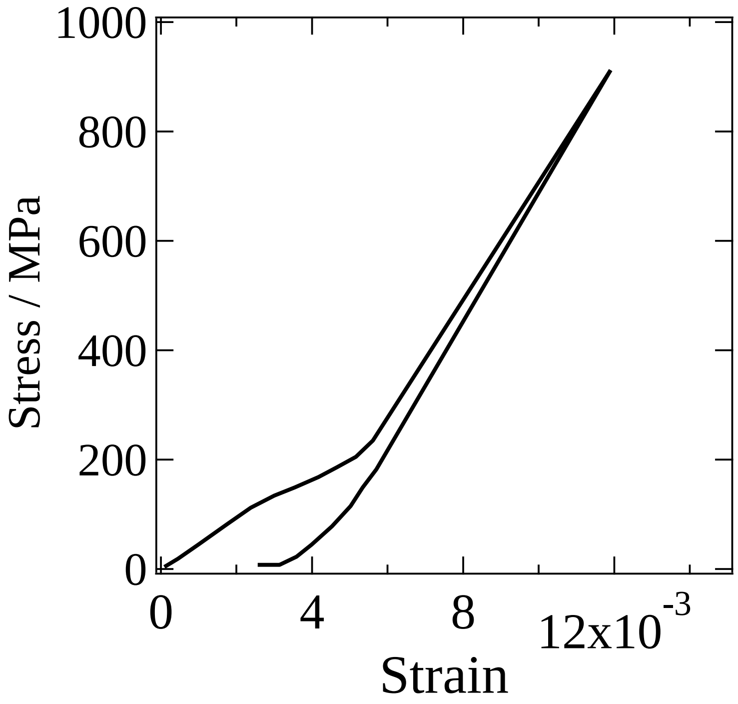

Fig. 1.24 Stress-strain relationship of $La_{0.6}Sr_{0.4}FeO_3$ with rhombohedral symmetry measured by uniaxial compression tests at room temperature [1.81].

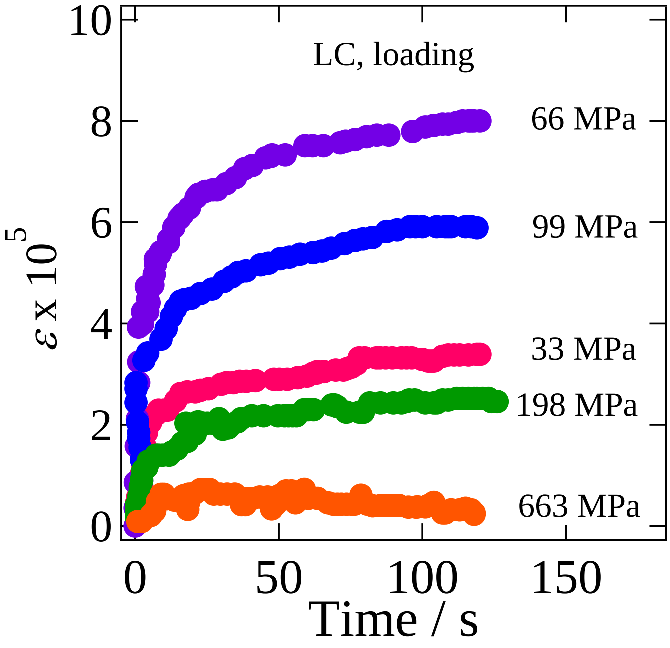

Fig. 1.25 Creep-like time dependent strain of $LaCoO_3$ under constant stress at room temperature . The stress is uniaxially applied to the sample [1.104].

1.6 Scope of this study

The perovskite and related oxides are one of the important components of high temperature energy conversion devices, such as SOFCs. For further commercialization of SOFCs, it is necessary to suppress the mechanical degradation and improve their reliability and durability. In order to do this, the mechanical properties of perovskite and related oxides for SOFC components should be correctly understood. However, as briefly reviewed in the above section, the mechanical properties of the perovskite and related oxides at high temperatures under controlled atmospheres are still poorly available compared to their room temperature mechanical properties. This is despite that the temperature dependence of the Young's modulus of perovskite and related oxides can be significantly influenced by the phase transition which occurs at intermediate or high temperatures. Moreover, the oxygen defect concentration of perovskite and related oxides can change depending on temperature and $P(O_2)$. However, there are few studies which examine the influence of the defect concentration on the mechanical properties. Furthermore, several perovskite oxides with rhombohedral symmetry are reported to show the nonelastic behavior.

Therefore, in this thesis, the mechanical properties of perovskite and related oxides for energy conversion devices are evaluated at high temperatures and under controlled atmospheres.

In chapter 2, mechanical properties of perovskite and related oxides, $La_{0.6}Sr_{0.4}Co_{1-y}Fe_{y}O_{3-\delta}$ (LSCF, LSC for $y = 0$, LSCF6482 for $y = 0.2$, LSCF6428 for $y = 0.8$, LSF for $y = 1$) and La_2NiO_4 (LN214) were investigated at high temperatures under controlled atmospheres by using resonance method and small-punch tests.

In chapter 3, the $P(O_2)$ dependence of mechanical properties of LSCF6428 and LN214 were directly evaluated at high temperatures in order to understand the influence of the defect concentration on the mechanical properties.

In chapter 4, the stress-strain relationship of LSCF was investigated by uniaxial compression tests. And the amplitude and frequency dependence of the elastic modulus and the internal friction of perovskite and related oxides were evaluated by the resonance method and dynamic mechanical analysis (DMA) in order to understand the influence of ferroelasticity on the mechanical properties. In addition, DMA was also performed with LSCF6428 with various oxygen vacancy concentrations, in order to understand the influence of the interaction between the ferroelastic domain walls and the oxygen vacancies on the mechanical properties.

In chapter 5, two cases of simulations were performed in order to separately examine the influence of the domain switching and the change in the defect concentration on the stress distribution in the energy conversion devices.

1. 7 References

[1.1] A. V. da Rosa, *Fundamentals of Renewable Energy processes second Edition*, pp. 5-26, pp. 287-329, Academic Press, San Diego, 2009.
[1.2] International Energy Agency, *2014 Key World Enrgy Statistics*, The Electronics Division,
http://www.iea.org/publications/freepublications/publication/KeyWorld2014.pdf.
[1.3] Agency for Natural Resources and Energy, Ministry of Economy, Trade and Industry, Japanese Government, *2014 White Paper for Energy Usage*, The Electronics Division,
http://www.enecho.meti.go.jp/about/whitepaper/2014pdf/whitepaper2014pdf_1_1.pdf.
[1.4] The IPCC fifth assessment report has concluded that it is extremely likely that human influence has been the dominant cause of the observed warming
Intergovernmental Panel on Climate Change, *IPCC fifth Assessment Report*, The Electronics Division,
http://www.ipcc.ch/pdf/assessment-report/ar5/wg1/WG1AR5_SPM_FINAL.pdf.
[1.5] N. Q. Minh, *J. Am. Ceram. Soc*. **76**, 563 (1993).
[1.6] M. Ni, M. K. H. Leung, and, D. Y. C. Leung, *Int. J. Hydrogen Energy*, **33**, 2337 (2008).
[1.7] H. Kawamoto, *Proc. Soc. Mater. Sci., Japan*, **51**, 363 (2003).
[1.8] M.A. Laguna-Bercero, *J. Power Sources*, **203**, 4 (2012).
[1.9] J. Sunarso, S. Baumann, J.M. Serra,W.A. Meulenberg, S. Liu, Y.S. Lin, J.C. Diniz da Costa, *J. Membr. Sci*., **320**, 13 (2008).
[1.10] W. Yang, H. Wang, X. Zhu, and L. Lin, *Top. Catal*., 35, 155 (2005).
[1.11] H. J. M. Bouwmeester, *Catal. Today*, **83**, 141 (2003).
[1.12] H. Iwahara, *Solid State Ionics*, **77**, 289 (1995).
[1.13] H. Iwahara, *Solid State Ionics*, **86-88**, 9 (1996).
[1.14] T. Norby, Y. Larring, *Solid State Ionics*, **136-137**, 139 (2000).
[1.15] M. D. Graef and M.E. McHenry, *Structure of Materials An Introduction to Crystallography, Diffraction, and Symmetry*, p. 671, Cambridge university Press, New

York, 2007.

[1.16] R.E. Schaak and T. E. Mallouk., *Chem. Mater.*, **14**, 1455 (2002).

[1.17] Z. Zhang and M. Greenblatt, *J. Solid State Chem.*,**117**, 236 (1995).

[1.18] M. A. Pena and J. L. G. Fierro, *Chem. Rev*., **101**, 1981 (2001).

[1.19] J. Mizusaki, Y. Mima, S. Yamauchi, and K. Fueki, *J. Solid State Chem.*, **80**, 102 (1989).

[1.20] T. Ishigaki, S. Yamauchi, J. Mizusaki, and K. Fueki, *J. Solid State Chem.*, **54**, 100 (1984).

[1.21] J.D. Jorgensen, B. Dabrowski, S. Pei, D. R. Richards, and D. G. Hinks, *Phys. Rev. B*, **40**, 2187 (1989).

[1.22] A. J. Jacobson, *Chem. Mater.*, **22**, 660 (2010).

[1.23] H. Obayashi, Y. Sakurai, and T. Gejo, *J. Solid State Chem.*, **17**, 299 (1976).

[1.24] K. Eguchi, *Development of Solid Oxide Fuel Cells*, pp. 1-24, 161-171, 215-222 CMC Press, Tokyo, 2005.

[1.25] B. C. H. Steele and A. Heinzel, *Nature*, **414**, 345 (2001).

[1.26] H. Yokokawa, N. Sakai, T. Horita and K. yamaji, *Fuel Cells*, **1**, 117 (2001).

[1.27] S. D. Vora, *ECS Trans.*, **57**(1), 11 (2013).

[1.28] Bloom Energy, Data available online at www.bloomenergy.com.

[1.29] Bloom Energy Corporation, *PRODUCT DATASHEET*, The Electronics Division, http://www.bloomenergy.co.jp/wp-content/themes/bloomenergy/files/be_datasheet_es-5700-j_japanese.pdf.

[1.30] Bloom Energy Corporation, *Press release (7/17/2013), "SoftBank & Bloom Energy Form Joint Venture to Provide Clean, Reliable, and Affordable Energy to Japan"*, Data available at http://www.bloomenergy.co.jp/information/news/press-release-07-17-2013-60.

[1.31]L. Blum, P. Batfalsky, L.G.J. de Haart, J. Malzbender, N. H. Menzler, R. Peters,W. J. Quadakkers, J. Remmel, F. Tietz, and D. Stolten, *ECS Trans.*, **57**(1), 23 (2013).

[1.32] L. Blum, U. Packbier, I. C. Vinke, and L.G. J. deHaart, *Fuel Cells*, **13**, 646 (2013).

[1.33] A. Mai, B. Iwanschitz, J. A. Schuler, R. Denzler, V. Nerlich, A. Schuler, *ECS Tran.*, **57**(1), 73 (2013).

[1.34] R. Steinberger-Wilckens, O. Bucheli, L.G.J. de Haart, A. Hagen, J. Kiviaho J. Larsen, S. Pyke, B. Rietveld, J. Sfeir, F. Tietz, and M. Zahid, *ECS Trans.*, **25**(2), 43 (2009).

[1. 35] K. Hosoi, M. Ito and M. Fukae, *ECS Trans.*, **35**, 11 (2011).

[1.36] T. Horita, K. Yamaji, H. Kishimoto and H. Yokokawa, *Bull. Ceram. Soc. Jpn.*, **44**, 267 (2009).

[1.37] New Energy Foundation, *Accomplishment report of the demonstrative research project of solid oxide fuel cells*, 2011, Data available at www.nef.or.jp.

[1.38] Fuel cells and hydrogen project group, NEDO(2008), *An outline of "Development of System and Elemental Technology on Solid Oxide Fuel Cell"* , Data available online at www.nedo.go.jp.

[1.39] JX Holdings, Inc., *Press release (9/15/2011)*, Data available at http://www.noe.jx-group.co.jp/newsrelease/2011/20110915_01_0950261.html.

[1.40] Osaka Gas Co., Ltd., *Press release (3/13/2012)*, Data available at http://www.osakagas.co.jp/company/press/pr_2012/1196121_5712.html.

[1.41] JX Holdings, Inc., *Press release (10/10/2014)*, Data available at http://www.noe.jx-group.co.jp/newsrelease/2014/20141010_01_1030113.html.

[1.42] ENEFARM PARTNERS, *Press release (9/29/2014)*, Data available at http://www.gas.or.jp/user/comfortable-life/enefarm-partners/common/data/20140929_web.pdf.

[1.43] Osaka Gas Co., Ltd., *Press release (3/10/2014)*, Data available at http://www.osakagas.co.jp/company/press/pr_2014/1209206_10899.html.

[1.44] H. Yokokawa, *ECS. Trans.*, **57**(1), 299 (2013).

[1.45] K. Horiuchi, *ECS Trans.*, **57**(1), 3 (2013).

[1.46] T. Shimonosono, H. Kishimoto, K. Yamaji, M. E. Brito, T. Horita and H. Yokokawa, *Solid State Ionics*, **225**, 61 (2012).

[1.47] T. Shimonosono, H. Kishimoto, K. Yamaji, M. E. Brito, T. Horita and H. Yokokawa, *Solid State Ionics*, **255**, 69 (2012).

[1.48] H. Kishimoto, K. Yashiro, T. Shimonosono, M. E. Brito, K. Yamaji, T. Horita, H.Yokokawa, and J. Mizusaki, *Electrochem. Acta*, **82**, 263 (2012).

[1.49] H. Yokokawa, H. Kishimoto, K. Yamaji, T. Horita, T. Watanabe, T. Yamamoto, K. Eguchi, T. Matsui, K. Sasaki, Y. Shiratori, T. Kawada, K. Sato, T. Hashida, A. Unemoto, T. Kabata, and K. Tomida, *ECS Trans.*, **35**(1), 2191 (2011).

[1.50] H. Yokokawa, T. Horita, K. Yamaji, H. Kishimoto, T. Yamamoto, M. Yoshikawa, Y. Mugirura, K. Tomida, *Fuel Cells*, **13**, 526 (2013).

[1.51] J.G. Swallow, W. H. Woodford, Y. Chen, Q. Lu, J. J. Kim, D. Chen, Y.-M. Chiang, W. C. Carter, B. Yildiz, H. L. Tuller, and K. J. Van Vliet, *J. Electroceram.*, **32**, 3 (2014).

[1.52] S. Hashimoto, Y. Fukuda, M. Kuhn, K. Sato, K. yashiro and J. Mizusaki, *Solid State Ionics*, **186**, 37 (2011).

[1.53] S. Wang, M. Katsuki, T. Hashimoto and M. Dokiya, *J. Electrochem. Soc.*, **150**, A952 (2003).

[1.54] T. R. Armstrong, J. W. Stevenson, L. R. Pederson and P. E. Raney, *J. Electrochem. Soc*., **143**, 2919 (1996).

[1.55] S. R. Bishop, *Acta Mech. Sinica* **29**, 312 (2013).

[1.56] S. Nakayama, S. Hashimoto, K. Sato, K. Yashiro, K. Amezawa, and J. Mizusaki, *ECS Trans.*, **25**(2), 1701 (2009).

[1.57] T. Ishihara, H. Furutani, M. Honda, T. Yamada,T. Shibayama, T. Akbay, N. Sakai, H. Yokokawa, and Y. Takita, *Chem. Mater.*, **11**, 2081 (1999).

[1.58] T. Kawada, S. Watanabe, S. Hashimoto, T. Sakamoto, A. Unemoto, M. Kurumatani, K. Sato, F. Iguchi, K. Yashiro, K. Amezawa, K. Terada, M. Kubo, H. Yugami, T. Hashida, and J. Mizusaki, *ECS Trans.*, **25**(2), 467 (2009).

[1.59] T. Kawada, T. Horita, N. Sakai, H. Yokokawa, M. Dokiya and J. Mizusaki, *Solid State Ionics*, **131**(2000)199.

[1.60] S. B. Adler, *Chem. Rev.*, **104**, 4791 (2004).

[1.61] F. Tariq, M. Kishimoto, S. J. Cooper, P. Shearing, and N. Brandon, *ECS Trans.*, **57**(1), 2553 (2013).

[1.62] T. Kawada, T. Horita, N. Sakai, H. Yokokawa, M. Dokiya and J. Mizusaki, *Solid State Ionics*, **131**, 199 (2000).

[1.63] T. Horita, K. Yamaji, N. Sakai, X. P. Xiong, T. Kato, H. Yokokawa and T. Kawada, *J. Power Sources*, **106,** 224 (2002)..

[1.64] J. Winkler, P. V. Hendriksen, N. Bonanos and M. Mogensen, *J. Electrochem. Soc*., **145**, 1184 (1998).

[1.65] K. Amezawa, T. Ina, Y. Orikasa, A. Unemoto, H. Watanabe, F. Iguchi, Y. Terada, T. Fukutsuka, T. Kawada, H. Yugami and Y. Uchimoto, *ECS Trans.*, **25**(2009)345.

[1.66] Y. Shirai, *Mechanical Properties of Complex Oxides for Solid Oxide Fuel Cells*, Master thesis, Graduate School of Environmental Studies, Tohoku University (2012).

[1.67] S. Miyoshi, A. Kaimai, H. Matsumoto, K. Yashiro, Y. Nigara, T. Kawada, and J. Mizusaki, *Solid State Ionics*, **175**, 383 (2004).

[1.68] O. Chmaissem, B. Dabrowski, S. Kolesnik, J. Mais, J. D. Jorgensen, and S. Short, *Phys.Rev B.*, **67**, 094431 (2003).

[1.69] T. Grande, J. R. Tolchard, and S. M. Selbach, *Chem. Mater*., **24**, 338 (2012).

[1.70] H. Cerva, *J. Solid State Chem.*, **120**, 175 (1995).

[1.71] S. Giraud and J. Canel, *J. Eur. Ceram. Soc.*, **28**, 77 (2008).

[1.72] K. Sakthipandi, V. Rajendran, T. Jayakumar, *Mater. Res. Bull.*, **48**, 1651 (2013).

[1.73] F. Cordero, C. Castellano, R. Cantelli, and M. Ferretti, *Phys. Rev. B*, **65**, 012403

(2001).

[1.74] Y.Q. Ma, W.H. Song, J. Yang, R.L. Zhang, B.C. Zhao, Z.G. Sheng, W.J. Lu, J.J. Du, Y.P. Sun, *Solid State Commun.*, **133**, 163 (2005).

[1.75] K. Kleveland, N. Orlovskaya, T. Grande, A. M. Mardal Moe, M.-A. Einarsrud, K. Breder, and G. Gogotsi, *J. Am. Ceram. Soc.*, **84**, 2029 (2001).

[1.76] S. Pathak, J. Kuebler, A. Payzant, and N. Orlovskaya, *J. Power Sources*, **195**, 3612 (2010).

[1.77] N. Orlovskaya, K. Kleveland, T. Grande, and M.-A. Einarsrud, *J. Eur. Ceram. Soc.*, **20**, 51 (2000).

[1.78] Z. Zhang, J. Koppensteiner, W. Schranz, D. Prabhakaran, and M. A Carpenter, *J. Phys.: Condens. Matter*, **23**, 145401 (2011).

[1.79] H. L. Lein, O. S. Andersen, P. E. Vullum, E. Lara-Curzio, R. Holmestad, M.-A. Einarsrud, and T. Grande, *J. Solid State Electrochem.*, **10**, 635 (2009).

[1.80] A. Fossdal, M.-A. Einarsrud, and T. Grande, *J. Eur. Ceram. Soc.*, **25**, 927, (2005).

[1.81] N. Orlovskaya, H. Anderson, M. Brodnikovskyy, M. Lugovy, and M. J. Reece, *J. Appl. Phys.*, **100**, 026102 (2006).

[1.82] A. Julian, E. Juste, P.M. Geffroy, N. Tessier-Doyen, P. Del Gallo, N. Richet, T. Chartier, *J. Euro Ceram. Soc.*, **29**, 2603 (2009).

[1.83] Z. C. Xu, C. C. Chen, X. N. Ying, *Applied Physics Letters*, **105**, 061905 (2014).

[1.84] X.S. Wu, Y.B. Zuo, J.H. Li, C.S. Chen, W. Liu, *J. Alloys Compd.*, **462**, 432 (2008).

[1.85] Z. C. Xu, M. F. Liu, C. C. Chen, and X. N. Ying, *J. Applied Physics*, **115**, 123516 (2014).

[1.86] X. N. Ying, *Applied Physics Letters*, **101**, 211906 (2012).

[1.87] X. N. Ying and L. Zhang, *Solid State Commun.*, **152**, 1252 (2012).

[1.88] Y. S. Chou, J. W. Stevenson, T. R. Armstrong, and L. R. Pederson, *J. Am. Ceram. Soc.*, **83**, 1457 (2000).

[1.89] Z. Chen, X. Wang, V. Bhakhri, F. Giuliani, and A. Atkinson, *Acta Mater.*, **61**, 5720 (2013).

[1.90] B.X. Huang, J. Malzbender, R.W. Steinbrech, and L. Singheiser, *Solid State Ionics*, **180**, 241 (2009).

[1.91] B.X. Huang, J. Malzbender, and R.W. Steinbrech, *J. Mater. Res.*, **26**, 1388 (2011).

[1.92] X. S. Wu, J. F. Cao, H. Kong, Z. J. Chen, and W. Liu, *J. Alloys Compd.*, **509**, 5029 (2011).

[1.93] B. X. Huang and J. Malzbender, *J. Eur. Ceram. Soc.*, **34**, 1777 (2014).

[1.94] A. A. Yaremchenko, V. V. Kharton, E. N. Naumovich, D. I. Shestakov, V. F. Chukharev, A. V. Kovalevsky, A. L. Shaula, M. V. Patrakeev, J. R. Frade, F. M. B. Marques, *Solid State Ionics*, **177**, 549, (2006).

[1.95] T. Okamura, S. Shimizu, M. Mogi, M. Tanimura, K. Furuya, F. Munakat, *J. Power Sources*, **130**, 38 (2004).

[1.96] Y. S. Chou, K. Kerstetter, L.R. Pederson, and R.E. Williford, *J. Mater. Res.*, **16**, 3545 (2001).

[1.97] M.L. Cohen, *Phys. Rev. B,* **32**, 7988 (1985).

[1.98] L-W. Tai, M.M. Nasrallah, H.U. Anderson, D.M. Sparlin, and S.R. Sehlin, *Solid State Ionics,* **76**, 272 (1995).

[1.99] S. W. Paulik, S. Baskaran, and T. R. Armstrong, *J. Mater. Scie.*, **33**, 2397 (1998).

[1.100] B. X. Huang, J. Malzbender, and R. W. Steinbrech, *J. Mater. Sci.*, **46**, 4937 (2011).

[1.101] T. M. Brill, G. Hampel, F. Mertens, R. Schurmann, W. Assmus, and B. Luthi, *Phys. Rev. B*, **43**, 10548 (1991).

[1.102] T. Nakamura, Y. Takeyama, S. Watanabe, K. Yashiro, K. Sato, T. Hashida, and J. Mizusaki, *ECS Trans.*, **25**(2), 2573 (2009).

[1.103] N. Orlovskaya, Y. Gogotsi, M. Reece, B. Cheng, and I. Gibson, *Acta Mater.*, **50**, 715 (2002).

[1.104] M. Lugovy, V. Slyunyayev, N. Orlovskaya, D. Verbylo and M. J. Reece, *Phys. Rev. B*, **78**, 024107 (2008).

[1.105] S. Faaland, T. Grande, M.-A. Einarsrud, P. E. Vullum, and R. Holmestad, *J. Am. Ceram. Soc.*, **88**, 726 (2005).

[1.106] W. Araki, T. Abe, and Y. Arai, *J. Appl. Phys.*, **116**, 043513 (2014).

[1.107] A. Aman, Y. Chen, M. Lugovy, N. Orlovskaya, M. J. Reece, D. Ma, A. D. Stoica,and K. An,*J. Appl. Phys.*, **116**, 013503 (2014).

[1.108] M. Lugovy, A. Aman, Y. Chen, N. Orlovskaya, J. Kuebler, T. Graule, M. J. Reece, D.Ma, A. D. Stoica, and K. An, *J. Appl. Phys.*, **116**, 013504 (2014).

LaFeO3

[1.109] W. Araki and J. Malzbender, *J. Eur. Ceram. Soc.*, **33**, 805 (2013).

[1.110] P. E. Vullum, R. Holmestad, H. L. Lein, J. Mastin, M.-A. Einarsrud, T. Grande, *Adv. Mater.*, **19**, 4399 (2007).

[1.111] B. X. Huang, J. Malzbender, R. W. Steinbrech, E. Wessel, H. J. Penkalla, and L. Singheiser, *J. Membr. Sci.*, **149**, 183 (2010).

[1.112] W. Araki and J. Malzbender, *Scripta Mater.*, **69**, 278 (2013).

[1.113] D. L. Meixner and R. A. Cutler, *Solid State Ionics*, **146**, 285 (2002).

[1.114] N. Orlovskaya, M. Lugovy, D. Verbylo, and M. J. Reece, *Scripta Mater.*, **60**, 783, (2009).

Chapter 2

The text presented in this Chapter is reproduced in part with permission from:

Y. Kimura, T. Kushi, S. Hashimoto, K. Amezawa and T. Kawada, , *J. Am. Ceram. Soc.*, **95**, 2608 (2012).

Evaluation of mechanical properties of perovskite and related oxides at high temperatures

2.1 Introduction

Perovskite and related oxides such as $LaCoO_3$-based oxides, $LaGaO_3$-based oxides, and La_2NiO_4-based oxides are expected to be a promising candidate for the components of high temperature energy conversion devices, *e.g.* solid oxide fuel cells (SOFCs) and permeation membranes [2.1-2.4]. One of the biggest problems for the full-scale commercialization of the high temperature energy conversion devices is to improve their durability and reliability [2.5]. Especially, it has been pointed out that the mechanical degradation of the components is one of the serious problems in securing the durability and the reliability [2.6, 2.7]. In order to suppress the mechanical degradation, it is necessary to correctly understand the mechanical properties of the components of the high temperature energy conversion devices. However, the data of their mechanical properties, especially at high temperatures, are still limited [2.8-2.10], although their chemical or electrochemical properties have been widely investigated [2.11-2.13]. It is expected that the mechanical properties of the components vary with temperature and oxygen partial pressure, $P(O_2)$ [2.8-2.10]. For instance, $La_{0.6}Sr_{0.4}Co_{1-y}Fe_yO_{3-\delta}$, which is one of the common cathode materials for SOFCs, changes its crystal structure and also shows a comparatively large oxygen nonstoichiometry depending on temperature and $P(O_2)$ [2.13-2.19]. When perovskite and related oxides are used as an SOFC component, they are exposed not only to high temperatures but also to a certain oxygen potential gradient. Therefore, it is important to understand influences of temperature and $P(O_2)$ on mechanical properties of perovskite and related oxides in suppressing the mechanical degradations.

In this study, mechanical properties of perovskite and related oxides,

$La_{0.6}Sr_{0.4}Co_{1-y}Fe_yO_{3-\delta}$ (LSCF, LSC for $y = 0$, LSCF6482 for $y = 0.2$, LSCF6428 for $y = 0.8$, LSF for $y = 1$) and La_2NiO_4 (LN214) were investigated at high temperatures under controlled atmospheres by using resonance method and small-punch tests.

2.2 Experimental

2.2.1. Resonance method

Powders of LSCF6428 were obtained from AGC SEIMI CHEMICAL Co., Ltd. and those of LSC, LSCF6482, LSF, LN214 were synthesized by the Pechini method. Nitrate solutions of La^{3+}, Sr^{2+}, Co^{3+}, Fe^{3+}, and Ni^{2+}, ethylene glycol and citric acid were mixed in an appropriate ratio, and heated to 673 K. The obtained polymeric precursor was calcined at 1173-1473 K. The obtained powders were hydrostatically pressed at 150 MPa, sintered at 1473-1673 K for 6 hours, and then slowly cooled with the rate of 106 K / h to avoid cracking. It was confirmed from X-ray diffraction that all of the as-sintered samples of LSC, LSCF6482, LSCF6428, and LSF had a single phase of rhombohedral perovskite (space group: $R\bar{3}c$) and LN214 had a single phase of tetragonal perovskite (space group: *I*4*/mmm*). The sintered samples were cut into a rectangular shape with 45 x 10 x 1.5 mm. The length, the width and the thickness of a sample were machined so that respective deviations in parallelism were less than 0.1, 0.1 and 0.02 mm. The surfaces were polished with a diamond paste of 3 µm.

The resonance measurements were performed at high temperatures and under controlled atmospheres by using EGII-HT (Nihon Technoplus Co., Ltd., Japan). The experimental apparatus used for the resonance method is shown in Fig. 2.1. EGII-HT performs cantilever measurements. One end of a sample is rigidly fixed while the other end is attached to a bar which is placed perpendicular to a sample. The bar has three electromagnetic actuators at the center and the both ends. The electromagnetic actuator at the center applies a flexural oscillation to a sample while the ones at the ends do a torsional oscillation. The resonance frequency of each oscillation is detected by eddy current sensors which are equipped at the opposite sides of the actuators across the bar. The Young’s modulus, *E*, and the shear modulus, *G*, are evaluated from the respective resonance frequencies and the sample dimension according to the following relations;

$$E = \frac{4\pi^2 L^4}{\alpha^2} \cdot \frac{\rho S}{I} \cdot f_{\mathbf{f}}^{\,2} \qquad [2.1]$$

$$G = \frac{16L^2 \cdot \rho K^2}{\beta} \cdot f_{\mathrm{t}}^{\ 2} \qquad [2.2]$$

where f_{f}, f_{t}, L, α, ρ, S, I, K, and β are the flexural resonance frequency, the torsional resonance frequency, the length of the sample, a constant given by the boundary conditions, the density of the sample, the cross-sectional area of the sample, the second moment of the area, the adjustment parameter and the inertia moment of the driven section, respectively. The Poisson's ratio, μ, was calculated from the Young's and the shear moduli as follows;

$$\mu = \frac{E}{2G} - 1 \qquad [2.3]$$

Prior to the measurements at high temperatures under controlled atmospheres, the Young's and shear moduli were measured by using JE and JG (Nihon Technoplus Co., Ltd., Japan) at room temperature. JE and JG perform free hold resonance measurements and generally have a higher accuracy than cantilever ones [2.20], although JE and JG are available only for measurements at room temperature. The measurement methodologies of JE and JG confirm to the Japanese Industrial Standards (JIS) R 1602 [2.21]. JE applies a flexural oscillation to a sample which is held on two thin wires at oscillation node points while JG does a torsional oscillation to a sample which is put on crossed wires. The flexural and torsional oscillations are electrostatically excited and the resonance frequencies of the respective oscillations are detected by an acoustic wave displacement sensor. In this work, absolute values of the elastic moduli obtained at room temperature with EGII-HT were calibrated by those with JE and JG.

Although JE and JG have a relatively high accuracy, measured values of the elastic moduli were slightly different from sample to sample. Such a slight discrepancy is considered to be mainly because of an incomplete parallelism of the sample. The maximum deviation among the elastic moduli of different samples having the same composition was about 3 %.

In this study, the elastic mouduli of LSCF were evaluated as a function of temperature under a constant $P(\mathrm{O_2})$ of 1 x 10^{-1} or 1 x 10^{-4} bar. $P(\mathrm{O_2})$ around the sample was controlled by flowing a mixture gas of $\mathrm{O_2}$ and Ar, and monitored by an yttria-stabilized zirconia oxygen sensor. Resonance measurements were repeated until the measured value of the elastic moduli reached a constant while keeping temperature and $P(\mathrm{O_2})$ constant, *i.e.*, until the sample equilibrated with the applied temperature and $P(\mathrm{O_2})$. The time required for the equilibration was typically 5-24 hours, and was longer at lower temperature and $P(\mathrm{O_2})$.

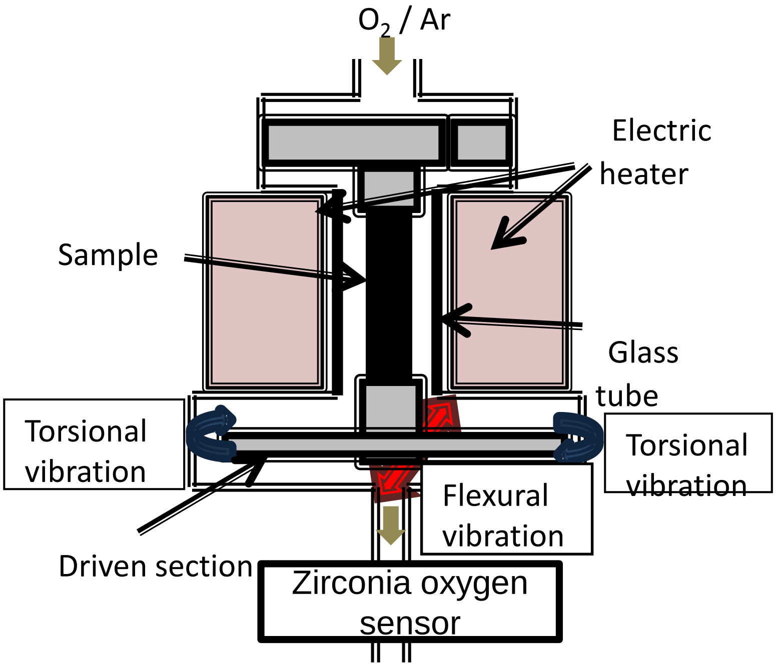

Fig. 2.1. The experimental apparatus used for the resonance method.

2.2.2 Small punch testing method

The powders were pressed into disks at 2 MPa and isostatically pressed at 150 MPa. The samples were then sintered in air at 1573 K for 6h and gradually cooled to room temperature with the cooling rate of 106 K/h. The sintered samples were cut into a square shape with the dimension of about 7 x 7 x 0.5 mm and polished with a diamond paste of 3 μm. The relative density of the sintered samples was over 96 %.

The Young's modulus of LSCF6428 were measured under a constant $P(O_2)$ of 1 x 10^{-1} bar by SP testing method. The experimental apparatus used for the SP tests is shown in Fig. 2.2 [2.22]. The samples were simply supported at the circumferential edge and subjected to a concentrated load at their center position. The SP tests were performed on a universal testing machine (INSTRON Type 5565, INSTRON, USA) at room temperature, 873K, 973 K, and 1073 K. The load was applied through a puncher until a final failure was observed. The cross head speed was 0.1 mm/min. The load-line deflection of the specimens was measured by monitoring the movement of an Al_2O_3 rod using a laser displacement sensor (LK-G15, Keyence, Japan). The resolution of the displacement sensor was within 1.0 μm. The Young's modulus, E_{sp}, was calculated using the following equations [2.23];

$$E_{sp} = f(t/a)\frac{3a^2(1-\mu)(3+\mu)}{4\pi t^2}\cdot\left(\frac{P}{d}\right) \qquad [2.4]$$

where *P*, *d*, *μ*, *a*, *t*, and *f*(t/a) are puncher load, displacement, Poisson's ratio, die radius, sample thickness, and adjustment parameter, respectively. The adjustment parameter is given by the following equation [2.23];

$$f\left(\frac{t}{a}\right) = 1.5136\times\left(\frac{t}{a}\right)^2 + 0.0162\times\left(\frac{t}{a}\right) + 0.9962 \qquad [2.5]$$

The Young's modulus was calculated from the linear slope of the load versus displacement records. The Poisson's ratio was taken from the data measured by the resonance method. Three samples were tested at each temperature.

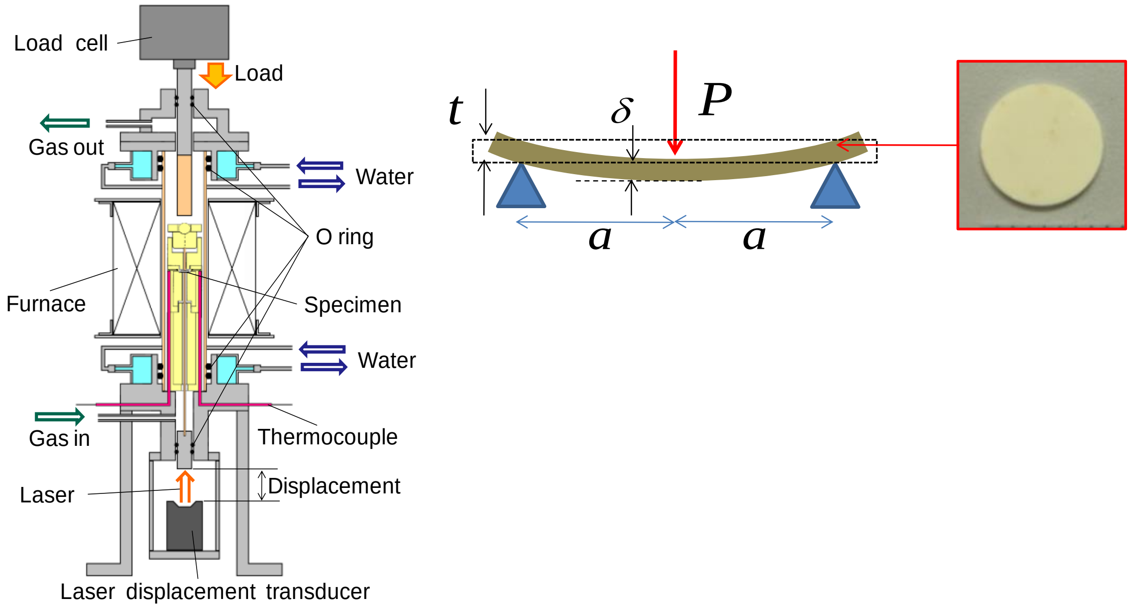

Fig. 2.2. The experimental apparatus used for the SP tests [2.22].

2.3. Results

2.3.1 Temperature Dependence of Mechanical Properties of LN214

Figure 2.3 shows the temperature dependence of the Young's and the shear moduli and the Poisson's ratio of LN214. The Young's modulus of LN214 monotonically decreased with increasing temperature. The shear modulus was almost independent of temperature. The Poisson's ratio monotonically decreased with increasing temperature. Fig. 2.4 shows the temperature dependence of the internal friction of LN214. The internal friction of LN214 was very small over the whole temperature range.

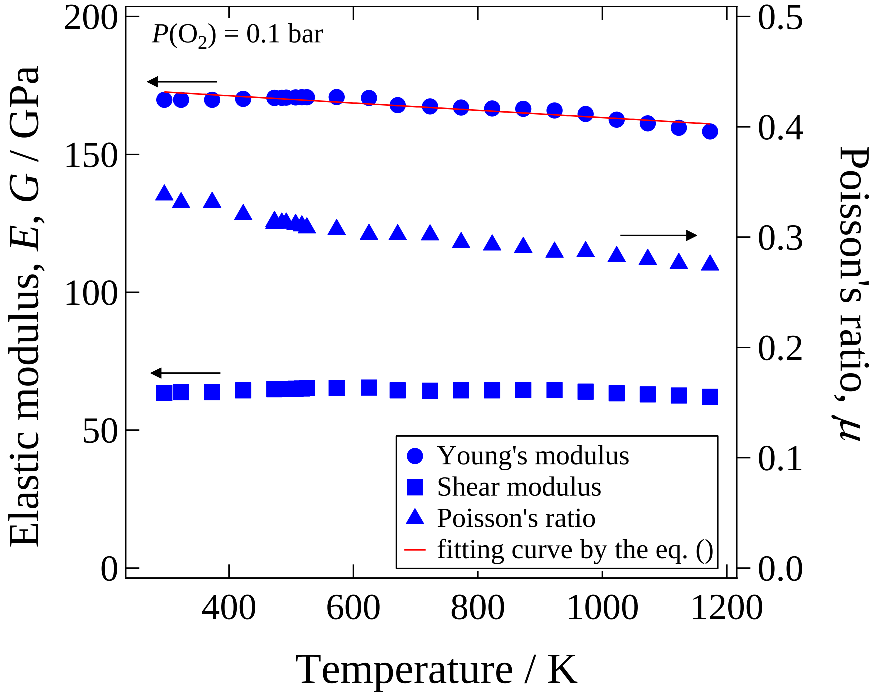

Fig. 2.3. Temperature dependence of the Young's and shear moduli of La_2NiO_4 (LN214) measured by the resonance method under $P(O_2)$ of 1.0 x 10^{-1} bar.

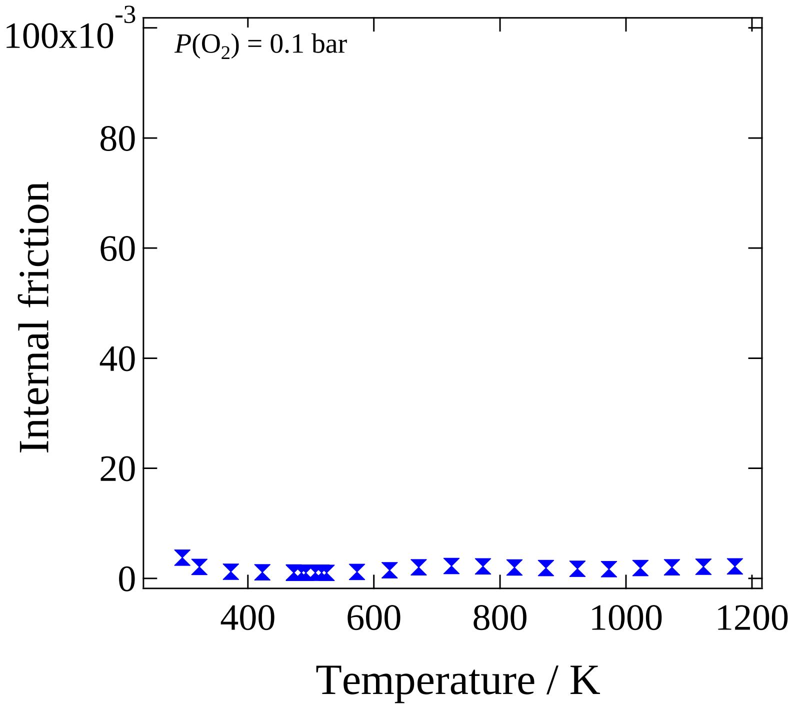

Fig. 2.4. Temperature dependence of the Young’s and shear moduli of La_2NiO_4 (LN214) measured by the resonance method under $P(O_2)$ of 1.0 x 10^{-1} bar.

2.3.2 Temperature dependence of E, G, and Q^{-1} of LSCF6428

Figure 2.5 shows the temperature dependence of the Young's and the shear moduli of LSCF6428 measured by the resonance method under $P(O_2)$ of 1.0 x 10^{-1} and 1.0 x 10^{-4} bar. Under $P(O_2)$ of 1.0 x 10^{-1} bar, the Young's and the shear moduli significantly decreased up to 823 K, gradually increased up to 973 K and then drastically increased at further higher temperatures. The Young's modulus of LSCF6428 at room temperature measured by the resonance method was 164 GPa. This value is slightly higher than the literatures reported by Y.-S. Chou *et al.* [2.24] (152 ± 3 GPa) and Z. Chen et al. [2.25] (147 ± 3 GPa). Y.-S. Chou *et al.* measured the Young's modulus by the ultrasonic/pulse-echo method while Z. Chen *et al.* did by the impulse excitation technique. This difference in the absolute value of the Young's modulus is possibly due to the difference in relative densities between the samples. The relative density of our sample was 98 %, while the relative densities of the samples of Y.-S. Chou *et al.* was 95.36 ± 0.22 % and the samples of Z. Chen *et al.* was 94.78 ± 0.01 %. Z. Chen *et al.* estimated the effect of porosity based on the model proposed by Ramakrishnan and Arunachalam [2.26]. According to their model, the Young's modulus of a porous solid can be estimated by the following equation;

$$E_0 = \frac{E_p\{1+(2-3\mu_0)p\}}{(1-p)^2} \tag{2.6}$$

where E_p is the Young's modulus of the porous solid, p is porosity, E_0 is the Young's modulus of the fully dense solid, and μ_0 is the Poisson's ratio of the fully dense solid. Table 1 shows the Young's modulus of the fully dense LSCF6428 extrapolated by using the eq. [] and reported Young's modulus and porosity. The Poisson's ratio of the fully dense solid was assumed to be 0.29, which is the value at room temperature measured by the resonance method. The Young's modulus of the fully dense LSCF6428 extrapolated by using reported Young's modulus and porosity was all in good agreement within experimental error. Thus it can be said the main reason of the discrepancy the Young's modulus of this work and the literatures is the porosity of the samples. In Fig. 2.5, the temperature dependence of the Young's modulus of LSCF6428 measured by the SP tests were also depicted by open circle symbols (○). The Young's modulus measured by SP tests at room temperature was much higher than that by resonance method. It significantly decreased with increasing temperature up to 673 K. Although the data was scattered above 873 K, the Young's modulus seemed to increase with increasing temperature above 873 K. The absolute values were different depending on the measuring method, the significant decrease in the Young's modulus at lower temperatures and the increase at higher temperatures were also observed by a static measurement, namely the SP tests. A similar temperature dependence was observed also under $P(O_2)$ of 1.0 x 10^{-4} bar. However, the temperature at which the elastic moduli started to increase, T_c, was about 100 K lower than that under $P(O_2)$ of 1.0 x 10^{-1} bar. Figure 2.6 shows the temperature dependence of the internal friction of LSCF6428 under $P(O_2)$ of 1.0 x 10^{-1} and 1.0 x 10^{-4} bar. Under $P(O_2)$ of 1.0 x 10^{-1} bar, there seemed to be 2 broad peaks in the temperature range between 423 and 873 K. The internal friction greatly decreased above 823 K. The temperature dependence of the internal friction under $P(O_2)$ of 1.0 x 10^{-4} bar was similar to that under $P(O_2)$ of 1.0 x 10^{-1} bar. But the peak was slightly higher, and the internal friction decreased more drastically above 823 K.

Table 1. The Young's modulus of the fully dense LSCF6428 extrapolated by using the eq. [] and reported Young's modulus and porosity. The Poisson's ratio of the fully dense solid was assumed to be 0.29.

Literature	Young's modulus / GPa	Porosity / %	The extrapolated Young's modulus / GPa
Z. Chen *et al.* [2.24]	**147 ± 3**	**5.22± 0.01**	**173± 4**
Y.-S. Chou *et al.* [2.25]	**152 ± 3**	**4.64 ± 0.22**	**176 ± 2**
This work	**164**	**2**	**175**

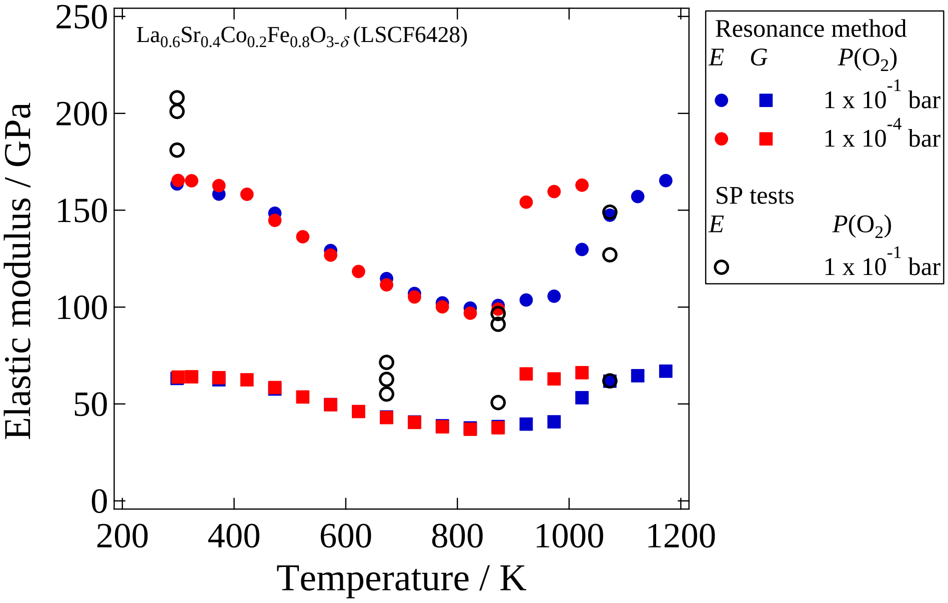

Fig. 2.5. Temperature dependence of the Young's (E) and the shear moduli (G) of $La_{0.6}Sr_{0.4}Co_{0.2}Fe_{0.8}O_{3-\delta}$ (LSCF6428) measured by the resonance method under $P(O_2)$ of 1.0 x 10^{-1} and 1.0 x 10^{-4} bar and the Young's modulus measured by the SP tests under $P(O_2)$ of 1.0 x 10^{-1} bar.

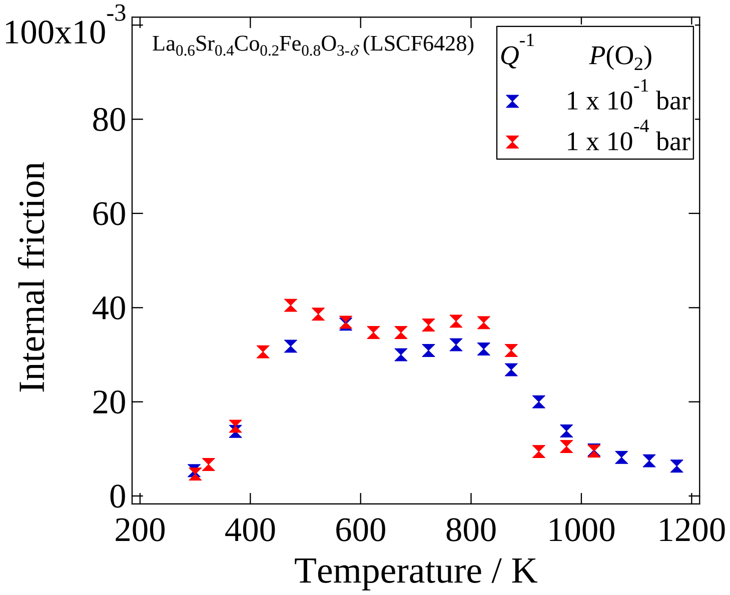

Fig. 2.6. Temperature dependence of the internal friction of $La_{0.6}Sr_{0.4}Co_{0.2}Fe_{0.8}O_{3-\delta}$ (LSCF6428) measured by the resonance method under $P(O_2)$ of 1.0 x 10^{-1} and 1.0 x 10^{-4} bar.

2.3.3 Temperature dependence of E, G, and Q^{-1} of LSCF with other compositions

The Young's and the shear moduli of LSC, LSCF6482, and LSF are shown in Figs. 2.7-2.9 as a function of temperature, respectively. Regardless of $P(O_2)$, they basically showed similar temperature dependence as those of LSCF6428. That is, the elastic moduli significantly decreased with increasing temperature in the low temperature range and drastically increased at intermediate temperatures, and T_c was lower under $P(O_2)$ of 1.0 x 10^{-4} bar than 1.0 x 10^{-1} bar. However, some minor differences were found among the temperature dependence of these compositions. First, T_c was different from material to material, and was higher in order of LSC, LSCF6482, LSCF6428, and LSF. Secondly, the gradual increase before the drastic increase, which was observed with LSCF6428 and LSF, was not detected with LSC and LSCF6482. Figure 2.10 shows the temperature dependence of the internal friction of LSC under $P(O_2)$ of 1.0 x 10^{-1} and 1.0 x 10^{-4} bar. A sharp and pronounced peak was observed in the temperature range between 423 and 573 K. There seemed to be one more shoulder peak at around 600 K. Above 823 K, the internal friction took very small values. The difference between the results under $P(O_2)$ of 1.0 x 10^{-1} and 1.0 x 10^{-4} bar was not so large. However, the temperature at which the internal friction became very small was smaller under 1.0 x 10^{-4} bar than under $P(O_2)$ of 1.0 x 10^{-4} bar. Figures 2.11 and 2.12 show the temperature dependence of the internal friction of LSCF6482 and LSF, respectively, under $P(O_2)$ of 1.0 x 10^{-1} and 1.0 x 10^{-4} bar. Two peaks were observed in the internal friction of LSCF6482 and LSF. One was observed at around 423 K and another was observed at around 700 K. The internal friction of LSCF6482 became very small above 873 K while the internal friction of LSF became very small above 1000 K. As well as LSC, The difference between the results under $P(O_2)$ of 1.0 x 10^{-1} and 1.0 x 10^{-4} bar was not so large, although the temperature at which the internal friction of LSF became very small was smaller under 1.0 x 10^{-4} bar than under $P(O_2)$ of 1.0 x 10^{-4} bar.

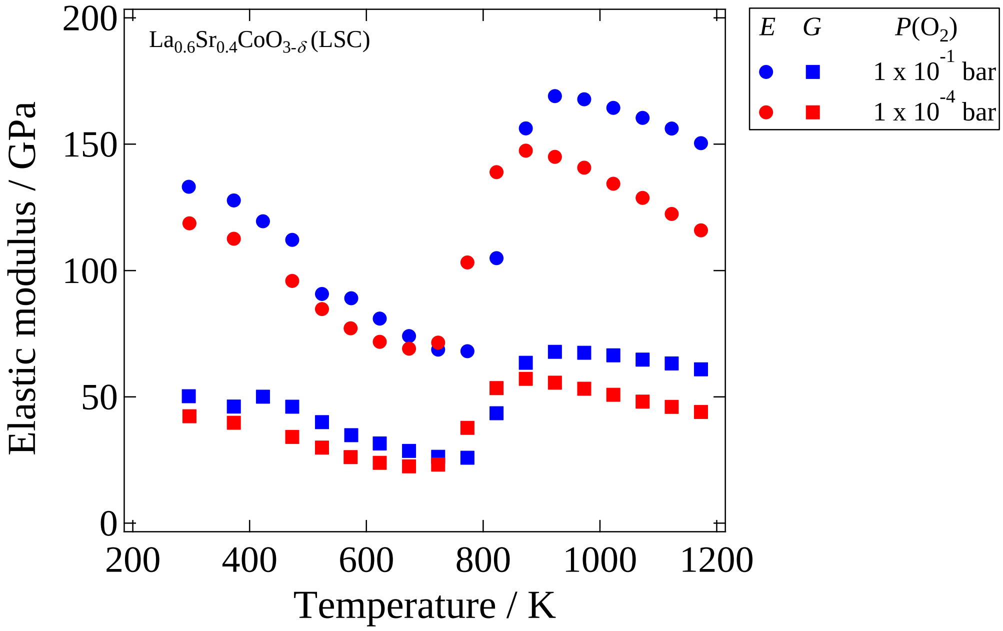

Fig. 2.7. Temperature dependence of the Young's (*E*) and the shear moduli (*G*) of La$_{0.6}$Sr$_{0.4}$CoO$_{3-\delta}$ (LSC) measured by the resonance method under *P*(O$_2$) of 1.0 x 10^{-1} and 1.0 x 10^{-4} bar.

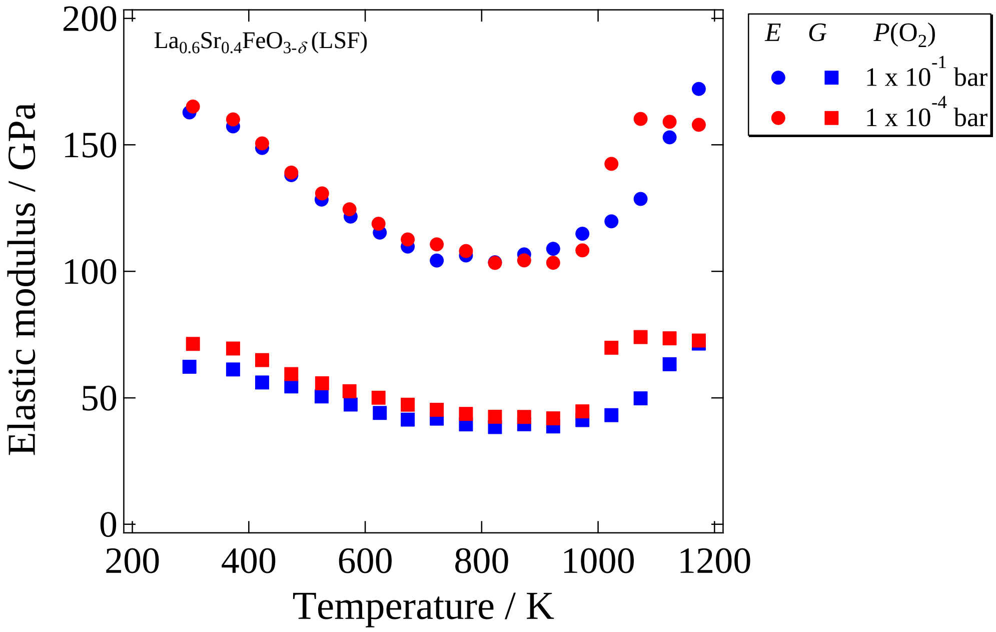

Fig. 2.8. Temperature dependence of the Young's (*E*) and the shear moduli (*G*) of La$_{0.6}$Sr$_{0.4}$FeO$_{3-\delta}$ (LSF) measured by the resonance method under *P*(O$_2$) of 1.0 x 10^{-1} and 1.0 x 10^{-4} bar.

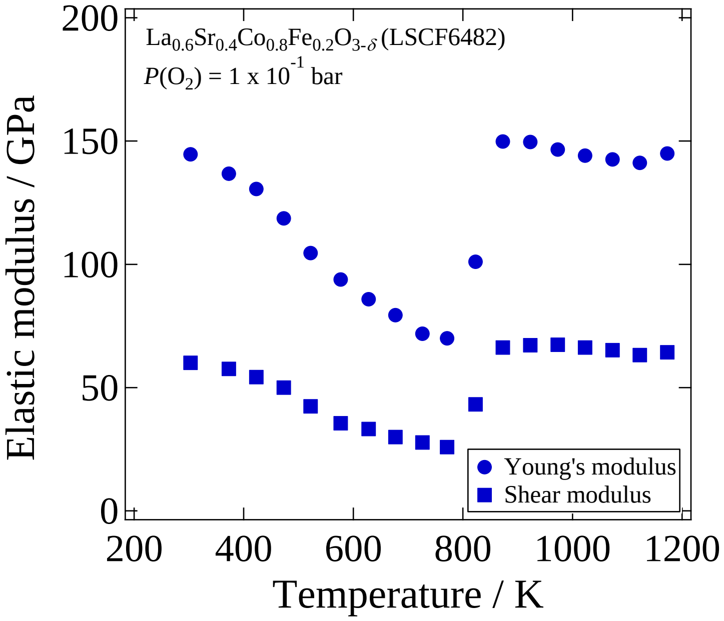

Fig. 2.9. Temperature dependence of the Young's and the shear moduli of $La_{0.6}Sr_{0.4}Co_{0.8}Fe_{0.2}O_{3-\delta}$ (LSCF6482) measured by the resonance method under $P(O_2)$ of 1.0×10^{-1} bar.

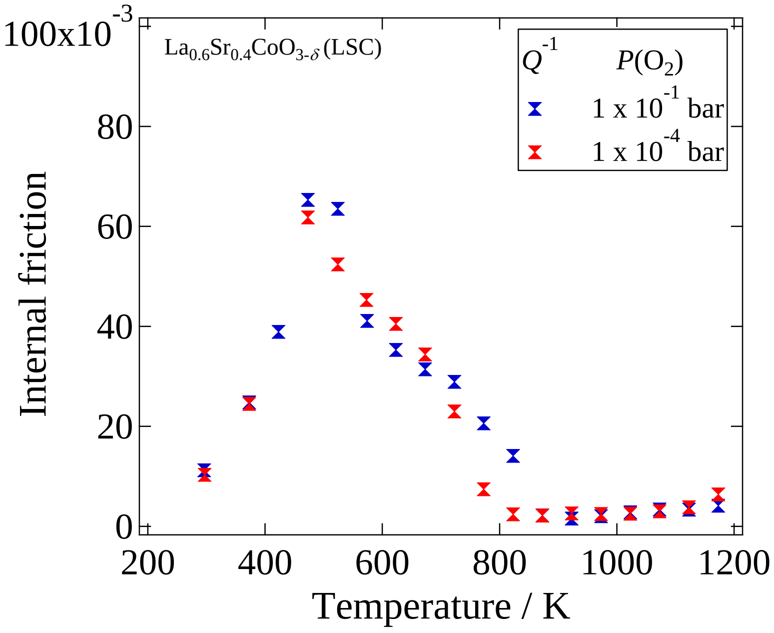

Fig. 2.10. Temperature dependence of the internal friction of $La_{0.6}Sr_{0.4}CoO_{3-\delta}$ (LSC) measured by the resonance method under $P(O_2)$ of 1.0×10^{-1} and 1.0×10^{-4} bar.

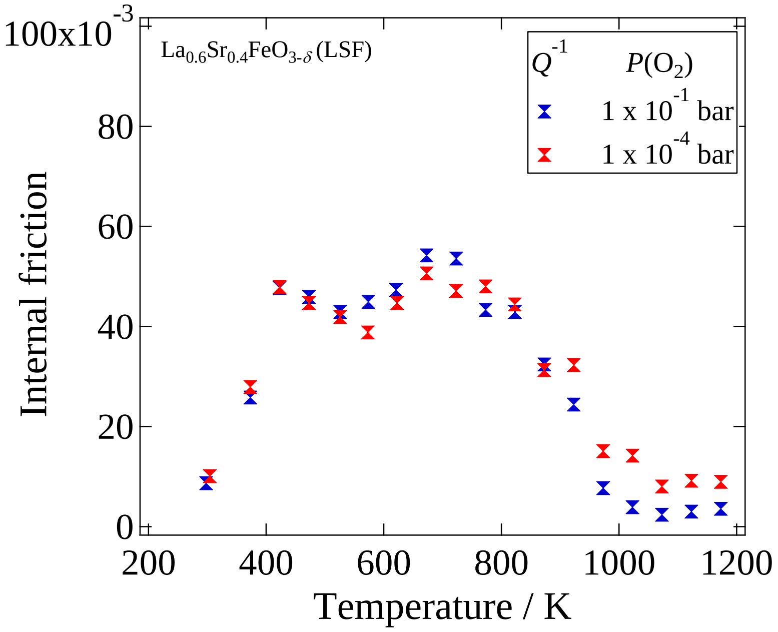

Fig. 2.11. Temperature dependence of the internal friction of $La_{0.6}Sr_{0.4}CoO_{3-\delta}$ (LSF) measured by the resonance method under $P(O_2)$ of 1.0 x 10^{-1} and 1.0 x 10^{-4} bar.

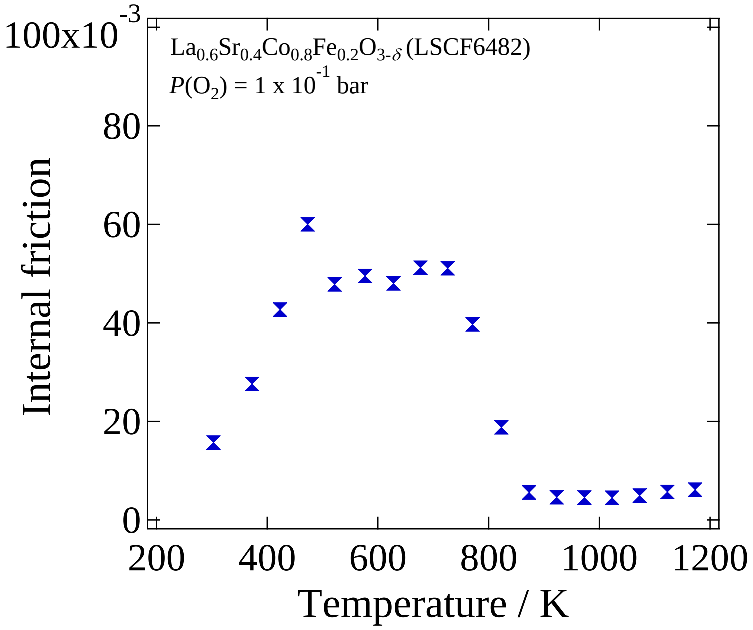

Fig. 2.12. Temperature dependence of the internal friction of $La_{0.6}Sr_{0.4}Co_{0.8}Fe_{0.2}O_{3-\delta}$ (LSCF6482) measured by the resonance method under $P(O_2)$ of 1.0 x 10^{-1} bar.

2.3.4 Temperature Dependence of Poisson's ratio of LSCF

Figure 2.13 shows the Poisson's ratio of LSCF6428 under *P*(O_2) of 1.0 x 10^{-1} and 1.0 x 10^{-4} bar. Under *P*(O_2) of 1.0 x 10^{-1} bar, the Poisson's ratio was almost constant at around 0.3 below 973 K. But it sharply decreased at 1023 K and then became constant at around 0.2. It showed a similar temperature dependence under *P*(O_2) of 1.0 x 10^{-4} bar although the sudden decrease was observed at 873 K. Figure 2.14 shows Poisson's ratios of LSC LSCF6482, and LSF under *P*(O_2) of 1.0 x 10^{-1} bar. The Poisson's ratio of LSF was around 0.35 up to 973 K and decreased above 973 K. The Poisson's ratio of LSC and LSCF6482 was scattered around 0.3 below 773 K. But it decreased at 823 K and became stable at around 0.2, 0.1 above 823 K, respectively. The reason for the scattering is probably the measurement error of the elastic moduli.

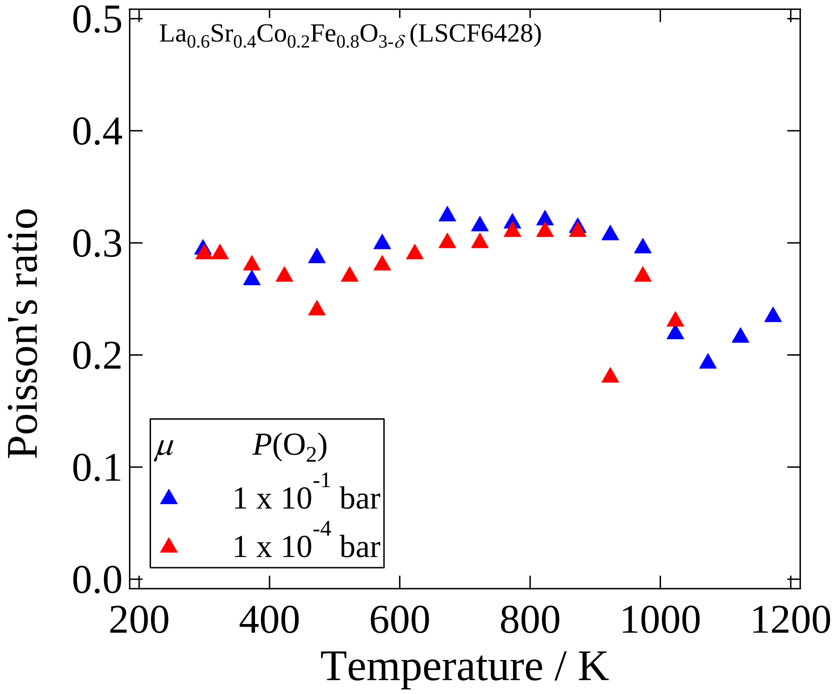

Fig. 2.13. Temperature dependence of Poisson's ratio of $La_{0.6}Sr_{0.4}Co_{0.2}Fe_{0.8}O_{3-\delta}$ (LSCF6428) under *P*(O_2) of 1.0 x 10^{-1} and 1.0 x 10^{-4} bar.

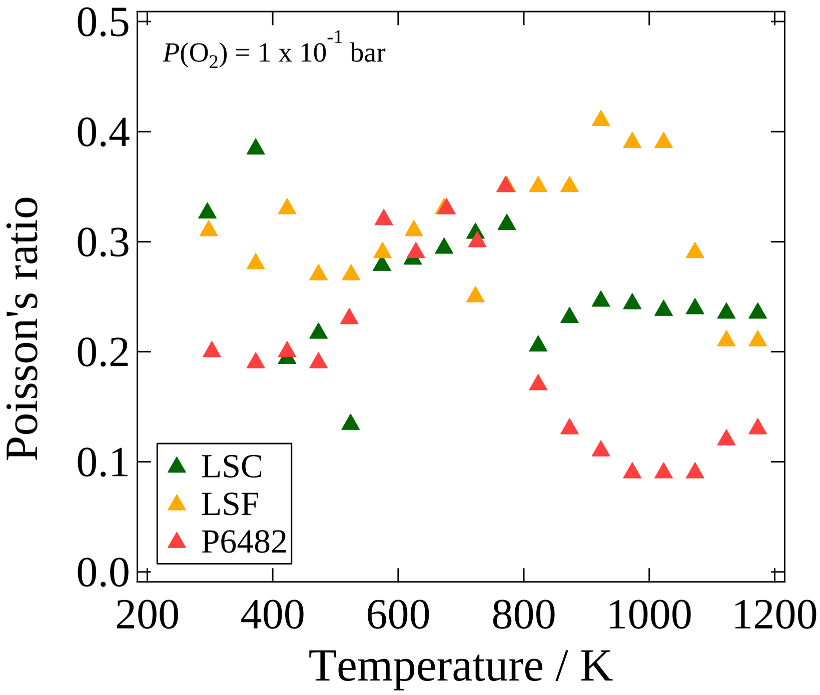

Fig. 2. 14. Temperature dependence of Poisson's ratio of $La_{0.6}Sr_{0.4}CoO_{3-\delta}$ (LSC), $La_{0.6}Sr_{0.4}Co_{0.8}Fe_{0.2}O_{3-\delta}$ (LSCF6482), and $La_{0.6}Sr_{0.4}FeO_{3-\delta}$ (LSF) under $P(O_2)$ of 1.0 x 10^{-1} bar.

2.4 Discussion

2.4.1 Temperature Dependence of Mechanical Properties of LN214

The gradual decrease in the Young's modulus of LN214 with increasing temperature is a typical temperature dependence of the conventional ceramics such as Al_2O_3 [2.27]. This gradual decrease in the Young's modulus with increasing temperature is interpreted to be because of the decrease in the bonding strength due to the thermal expansion [2.27]. This gradual decrease due to the thermal expansion is often described by the following equation [2.27];

$$E = E_0\left[1-3b\frac{T}{T_m}\right] \qquad [2.7]$$

where E is the Young's modulus at an arbitrary temperature, E_0 is the Young's modulus at 0K, b is a constant, T is temperature, T_m is the melting point. The b usually takes the value between 0.02 and 0.05 [2.27]. The temperature dependence of the Young's modulus of LN214 was fitted by the above equation. The fitting curve was shown in the Fig.2.3. The above equation fitted well the temperature dependence of the Young's modulus of LN214. The calculated values of E_0, b, T_m were 177 GPa, 0.05, 2006 K, respectively. The melting point of LN214 is reported to be 1957 K [2.28]. Thus the calculated melting point agreed well with the literature.

2.4.2 Temperature Dependence of E, G, Q-1 of LSCF

A drastic increase in the elastic moduli at intermediate temperatures was reported also with $La_{0.58}Sr_{0.4}Co_{0.2}Fe_{0.8}O_{3-\delta}$ and $La_{0.8}Sr_{0.2}FeO_{3-\delta}$ [2.29, 2.30]. Such an increase in the elastic modulus can be associated with the phase transition [2.31, 2.32]. The crystal structures of LSCF are known to transform from rhombohedral to cubic by a second-order phase transition with increasing temperature [2.14-2.19].

The T_c and the phase transition temperatures of LSCF with each composition reported in literatures are summarized in Table 1 [2.14-2.19]. Since the phase transition temperatures in the literatures were measured in air, T_c under $P(O_2)$ of 1.0 x 10^{-1} bar, which is close to $P(O_2)$ in air, was here compared. Although the reported phase transition temperatures of LSCF are slightly different from literature to literature, T_c seems to comparatively agree with the phase transition temperatures. In the case of LSC and LSF, it is reported that the phase transition temperature becomes lower with decreasing $P(O_2)$ [2.19, 2.33]. Accordingly, T_c also became lower under $P(O_2)$ of 1.0 x 10^{-4} bar than 1.0 x 10^{-1} bar. These facts support the hypothesis that the drastic increase in the elastic moduli is related to the phase transition.

Table 1. Temperatures at which Young's and shear moduli increased, T_c, under $P(O_2)$ of 1.0 x 10^{-1} bar and phase transition temperatures in air.

Composition	T_c / K	Phase transition temperature / K
$La_{0.6}Sr_{0.4}CoO_{3-\delta}$	**773**	**753 [2.15]**
		673-773 [2.16]
$La_{0.6}Sr_{0.4}Co_{0.8}Fe_{0.2}O_{3-\delta}$	**773**	**773 [2.16]**
$La_{0.6}Sr_{0.4}Co_{0.2}Fe_{0.8}O_{3-\delta}$	**973**	**873-973 [2.17]**
$La_{0.6}Sr_{0.4}FeO_{3-\delta}$	**1073**	**1073-1173 [2.18]**
		1173 ≤ [2.19]

The phase transition of LSCF and the following drastic increase in the elastic modulus can be phenomenologically explained by the polynominal Gibbs free energy and the coupling theory [2.32, 2.34]. LSCF has a high symmetry cubic phase (space group: $Pm\bar{3}m$) at higher temperatures and a low symmetry rhombohedral phase (space group: $R\bar{3}c$) at lower temperatures [2.14-2.19]. The phase transition from cubic to rhombohedral phase is followed by the compression of the cubic unit cell and the BO_6 octahedron along the [111] direction and the rotation of the BO_6 octahedron around the three cubic axes [2.35]. The difference in Gibbs free energy between both phases, which determines the stable phase under a certain condition, can be described by some classical thermodynamic parameters, such as temperature, T, pressure, P, chemical composition, N, and an additional parameter, the order parameter, φ. The order parameter specifies the thermodynamic state of the rhombohedral phase [2.34]. In the case of $R\bar{3}c \leftrightarrow Pm\bar{3}m$ transition in LSCF, the rotation angle of the BO_6 octahedron around the three cubic axes can be taken as a primary order parameter [2.36]. In what follows, the difference in Gibbs free energy between both phases is referred to as the excess Gibbs free energy, G_{ex}. The excess Gibbs free energy is often assumed to have a simple polynomial form with coupling terms between the order parameter and the elastic strain, and has to fulfill all symmetry requirements of the material [2.34]. The excess Gibbs free energy for $R\bar{3}c$ ↔ $Pm\bar{3}m$ transition in a perovskite oxide can be written as follows, taking the rotation angle of the BO_6 octahedron around the three cubic axes as a primary order parameter [2.32];

$$\begin{aligned} &G_{ex}(\varphi,\mathbf{e},T) \\ &= \frac{1}{2}\mathrm{A}(T-T_{\mathrm{c}})\varphi^2 + \frac{1}{4}\mathrm{B}\varphi^4 + \frac{1}{6}(C_{11}{}^{o} + 2C_{12}{}^{o})(e_1+e_2+e_3)^2 + \frac{3}{2}C_{44}{}^{o}e_4{}^2 + \lambda_1(e_1+e_2+e_3)\varphi^2 + \lambda_2 e_4\varphi^2 \end{aligned} \qquad [2.8]$$

where A, B, λ_1, λ_2 are constants which are independent of temperature, T_c is a critical temperature, $C_{11}{}^{\mathrm{o}}$, $C_{12}{}^{\mathrm{o}}$, and $C_{44}{}^{\mathrm{o}}$ are the elastic constants of the cubic LSCF, **e** is a strain tensor, e_1, e_2, e_3, and e_4, are elastic strains. In the above equation, the effects of pressure, *P*, and chemical composition, *N*, were ignored since our main concern is the effect of temperature and the other parameters, φ and **e**. The coupling terms mean the external stress can be relaxed by the change in the primary order parameter [2.34]. The equilibrium condition with respect to φ under a constant strain at a constant temperature is given by [2.34];

$$\left.\frac{\partial G_{ex}(\varphi,\mathbf{e},T)}{\partial\varphi}\right|_{\mathbf{e},T} = 0 \qquad [2.9]$$

Moreover, the elastic constants of the rhombohedral phase, C_{ij}, can be expressed by the following equation [2.37];

$$C_{ij} = C_{ij}^0 - \sum_m \frac{\partial^2 G_{ex}}{\partial e_i \partial\varphi_m} R_{kl} \frac{\partial^2 G_{ex}}{\partial e_k \partial\varphi_m} \qquad [2.10]$$

The matrix R_{kl} is given by;

$$R_{kl}^{-1} = \left[\frac{\partial^2 G_{ex}}{\partial\varphi_k \partial\varphi_l}\right] \quad (k,l = 1,2,3,4,5,6) \qquad [2.11]$$

Substituting the eq. [2.8] into [2.10], the elastic constant of the rhombohedral phase, C_{11}, for instance, can be obtained as follows;

$$C_{11} = C^0{}_{11} - \frac{2}{3}\left(C^0{}_{11} - C^0{}_{12} + \frac{3\lambda_1{}^2}{\mathrm{B}}\right) \qquad [2.12]$$

The above equation suggests the elastic constant of the rhombohedral phase can be reduced by the relaxation of the primary order parameter. And it abruptly changes from C_{11} to C_{11}^0 at the phase transition temperature. The phase transition in other materials such as the $R\bar{3}c \leftrightarrow Pm\bar{3}m$ transition in $LaAlO_3$ and the $I4/mcm \leftrightarrow Pm\bar{3}m$ transition in $SrTiO_3$ have been successfully explained by the similar argument [2.31, 2.32].

With LSC, LSCF6482, and LSF, the Young's and the shear moduli showed the gradual decrease after the drastic increase. Such a gradual decrease can be explained as follows. LSCF expands the crystal lattice with increasing temperature, *i.e.* thermal expansion, as conventional ceramics do. In addition, LSCF shows a significant change in the oxygen nonstoichiometry by the formation of oxygen vacancies at higher temperatures. The amount of oxygen vacancies increases with increasing temperature. An increase of oxygen vacancies leads to the expansion of the lattice, *i.e.* chemical expansion. Both thermal and chemical expansions reduce the bond strength, and thus decrease the elastic moduli, with increasing temperature [2.10]. Furthermore, the formation of oxygen vacancies leads to the decrease in the average valence of cations as well as disappearance of a part of chemical bonds between oxygens and cations. These also may reduce the bonding strength in the lattice, and the elastic moduli [2.10].

At lower temperatures up to about 800 K, the Young's and the moduli of LSCF decreased by 35-50 % of the initial value at room temperature. In this temperature range, the variation of the oxygen nonstoichiometry is negligibly small. In addition, such a considerable decrease cannot be explained only by the thermal expansion. In the temperature range in which the significant decrease was observed, several peaks were also observed in the internal friction of LSCF. Huang *et al.* also reported that the internal friction of $La_{0.58}Sr_{0.4}Co_{0.2}Fe_{0.8}O_{3-\delta}$ showed comparatively larger values and had several peaks in the temperature range between 400 and 1000 K [2.29]. Such a large internal friction may indicate ferroelasticity of LSCF. It is reported that rhombohedral $LaCoO_3$-based oxides exhibit a ferroelastic behavior [2.38-2.40]. In rhombohedral $LaCoO_3$-based oxides, there can exist 4 domain states which have a different rhombohedral principal axis. When a stress which is higher than a certain level is applied, a part of domains switch their state to the other. Such a ferroelastic domain switching can relieve the stress and thus be the cause of the decrease in the elastic modulus. However, further investigation is needed to identify the main cause of the decrease in the elastic modulus of LSCF at low temperatures.

2.4.3 Poisson's ratio of LSCF

For all materials investigated in this work, the temperature at which the Poisson's ratio decreased corresponded to the temperature at which the elastic moduli drastically increased. This suggests that the decrease in the Poisson's ratio is considered to be caused by the phase transition. On the other hand, at temperatures except around the phase transition temperatures, the Poisson's ratios were almost independent of temperature. These indicate that the Poisson's ratio is insignificantly affected by the thermal and the chemical expansion, and the formation of oxygen vacancy.

2.5. Conclusion

The Young's and the shear moduli, the internal friction, and the Poisson's ratio of La_2NiO_4 (LN214), $La_{0.6}Sr_{0.4}CoO_{3-\delta}$ (LSC), $La_{0.6}Sr_{0.4}Co_{0.8}Fe_{0.2}O_{3-\delta}$ (LSCF6482), $La_{0.6}Sr_{0.4}Co_{0.2}Fe_{0.8}O_{3-\delta}$ (LSCF6428), and $La_{0.6}Sr_{0.4}FeO_{3-\delta}$ (LSF) were evaluated as a function of temperature under a constant $P(O_2)$ of 1×10^{-1} or 1×10^{-4} bar by using the resonance method and the small punch testing method. Whereas the Young's and the shear moduli of LN214 monotonically decreased with increasing temperature and the internal friction was very small, the Young's and the shear moduli of LSCF significantly decreased with increasing temperature at lower temperatures and drastically increased at intermediate temperatures. The Young's modulus of LSC, LSCF6482, and LSF gradually decreased with increasing temperature at further higher temperatures. The internal friction had one or two peak/peaks in the temperature range in which the Young's modulus significantly decreased. The temperature at which the Poisson's ratio of LSCF6428, LSC, and LSF decreased corresponded to the temperature at which the elastic moduli drastically increased. The gradual decrease in the Young's modulus of LN214 is possibly due to the thermal expansion. The abrupt change in the Young's and the shear moduli of LSCF at intermediate temperatures is considered to be associated with the phase transition. The abrupt change in the Young's and the shear moduli were phenomenologically explained based on the polynominal Gibbs free energy and the coupling theory. It was suggested that the significant decrease in the Young's and the shear moduli of LSCF at lower temperatures was related with the ferroelastic domain switching. The gradual decrease in the Young's and the shear moduli of LSCF above the phase transition temperature may be associated with the decrease in the bonding strength due to the thermal and the chemical expansion.

2.6. References

[2.1] A. Mai, V. A.C. Haanappel, S. Uhlenbruck, F. Tietz, and D. Stöver, *Solid State Ionics*, **176**, 1341(2005).

[2.2] J. W. Fergus, *J. Power Sources*, **162**, 30 (2006).

[2.3] R. Sayers, M. Rieu, P. Lenormand, F. Ansart, J.A. Kilner, S.J. Skinner, *Solid State Ionics*, **192**, 531 (2001).

[2.4]X. Tan, Y. Liu, K. Li, *AIChE journal*, **51**, 1991 (2005).

[2.5] K. Hosoi, M. Ito, M. Fukae, *ECS Transactions*, **35**, 11 (2011).

[2.6] J. Malzbender, R. W. Steinbrech and L. Singheiser, *Fuel Cells*, **9**, 785 (2009).

[2.7] K. Sato, T. Hashida, K. Yashiro, H. Yugami, T. Kawada and J. Mizusaki, *J. Ceram. Soc. Jpn.*, **113**, 562 (2005).

[2.8] T. Kushi, K. Sato, A. Unemoto, S. Hashimoto, K. Amezawa and T. Kawada, *J. Power Sources*, **196**, 7989 (2011).

[2.9] S. Giraud and J. Canel, *J. Eur. Ceram. Soc.*, **28**, 77 (2008).

[2.10]K. Amezawa, T. Kushi, K. Sato, A. Unemoto, S. Hashimoto and T. Kawada, *Solid State Ionics*, **198**, 32 (2011).

[2.11]T. Nakamura, K. Yashiro, K. Sato and J. Mizusaki, *Phys. Chem. Chem. Phys.*, **11**, 3055 (2009).

[2.12]A. Esquirol, N. P. Brandon, J. A. Kilner, and M. Mogensen, *J. Electrochem. Soc.*, **151**, A1847 (2004).

[2.13]S. Hashimoto, Y. Fukuda, M. Kuhn, K. Sato, K. Yashiro, J. Mizusaki, *Solid State Ionics*, **181**, 1713 (2010).

[2.14] M. Kuhn, S.Hashimoto, K.Sato, K.Yashiro, J.Mizusaki, *J. Solid Oxide Chem.*, **197**, 38 (2013).

[2.15] J. Mastin, M.-A. Einarsrud and T. Grande, *Chem. Mater.*, **18**, 6047 (2006).

[2.16] S. Wang, M. Katsuki, M. Dokiya and T. Hashimoto, *Solid State Ionics*, **159**, 71 (2003).

[2.17] B. X. Huang, J. Malzbender, R. W. Steinbrech and L. Singheiser, *Solid State Ionics*, **180**, 241 (2009).

[2.18] A. Fossdal, M. Menon, I. Wærnhus, K. Wiik, M.-A. Einarsrud and T. Grande, *J. Am. Ceram. Soc.*, **87**, 1952 (2004).

[2.19] M. Kuhn, S. Hashimoto, K. Sato, K. Yashiro and J. Mizusaki, *Solid State Ionics*, **195**, 7 (2011).

[2.20] Japanese Industrial Standards, ‘Test Method for Young’s Modulus of Metallic

Materials at Elevated Temperature,' JIS Z 2280, 1993.

[2.21] Japanese Industrial Standards, 'Test Method for Young's Modulus of Fine Ceramics,' JIS R 1602, 1994.

[2.22] K. Sato, T. Miyasaka, S. Watanabe, and T. Hashida, ECS Transactions, **57** (1) 753 (2013).

[2.23] S. Okuda, M. Saito, T. Hashida, H. Takahashi, *Trans. JSME(A), **57**, 940 (1991).*

[2.24] Y.-S. Chou, J. W. Stevenson, T. R. Armstrong, and L. R. Pederson, *J. Am. Ceram. Soc.*, **83**, 1457 (2000).

[2.25] Z. Chen, X. Wang, V. Bhakhri, F. Giuliani, and A. Atkinson, *Acta Mater.*, 61, 5720 (2013).

[2.26] N. Ramakrishnan and V. S. Arunachalam, *J. Mater. Sci.*, **25**, 3930 (1990).

[2.27] O. Kamigaito and N. Kamiya, *セラミックスの物理*, pp. 76-78, 内田老鶴圃, (1998).

[2.28] M. Zinkevich, F. Aldinger, *J. Alloys Compd*., **375**, 147 (2004).

[2.29] B. X. Huang, J. Malzbender and R. W. Steinbrech, *J. Mater. Res.*, **26**, 1388 (2011).

[2.30] A. Julian, E. Juste, P. M. Geffroy, N. Tessier-Doyen, P. Del Gallo, N. Richet and T. Chartier, *J. Eur. Ceram. Soc.*, **29**, 2603 (2009).

[2.31] J. F. Scott and H. Ledbetter, *Z. Phys. B*, **104**, 635 (1997).

[2.32] M. A. Carpenter, S. V. Sinogeikin and J. D. Bass, *J. Phys. Condens. Matter*, **22**, 035404 (2010).

[2.33] A. Mineshige, M. Kobune, S. Fujii, Z. Ogumi, M. Inaba, T. Yao and K. Kikuchi, *J. Solid State Chem*, **142**, 374 (1999).

[2.34] E. K. H. Salje, *Phase transitions in ferroelastic and co-elastic crystals Student Edition*, pp. 28-43, Cambridge University Press, New York, 1993.

[2.35] A. M. Glazer, *Acta Crystallogr. A*, **31**, 756 (1975).

[2.36] S. A. Hayward, F. D. Morrison, S. A. T. Redfern, E. K. H. Salje, J. F. Scott, K. S. Knight, S. Tarantino, A. M. Glazer, V. Shuvaeva, P. Daniel, M. Zhang, and M. A. Carpenter, *Phys. Rev. B*, **72**, 054110 (2005).

[2.37] J. C. Slonczewski and J. Thomas, *Phys. Rev. B*, **1**, 3599 (1970).

[2.38] P. E. Vullum, R. Holmestad, H. L. Lein, J. Mastin, M.–A. Einarsrud, and T. Grande, *Adv. Mater.*, **19**, 4399 (2007).

[2.39] W. Araki and J. Malzbender, *J. Euro. Ceram. Soc.*, **33**, 805 (2013).

[2.40] S. Faaland, T. Grande, M.-A. Einarsrud, P. E. Vullum and R. Holmestad, *J. Am. Ceram. Soc.*, **88**, 726 (2005).

Chapter 3

The text presented in this Chapter is reproduced in part with permission from:
Y. Kimura, T. Kushi, S. Hashimoto, K. Amezawa and T. Kawada, , *J. Am. Ceram. Soc.*, **95**, 2608 (2012).

Influence of oxygen defects on the mechanical properties of perovskite and related oxides

3.1 Introduction

As mentioned in the previous chapter, the knowledge of the mechanical properties of perovskite and related oxides for energy conversion devices, especially at high temperatures and under controlled atmospheres, is necessary for suppressing the mechanical degradations. The mechanical properties of those oxides may change at high temperatures and under controlled atmospheres since the defect concentration and crystal structure can change in those conditions. For the above background, the elastic modulus and the internal friction of $La_{0.6}Sr_{0.4}Co_{0.2}Fe_{0.8}O_{3-\delta}$ (LSCF6428), $La_{0.6}Sr_{0.4}CoO_{3-\delta}$ (LSC), $La_{0.6}Sr_{0.4}Co_{0.8}Fe_{0.2}O_{3-\delta}$ (LSCF6482), $La_{0.6}Sr_{0.4}FeO_{3-\delta}$ (LSF), and La_2NiO_4 (LN214) were evaluated at high temperatures under controlled atmospheres by using the resonance method in the chapter 2. It was found that the Young's and the shear moduli of LSC, LSCF6482, and LSF gradually decreased with increasing temperature at high temperatures. It was suggested that this gradual decrease in the Young's and the shear moduli at high temperatures was associated with the thermal expansion, the formation of oxygen vacancies and the following decrease in the bonding strength due to the chemical expansion. Such a change in the Young's and the shear moduli which is related with the change in the oxygen defect concentration is also reported with other oxides [3.1-3.4]. For instance, the Young's modulus of gadolinium doped ceria is independent of oxygen partial pressure, $P(O_2)$, in the oxidizing atmospheres. On the other hand, it noticeably decreases with decreasing $P(O_2)$ in the reducing atmospheres, in which the oxygen vacancy concentration significantly increases with decreasing $P(O_2)$ [3.1-3.3]. Conversely, the room temperature elastic modulus of $La_{1-x}Sr_xCrO3$ ($x \leq 0.24$) is reported to increase when the material is preliminarily annealed under low oxygen partial pressure, compared to the one annealed under high oxygen partial pressure. The cause of this increase is considered to be due to the structural change to the lattice [3.4]. Thus the change in oxygen partial pressure, more strictly speaking, the change in the defect concentration, does have influence on the mechanical properties of some oxides. However, in most studies, the measurements are performed in air and at room temperature, using samples annealed under controlled atmospheres [3.2, 3.4]. On the other hand, the studies in which the mechanical properties are directly measured at high temperatures under controlled atmospheres are limited [3.1, 3.3]. It is possible that the sample surfaces are partially oxidized when the sample is annealed and cooled to room temperature. This partially oxidized layer can affect the mechanical properties and prevent the accurate evaluation. Therefore, the influence of oxygen defects on the mechanical properties should be directly evaluated at high temperatures and controlled atmospheres.

In this study, the $P(O_2)$ dependence of mechanical properties of LSCF6428 and LN214 were directly evaluated at high temperatures in order to understand the influence of the defect concentration on the mechanical properties. These two materials were chosen for the evaluation since these materials have different kinds of oxygen defects. That is, LSCF6428 is known to show a comparatively large oxygen deficient composition [3.5]. On the other hand, LN214 is known to show a large oxygen excess composition [3.6].

3.2 Experimental

The $P(O_2)$ dependence of mechanical properties of LSCF6428 and LN214 was measured by the resonance method. The detailed procedure for the sample preparation and the resonance measurements is described in the chapter 2. $P(O_2)$ was changed from 1 x 10^{-1} to 1 x 10^{-4} bar at a constant temperature of 873, 973, 1073 and 1173 K. $P(O_2)$ around the sample was controlled by flowing a mixture gas of O_2 and Ar, and monitored by an yttria-stabilized zirconia oxygen sensor. Resonance measurements were repeated until the measured value of the elastic moduli reached a constant while keeping temperature and $P(O_2)$ constant, *i.e.*, until the sample equilibrated with the applied temperature and $P(O_2)$. The time required for the equilibration was typically 5-24 hours, and was longer at lower temperature and $P(O_2)$.

3.3 Results and discussion

3.3.1 $P(O_2)$ dependence of the mechanical properties of LSCF6428

Figure 3.1 shows the Young's and the shear moduli of LSCF6428 as a function of $P(O_2)$ at 873, 973, 1073, and 1173 K. The Young's and the shear moduli showed a different $P(O_2)$ dependence at each temperature. At 873 K, the Young's and the shear moduli were almost independent of $P(O_2)$. On the other hand, they considerably increased with decreasing $P(O_2)$ at 973 K. At 1073 K, the Young's and the shear moduli slightly increased with decreasing $P(O_2)$ down to 5 $\times 10^{-3}$ bar and then decreased in further lower $P(O_2)$. At 1173 K, they monotonically decreased with decreasing $P(O_2)$.

Figure 3.2 shows the oxygen nonstoichiometry of LSCF6428 as a function of $P(O_2)$ at 873, 973, and 1073 K taken from the literature [3.5]. At each temperature, the oxygen vacancy concentration increases with decreasing $P(O_2)$. It increases more significantly at higher temperature.

As previously seen in the chapter 2, the Young's and the shear moduli of LSCF6428 are considered to be influenced by the phase transition and the variation in the oxygen vacancy concentration. It appears that the phase transition temperature of LSCF6428 becomes lower with decreasing $P(O_2)$, more precisely speaking, with increasing the oxygen vacancy concentration [3.7, 3.8]. Therefore, at a constant temperature, the gradual phase transition from rhombohedral to cubic tends to proceed when $P(O_2)$ decreases. The Young's and the shear moduli are considered to increase with the phase transition from rhombohedral to cubic. On the other hand, the increase in the oxygen vacancy concentration is considered to slightly decrease the Young's and the shear moduli. Considering the above discussions, the $P(O_2)$ dependence of the Young's and the shear moduli in Fig. 3.1 can be explained as follows; At 873 K, the crystal structure as well as the oxygen vacancy concentration do not significantly change with $P(O_2)$. Therefore, the elastic moduli are independent of $P(O_2)$. At 973 K, the phase transition is not completed and the oxygen vacancy concentration increases with decreasing $P(O_2)$. Therefore, it is considered that the crystal structure gradually approaches to cubic and thus the Young's and the shear moduli increase with decreasing $P(O_2)$. At 1073 K, it is supposed that the crystal structure is close to cubic but the transition may not fully completed yet under higher $P(O_2)$. The Young's and the shear moduli thus increase with decreasing $P(O_2)$ under higher $P(O_2)$ due to the gradual phase transition. Once the phase transition is completed, the Young's and the shear moduli decrease with decreasing $P(O_2)$ due to the increase in the oxygen vacancy concentration. This is probably the situation under lower $P(O_2)$ at 1073 K. At sufficiently high temperatures, *i.e.* 1173 K, the phase transition is completed even under high $P(O_2)$. Then, at 1173 K, the Young's and the shear moduli are influenced only by the variation in the oxygen vacancy concentration. An increase of oxygen vacancies leads to the expansion of the lattice, *i.e.* chemical expansion. This chemical expansion reduce the bond strength, and thus decrease the Young's and the shear moduli [3.1]. Furthermore, the formation of oxygen vacancies leads to the decrease in the average valence of cations as well as disappearance of a part of chemical bonds between oxygens and cations. These also may reduce the bonding strength in the lattice, and the Young's and the shear moduli [3.1].

Figure 3.3 shows the Poisson's ratio of LSCF6428 as a function of $P(O_2)$. At 873 and 1173 K, it was almost independent of $P(O_2)$ and was around 0.3 and 0.2, respectively. On the other hand, it decreased with decreasing $P(O_2)$ at 973 K. At 1073 K, it slightly decreased with decreasing $P(O_2)$ down to 1.0 x 10^{-2} bar and became constant at around 0.2 under further lower $P(O_2)$. Comparing to the $P(O_2)$ dependence of the Young's and the shear moduli, it seems that the Poisson's ratio is affected by the phase transition but not significantly by the change in the oxygen vacancy concentration.

Figure 3.4 shows the internal friction of LSCF6428 as a function of $P(O_2)$. At 873 K, the internal friction showed comparatively larger values compared to the other temperatures, and it slightly decreased with decreasing $P(O_2)$. At 973 K, the internal friction slightly decreased with decreasing $P(O_2)$. At 1073 and 1173 K, the internal friction showed small values and almost independent of $P(O_2)$. At 873 K, the crystal structure of LSCF6428 is rhombohedral while it is cubic above 1073 K [3.9]. At 973 K, it seems that the phase transition is not completed and the crystal structure gradually approaches from rhombohedral to cubic with decreasing $P(O_2)$. Thus the internal friction showed larger values when the crystal structure was rhombohedral compared to the values when the crystal structure was cubic. One possible reason why the internal friction showed larger values is the energy loss due to the ferroelastic domain switching [3.10]. However, the interpretation of the large values in the internal friction needs further investigation.

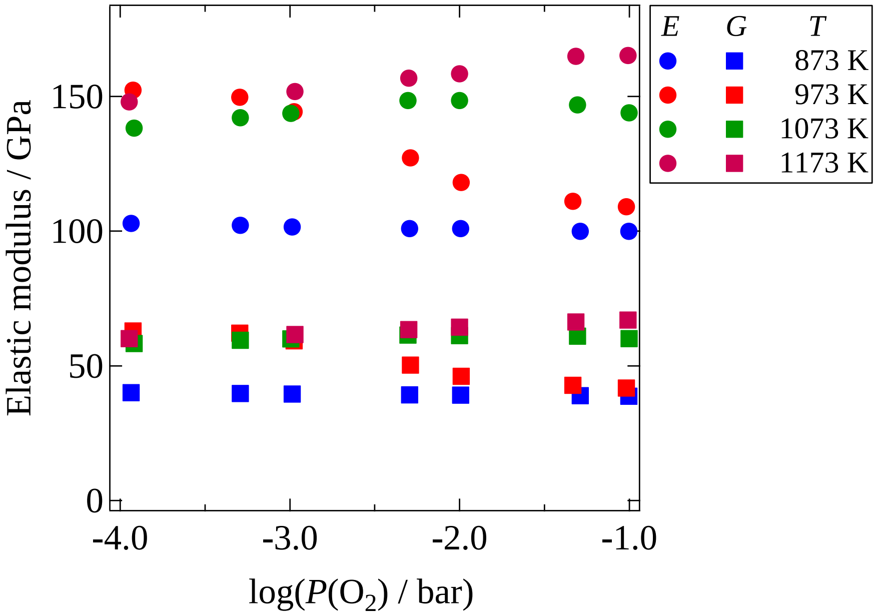

Fig. 3.1. $P(O_2)$ dependence of Young's (E) and shear (G) moduli of $La_{0.6}Sr_{0.4}Co_{0.2}Fe_{0.8}O_{3-\delta}$ (LSCF6428) at 873, 973, 1073 and 1173 K.

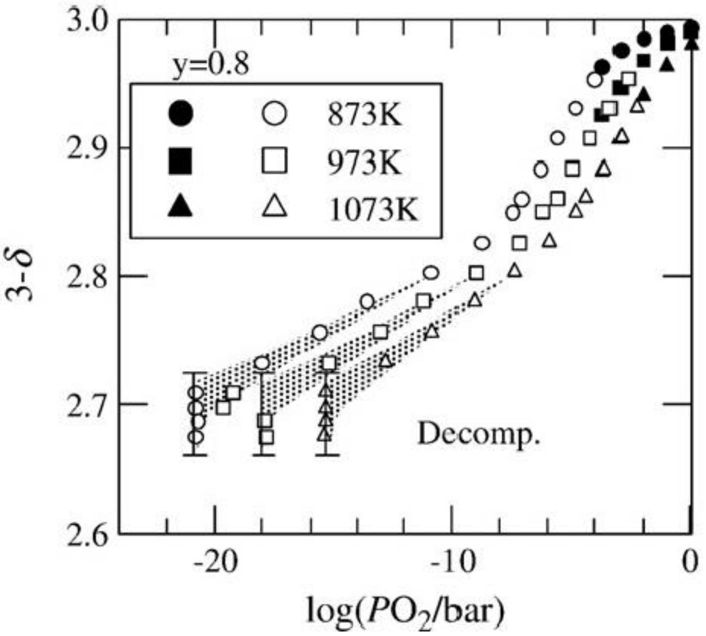

Fig.3.2 Oxygen nonstoichiometry of $La_{0.6}Sr_{0.4}Co_{0.2}Fe_{0.8}O_{3-\delta}$ (LSCF6428) as a function of $P(O_2)$ at 873, 973, and 1073 K taken from the literature [3.5].

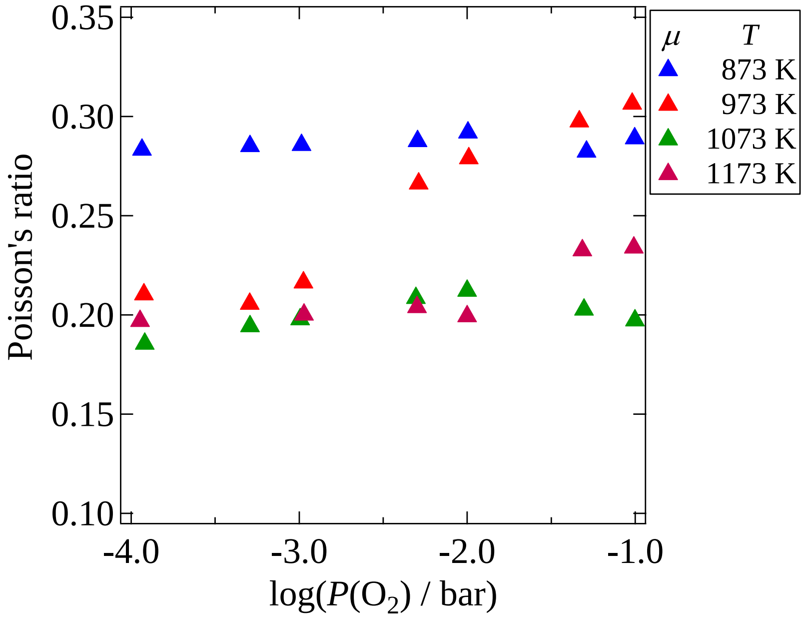

Fig. 3.3. $P(O_2)$ dependence of Poisson's ratio, μ, of $La_{0.6}Sr_{0.4}Co_{0.2}Fe_{0.8}O_{3-\delta}$ (LSCF6428) at 873, 973, 1073, and 1173 K.

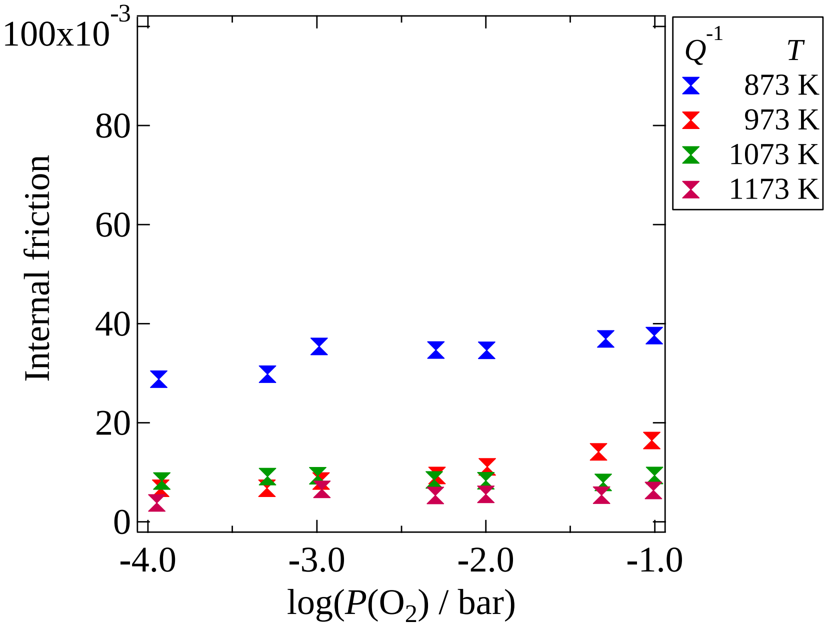

Fig. 3.4. $P(O_2)$ dependence of internal friction, Q^{-1}, of $La_{0.6}Sr_{0.4}Co_{0.2}Fe_{0.8}O_{3-\delta}$ (LSCF6428) at 873, 973, 1073, and 1173 K.

3.3.2 $P(O_2)$ dependence of the mechanical properties of LN214

Figure 3.5 shows the Young's and the shear moduli of LN214 as a function of $P(O_2)$ at 873, 973, and 1073 K. In contrast to the results of LSCF6428, the Young's and the shear moduli were almost independent of $P(O_2)$ at each temperature. Figure 3.6 shows the $P(O_2)$ dependence of the Poisson's ratio of LN214 at 873, 973, and 1073 K. Although the Poisson's ratio at 873 K was slightly higher than the one at the other temperatures, it was almost independent of $P(O_2)$ at all measuring temperatures. The internal friction was also independent of $P(O_2)$ and showed small values irrespective of the measuring temperature as shown in Fig.3.7. LN214 is formed by stacking the rock salt layer (AO) and the perovskite layer (ABO_3) alternatively. Above 873 K and in the $P(O_2)$ range between 1 x 10^{-4} and 1 x 10^{-1} bar, LN214 is known to have tetragonal symmetry [3.11]. Therefore, it is considered that the $P(O_2)$ dependence of the mechanical properties of LN214 are not influenced by the crystal structure change. Futhermore, LN214 has an excess oxygen composition. Figure 3.8 shows the oxygen nonstoichiometry of LN214 as a function of $P(O_2)$ at 873, 973, 1073, and 1173 K, which is taken from the literature [3.6]. The amount of excess oxygen atoms is greater at lower temperatures and decreases with decreasing $P(O_2)$. This change in the oxygen nonstoichiometry of LN214 leads to the change in the lattice parameters [3.11]. Since LN214 has tetragonal symmetry, it has two lattice parameters *e.g.* the lattice constants, a and c. Figures 3.9 (a)-(c) show the lattice parameters of LN214 as a function of $P(O_2)$; (a) a vs. $P(O_2)$, (b) c vs. $P(O_2)$, and (c) cell volume vs. $P(O_2)$, respectively, which are taken from the literature [3.11]. The a of LN214 increases while the c decreases with decreasing $P(O_2)$ at each temperature. Considering the above, the reason why the Young's and the shear moduli of LN214 were independent of $P(O_2)$ can be interpreted as follows. As previously mentioned in the section of LSCF6428, the increase in the lattice constant results in the decrease in the bonding strength and thus is considered to decrease the elastic modulus. Conversely, the decrease in the lattice constant is considered to lead to the increase in the elastic modulus. Taking the above into account, it is considered that the elastic constants, C_{11} and C_{22}, of LN214 increase while C_{33} decreases with decreasing $P(O_2)$. Since the sample of LN214 is polycrystalline, the influence of the change in each elastic constant on the Young's and the shear moduli is averaged. Therefore the Young's and the shear modulus are macroscopically independent of the changes in the amount of excess oxygen atoms.

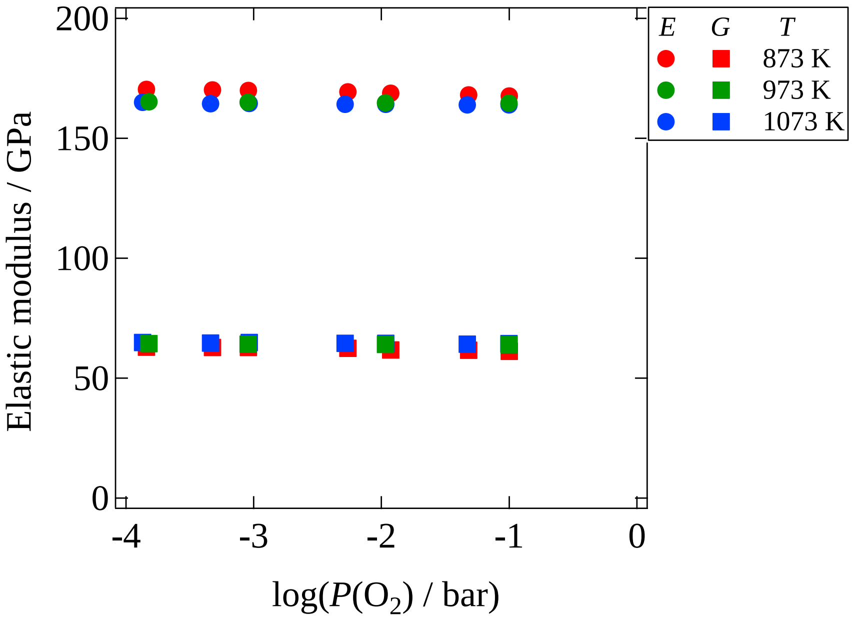

Fig. 3.5. $P(O_2)$ dependence of Young's (*E*) and shear (*G*) moduli of $La_2NiO_{4+\delta}$ (LN214) at 873, 973, and 1073 K.

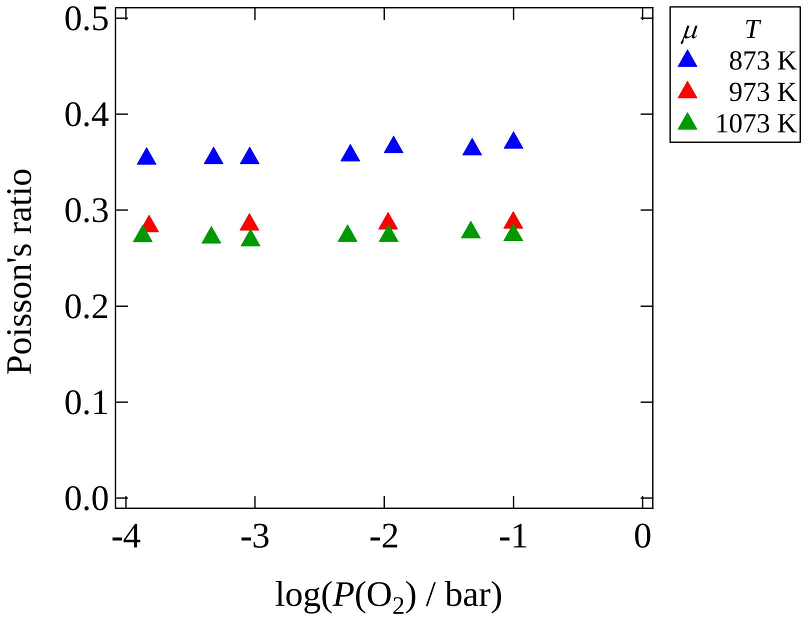

Fig. 3.6. $P(O_2)$ dependence of Poisson's ratio, μ, of $La_2NiO_{4+\delta}$ (LN214) at 873, 973, 1073, and 1173 K.

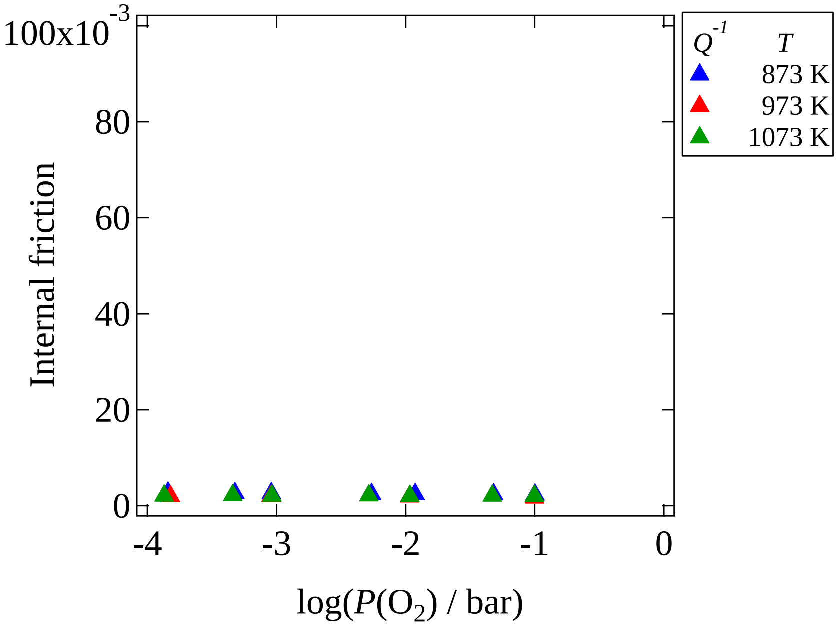

Fig. 3.7. $P(O_2)$ dependence of internal friction, Q^{-1}, of $La_2NiO_{4+\delta}$ (LN214) at 873, 973, 1073, and 1173 K.

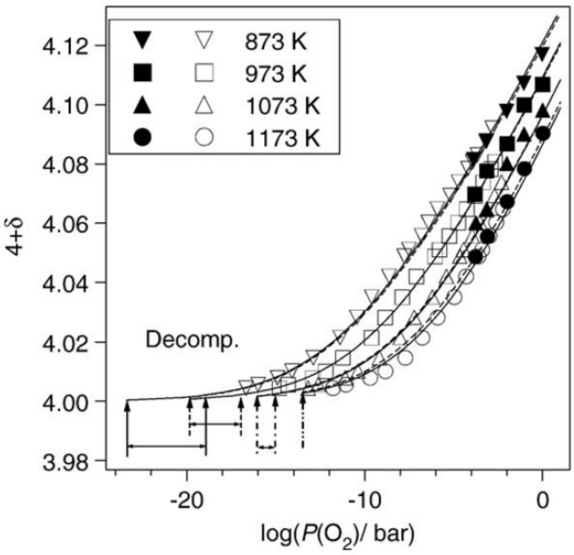

Fig.3.8 Oxygen nonstoichiometry of $La_2NiO_{4+\delta}$ (LN214) taken from the literature [3.6].

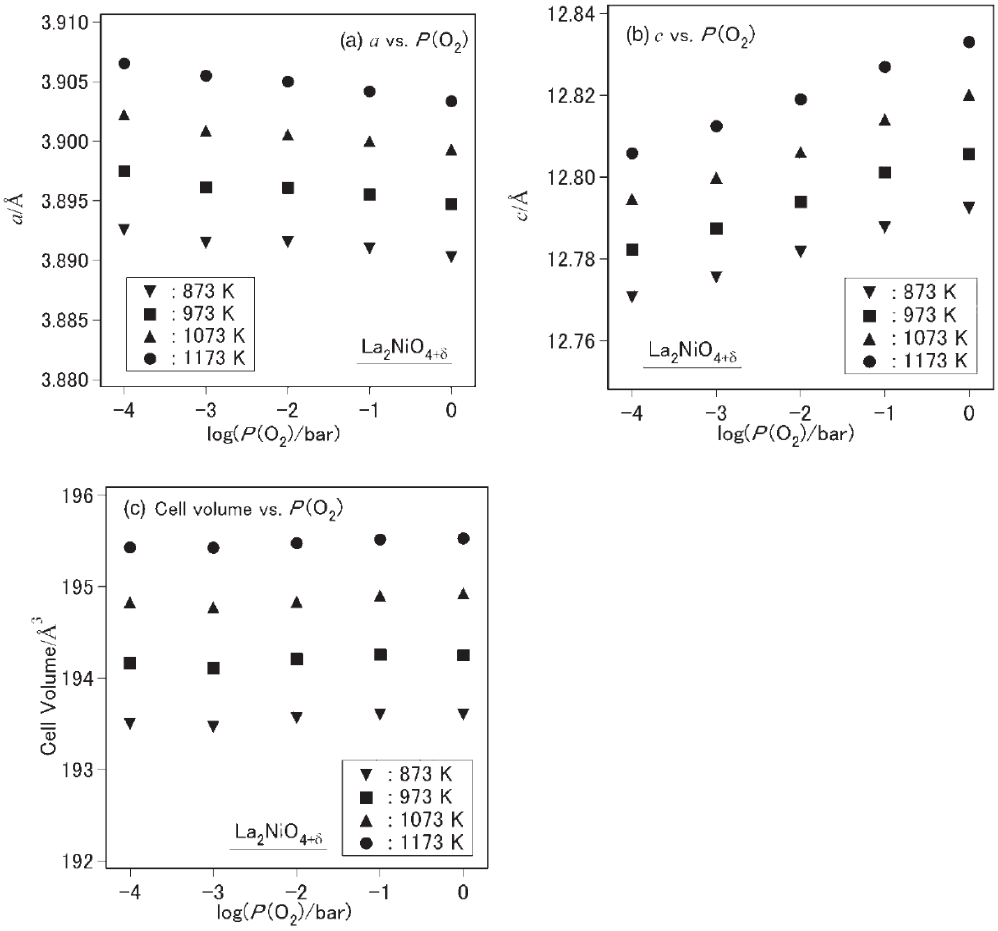

Fig. 3.9 The lattice parameters of $La_2NiO_{4+\delta}$ (LN214) as a function of $P(O_2)$; (a) a vs. $P(O_2)$, (b) c vs. $P(O_2)$, and (c) cell volume vs. $P(O_2)$, which are taken from the literature [3.11].

3.4 Conclusions

The Young's and the shear moduli and the Poisson's ratio of $La_{0.6}Sr_{0.4}Co_{0.2}Fe_{0.8}O_{3-\delta}$ (LSCF6428) and $La_2NiO_{4+\delta}$ (LN214) were evaluated as a function of $P(O_2)$. The Young's and the shear moduli of LSCF6428 showed a different $P(O_2)$ dependence in response to temperature. The $P(O_2)$ dependence was qualitatively explained by complex influences of the phase transition, the chemical expansion and the variation of the oxygen nonstoichiometry and the cation mean valence. On the other hand, the mechanical properties of the Young's and the shear moduli of LN214 were almost independent of $P(O_2)$. This is possibly because the decrease in the amount of excess oxygen atoms leads to the decrease in the elastic constant C_{33} and simultaneously the increase in the elastic constants, C_{11} and C_{22}. Therefore, the Young's the shear moduli are not macroscopically influenced by the change in the amount of excess oxygen atoms.

3.5 References

[3.1] K. Amezawa, T. Kushi, K. Sato, A. Unemoto, S. Hashimoto, and T. Kawada, *Solid State Ionics*, **198** 32 (2011).

[3.2] Y. Wang, K. Duncan, E. D. Wachsman, and F. Ebrahimi, *Solid State Ionics*, **178** 53 (2007).

[3.3] T. Hashida, K. Sato, Y. Takeyama, T. Kawada, and J. Mizusaki, *ECS Trans.*, **25** (2) 1565 (2009).

[3.4] S. W. Paulik, S. Baskaran, T. R. Armstrong, *J. Mater. Sci.*, **22**, 2397 (1998).

[3.5] S. Hashimoto, Y. Fukuda, M. Kuhn, K. Sato, K. Yashiro, J. Mizusaki, *Solid State Ionics*, **181**, 1713 (2010).

[3.6] T. Nakamura, K. Yashiro, K. Sato, J. Mizusaki, *Solid State Ionics*, **180**, 368 (2009).

[3.7] A. Mineshige, M. Kobune, S. Fujii, Z. Ogumi, M. Inaba, T. Yao and K. Kikuchi, *J. Solid State Chem*, **142**, 374 (1999).

[3.8] M. Kuhn, S. Hashimoto, K. Sato, K. Yashiro and J. Mizusaki, *Solid State Ionics*, **195**, 7 (2011).

[3.9] B. X. Huang, J. Malzbender, R. W. Steinbrech and L. Singheiser, *Solid State Ionics*, **180**, 241 (2009).

[3.10] P. E. Vullum, R. Holmestad, H. L. Lein, J. Mastin, M.–A. Einarsrud, and T. Grande, *Adv. Mater.*, **19**, 4399 (2007).

[3.11] T. Nakamura, K. Yashiro, K. Sato, J. Mizusaki, *Solid State Ionics*, **181**, 292 (2010).

Chapter 4

The text presented in this Chapter is reproduced in part with permission from:

Y. Kimura, K. Yashiro, S. Hashimoto, T. Kawada, *J. Electrochem. Soc.*, 161(11), F3079, 2014.

Y. Kimura, J. Tolchard, M.-A. Einarsrud, T. Grande, K. Amezawa, M. Fukuhara, S. Hashimoto and T. Kawada, *Solid State Ionics*, 262, 337 (2014).

Influence of ferroelastcity on the mechanical properties of perovskite and related oxides

4.1 Introduction

In chapter 2, the elastic modulus and the internal friction of $La_{0.6}Sr_{0.4}Co_{0.2}Fe_{0.8}O_{3-\delta}$ (LSCF6428), $La_{0.6}Sr_{0.4}CoO_{3-\delta}$ (LSC), $La_{0.6}Sr_{0.4}Co_{0.8}Fe_{0.2}O_{3-\delta}$ (LSCF6482), $La_{0.6}Sr_{0.4}FeO_{3-\delta}$ (LSF), and La_2NiO_4 (LN214) were evaluated at high temperatures under controlled atmospheres by using the resonance method [4.1]. It was found that the elastic modulus of LN214 measured by the resonance gradually decreased with increasing temperature, which is a typical temperature dependence of conventional ceramics such as alumina [4.2]. On the other hand, the elastic modulus of LSCF measured by the resonance method decreased by 35-50% of the value at room temperature with increasing temperature in the temperature range in which the crystal structure of LSCF was rhombohedral [4.1]. Moreover, the internal friction of LSCF showed one or two broad peak/peaks in the same temperature range. The magnitude of the significant decrease observed in a rhombohedral phase could not be explained only by the thermal expansion, and it was suggested that there were other mechanisms which caused the significant decrease in the elastic modulus measured by the resonance method. A possible cause which can lead to the significant decrease in the elastic modulus measured by the resonance method, and a peak in the internal friction of LSCF, is the ferroelastic domain reorientations. The rhombohedral crystal structure of perovskite oxides is formed by the compression of the ideal cubic structure along the <111> directions of a cubic unit cell. Therefore, the rhombohedral perovskite can have four kinds of the ferroelastic domains which have a rhombohedral distortion along with one of [111], $[11\bar{1}]$, $[1\bar{1}1]$, and $[\bar{1}11]$ directions [4.3, 4.4]. If the material is cooled through the phase transition temperature, these four kinds of the ferroelastic domains are formed in the material. When stress which is large enough to unpin the ferroelastic domains is applied to the material, the ferroelastic domain walls will move. This motion of the ferroelastic domain walls relaxes the applied stress, and thus can be the cause of the apparent enormous decrease in the elastic modulus and the increase in the internal friction, which was observed in our previous experiments. The motion of the ferroelastic domain walls in $LaCoO_3$-based perovskite oxides with rhombohedral symmetry has been confirmed by TEM and SEM observation [4.4, 4.5].

If this motion of the ferroelastic domain walls occurs in LSCF, the stress-strain relationship of LSCF should be nonlinear. And thus the Young's modulus measured by the resonance method should depend on the amplitude of the oscillation. Furthermore, the motion of the ferroelastic domains is considered to be a thermally activated process. Therefore, the temperature dependence of the elastic modulus and the internal friction of LSCF should depend also on measuring frequency.

Furthermore, the mobility of the ferroelastic domain walls is considered to be controlled by various mechanisms, *e.g.* the interaction between domain walls and defects such as grain boundaries, dislocations, surfaces, and cation and anion vacancies [4.6-4.9]. Especially, it is reported that the oxygen vacancies play a dominant role in determining the mobility of the ferroelastic domain walls in perovskite oxides [4.8, 4.10]. LSCF shows relatively high oxygen nonstoichiometry at high temperatures while it has a very small oxygen vacancy concentration under equilibrium conditions at low temperatures [4.11]. However, the oxygen vacancies can remain in LSCF even at low temperatures if LSCF is cooled from high temperatures so fast that LSCF cannot be equilibrated with ambient conditions. Thus the mechanical properties of rhombohedral LSCF can be strongly influenced by the presence of the oxygen vacancies due to the interaction between the ferroelastic domain walls and the oxygen vacancies.

In this chapter, the stress-strain relationship of LSCF was investigated by uniaxial compression tests. And the amplitude and frequency dependence of the elastic modulus and the internal friction of perovskite and related oxides were evaluated by the resonance method and dynamic mechanical analysis (DMA) in order to understand the influence of ferroelasticity on the mechanical properties. In addition, DMA was also performed with LSCF6428 with various oxygen vacancy concentrations, in order to understand the influence of the interaction between the ferroelastic domain walls and the oxygen vacancies on the mechanical properties.

4.2 Experimental

4.2.1 Uniaxial compression tests

The uniaxial compression tests were performed in order to evaluate the stress-strain curve of LSCF6428, LSC, and LSF in the temperature range between room temperature and 1073 K in air. Powders of LSCF6428 were purchased from AGC SEIMI CHEMICAL Co., Ltd. while powders of LSC and LSF were synthesized by the Pechini method. The detailed procedure for the sample preparation is given in chapter 2. The powders of LSCF6428, LSC, and LSF were first compacted into cylinders by uniaxial pressing at about 10 MPa and then isostatically pressed at 150 MPa. The compacts were sintered in air for 6 hours at 1473 K (LSC), 1573 K (LSCF6428 and LSF) and slowly cooled with the rate of 106 K/h to avoid cracking. The sintered compacts of LSCF were machined into cylindrical samples of diameter 5.0-5.1 mm and height 9.5-10 mm. The surfaces of the samples were polished to a 1 μm finish. The deviation in parallelism of the surfaces was less than 10μm. Relative densities of the samples were over 95 %. Details of the set-up are given elsewhere [4.12]. A stress up to 300 MPa was applied by a 20 kN uniaxial actuator (Cormet digital control, Cormet, Finland) and measured by 20 kN load cells (Cormet, Finland). The stress rate was ~25 MPa/min. The deformation of a sample was measured by an extensometer (MTS 634.31F-25 S/N 1144123, MTS Sensors, USA). The sample was held for 1 hour to attain equilibrium before each measurement. Once a measurement was performed, the load was removed from the sample and the sample was annealed at 1173 K for 1 hour, in order to “reset” the ferroelastic domain switching. Then it was cooled and the next measurement was successively performed with the same sample.

4.2.2 Resonance measurements

The dynamic amplitude dependence of Young’s modulus, E, and internal friction, Q^{-1}, of LSCF6428 and LN214 was evaluated by the resonance method with an elastic modulus meter (EGII-HT, Nihon Technoplus Co., Ltd., Japan). One end of a rectangular-shaped sample is rigidly fixed and a flexural oscillation is applied to another end of the sample by an electromagnetic actuator. The force applied to the sample was controlled by changing output voltage of the electromagnetic actuator. The resonance frequency of the sample was detected by an eddy current sensor. The eddy current sensor was calibrated by using a spectral-interference laser displacement meter (SI-F10, Keyence Corporation, Japan) to obtain the absolute value of the dynamic amplitude of the resonance oscillation. The $P(O_2)$ around the sample was controlled to be 1 x 10^{-1} bar by flowing a mixture gas of O_2 and Ar, and monitored by an yttria-stabilized zirconia oxygen sensor. The measurements were repeated until the measured values of the Young's modulus and the internal friction became constant at each temperature, *i.e.*, until the sample equilibrated with the surrounding atmosphere.

4.2.3 Dynamic mechanical analysis

The temperature dependence of the dynamic Young's modulus and of the internal friction of LSCF6428, LN214, and $La_{0.9}Sr_{0.1}Ga_{0.8}Mn_{0.2}O_3$ (LSGM) at low frequencies were measured by using the technique of DMA operating in three-point bend geometry (DMS6100, Hitachi High-Tech Science Co., Japan). The powders of LSCF6428 and of LSGM were obtained from AGC SEIMI CHEMICAL Co., Ltd., Japan and KUSAKA RARE METAL, Japan, respectively. The powders of LN214 were synthesized by the Pechini method. The powders were hydrostatically pressed at 150 MPa and sintered at 1573 K for 6 hours (LSCF6428) and at 1673 K for 10 h (LN214 and LSGM) in air. The sintered samples were cut into a rectangular shape and the surfaces were mirror polished. Then, the samples were annealed at 1173 K for 6 hours in air in order to get rid of the influence of the machining. The relative densities of the samples were over 95 %.

A sinusoidal force with the frequency in the range from 0.01 to 50 Hz was applied at the center of the sample. The amplitude of the applied force was determined so that the amplitude of the deflection of the sample would be 10 μm. The dynamic Young's modulus, M^*, and the internal friction, Q^{-1}, were calculated from the amplitude of the applied force, F, and of the deflection, u, and the phase difference between the applied force and the deflection, φ, as follows:

$$M^* = \frac{l^3}{4t^3 w}\frac{F}{u}\exp(i\varphi) \qquad [4.1]$$

$$Q^{-1} = \tan(\varphi) \qquad [4.2]$$

where, l, w, t are the length, the width, and the thickness of the sample, which were approximately 45, 1.3, and 0.7 mm, respectively. The real and imaginary components of the dynamic Young’s modulus are referred to as the storage (M') and the loss (M'') moduli, respectively. The storage and the loss moduli, and the internal friction have the following relationship:

$$Q^{-1} = \frac{M''}{M'} \qquad [4.3]$$

Therefore, given two of the above three parameters, another parameter can be calculated according to the eq. [4.3]. The measurements were performed at 100% N_2, increasing the temperature from 243 to 773 K with the heating rate of 1.5 K/min and changing the frequency of the applied force from 0.01 to 50 Hz.

4.2.4 Heat treatment for LSCF6428

In order to create different oxygen vacancy concentrations, the samples of LSCF6428 were further heat treated in a glass tube in the following three different conditions: (1) a sample was heat treated at 873 K under $P(O_2)$ of 1 bar for 50 hours and cooled to room temperature with the cooling rate of 1.3 K/min; (2) a sample was heat treated at 973 K under $P(O_2)$ of 10^{-2} bar for 35 hours and quenched to room temperature; and (3) a sample was heat treated at 973 K under $P(O_2)$ of 10^{-4} bar for 35 hours and quenched to room temperature. The quenching rate in the conditions (2) and (3) was approximately 140 K/min down to 423 K and 18 K/min for the range from 423 K to room temperature. The $P(O_2)$ in the glass tube was controlled by flowing a mixture gas of O_2 and Ar, and monitored by two zirconia oxygen sensors which were equipped at upper stream and downstream of the glass tube. In this paper, the samples heat treated in the conditions (1), (2), and (3) are referred to as LSCF1, LSCF2, and LSCF3, respectively. The oxygen vacancy concentration is small at 873 K under $P(O_2)$ of 1 bar ($\delta \approx 0.005$), while it is comparatively large at 973 K under $P(O_2)$ of 10^{-2} bar ($\delta \approx 0.032$) and 10^{-4} bar ($\delta \approx 0.074$) [4.11]. Therefore, the LSCF1, LSCF2, and LSCF3 were thought to have the higher oxygen vacancy concentrations in the order of LSCF3, LSCF2, and LSCF1. The samples were analyzed by X-ray diffractometer (D8 DISCOVER, Bruker AXS, Germany, CuKα, 40 kV, 40 mA) in 2θ range of 20–100°, after the heat treatments. The crystal structure and the lattice parameters of the samples were analyzed by whole powder pattern decomposition (WPPD) method with software (DIFFRAC. TOPAS ver.4.2.0.2, Bruker AXS, Germany). It was confirmed that the crystal structure of all three samples were rhombohedral perovskite (space group: $R\bar{3}c$).

There is a possibility that the oxygen vacancy concentration in the samples changes at high temperatures during the experiment. In order to estimate the temperature range where the oxygen vacancy concentration in the samples remains unchanged, we roughly calculated the diffusion time of the oxygen diffusion at each temperature in the temperature range from 243 to 773 K using the chemical diffusion coefficient [4.13]. The diffusion time, t_{Diff}, can be given by;

$$t_{\mathrm{Diff}} = \frac{t^2}{4D_{\mathrm{chem}}} \qquad [4.4]$$

Where t is the thickness of the sample and D_{chem} is the chemical diffusion coefficient. The value of D_{chem} was extrapolated from the data taken from the Ref. [4.13]. The diffusion time at room temperature was approximately 3.5 x 10^{12} hours while it was 1900, 60, and 5 hours at 573, 673, and 773 K, respectively. Thus the estimated diffusion time is an order of magnitude greater than the total measuring time (5 hours) below 673 K. The above estimation was based on the premise that the rate-determining step was the diffusion in the sample. If the surface reaction is the rate-determining step, the actual diffusion time is considered to be longer than the diffusion time estimated above. Therefore, it is believed that the oxygen vacancy concentration does not change below 673 K.

4.3 Results and discussion

4.3.1 Uniaxial compression tests

Stress-strain relationship at various temperatures

Figure 4.1 (a) shows the stress-strain relationship of LSCF6428 under loading and unloading at room temperature in air. Under loading, the stress-strain relationship was almost linear at lower stress but a clearly nonlinear behavior was observed above 70 MPa. The slope of the stress-strain curve became gradually steeper with increasing the applied stress above 70 MPa. Then it gradually became milder again above 150 MPa. The stress-strain relationship was almost linear again above 200 MPa. The stress-strain relationship under unloading was almost linear. A residual strain was observed after unloading. The effective compliance, *S*, of LSCF6428, which is the first derivative of the strain with respect to the stress under loading, had a peak at about 150 MPa. Such a nonlinear stress-strain relationship with a residual strain and a peak in the effective compliance is also previously observed for $LaCoO_3$ and $La_{1-x}Ca_xCoO_3$ [4. 12].

At 473, 673, and 873 K (Figs. 4.1 (b)-(d)), the stress-strain relationship was nonlinear even starting from low stress levels. A residual strain was also observed at these temperatures. It became smaller with increasing temperature. Under unloading, the stress-strain relationship was almost linear at higher stress but it became nonlinear at lower stress. A peak was observed in the effective compliance at 473 K. However, the stress level at which the peak was observed was much lower than that at room temperature. At 673 and 873 K, the peak in the effective compliance was not clearly observed. Instead, the effective compliance showed a comparatively large value in the neighborhood of zero stress. At 1073 K (Fig. 4.1 (e)), the stress-strain relationship under loading was almost linear up to about 250 MPa. The slope of the stress-strain curve became slightly steeper above 250 MPa. Contrary to the results below 873 K, the stress-strain relationship under unloading was nonlinear when higher stress was applied but it was almost linear at lower stress. A residual strain was also observed at this temperature. The effective compliance showed a slightly larger value at the beginning of loading and at around the maximum stress but it was almost constant over the wide range of the applied stress.

The nonlinear stress-strain relationship with a residual strain, which was observed below 873 K, can be interpreted by considering the ferroelasticity. The phase transition temperature of LSCF6428 is reported to be 973-1073 K [4.14]. Below the phase transition temperature, LSCF6428 has rhombohedral symmetry [4.14]. If LSCF6428 is cooled through the phase transition temperature, randomly oriented ferroelastic domains are formed in the material. LSCF6428 with rhombohedral symmetry deforms elastically if the applied stress is very small. However, when sufficiently large stress is applied to LSCF6428 with rhombohedral symmetry, the ferroelastic domains with a proper orientation reorient to relax the stress. Considering the above, the stress-strain relationship of LSCF6428 with rhombohedral symmetry is expected to be as follows. When the applied stress is low, LSCF6428 deforms elastically and thus the stress-strain relationship is linear. When the applied stress surpasses a certain stress level, the ferroelastic domains start to reorient and relax the applied stress. This makes the stress-strain relationship nonlinear and the slope of the stress-strain curve steeper. At a certain stress level, the ferroelastic domain switching is completed and only the elastic deformation is observed. Thus the slope of the stress-strain curve becomes milder and the stress-strain relationship becomes linear again. This change in the slope of the stress-strain curve is reflected on a peak in the effective compliance. During unloading, only the elastic deformation can occur and the strain due to the ferroelastic domain switching is preserved. Therefore, a residual strain is observed after unloading. The above discussion well describes the stress-strain relationship observed at room temperature.

Since the phase transition of LSCF6428 is a second-order phase transition, the crystal structure of LSCF6428 gradually changes from rhombohedral to cubic with increasing temperature [4.14]. As the crystal structure approaches from rhombohedral to cubic, the rhombohedral distortion becomes smaller. Thus the strain which is introduced by the domain switching is considered to be smaller with increasing temperature. This can explain why the residual strain became smaller with increasing temperature. At 673 and 873 K, no peak was observed in the effective compliance. Instead the compliance showed a large value at very low stress. This suggests that the ferroelastic domain switching can occur even from the beginning of the stress application. Under unloading, the stress-strain relationship became nonlinear at lower stress above 473 K. This nonlinearity at lower stress is possibly associated with back switching of the ferroelastic domains, which is driven by residual stress in the sample [4.5]. At these temperatures, the domain switching can occur even at low stress. Thus it is possible that the back switching can be initiated by small stress such as the residual stress.

Above 1073 K in air, LSCF6428 has cubic symmetry [4.14] and the material is no longer ferroelastic. Therefore, LSCF6428 can deform only elastically above 1073 K. Thus, the stress-strain relationship should be linear with no residual strain and the effective compliance should be constant through the loading above 1073 K. However, in our measurement, the slope of the stress-strain curve became slightly steeper above 250 MPa at 1073 K. Lein *et al.* reported a creep deformation of LSCF at 1073 K and under the load less than 300MPa [4.15]. It is possible that the nonlinear stress-strain relationship at higher stress at 1073 K is due to the creep deformation. This is consistent with the fact that the stress-strain relationship at 1073 K was nonlinear at higher stress, at which the creep deformation is more likely to occur, while below 873 K, the nonlinear behavior was observed at lower stress.

The similar irreversible stress-strain relationship and a residual strain were also observed in the stress-strain curves of LSC and LSF below 673 K (Figs. 4.2 (a)-(c)) and 873 K (Figs. 4.3 (a)-(c)), respectively. On the other hand, such an irreversible stress-strain relationship was not observed above these temperatures (Figs. 4.2 (d)-(e) and Figs. 4.3 (d)-(f)). Above 1073 K, the nonlinear stress-strain relationship, which is possibly due to the creep deformation, was also observed for both LSC and LSF. The phase transition temperatures of LSC and LSF are reported to be 753 K [4.16] and 1073 K [4.17], respectively. Thus the irreversible stress-strain relationship was observed only below the phase transition temperatures for both LSC and LSF. This fact supports that the irreversible stress-strain relationship and a residual strain is related with the ferroelastic domain switching.

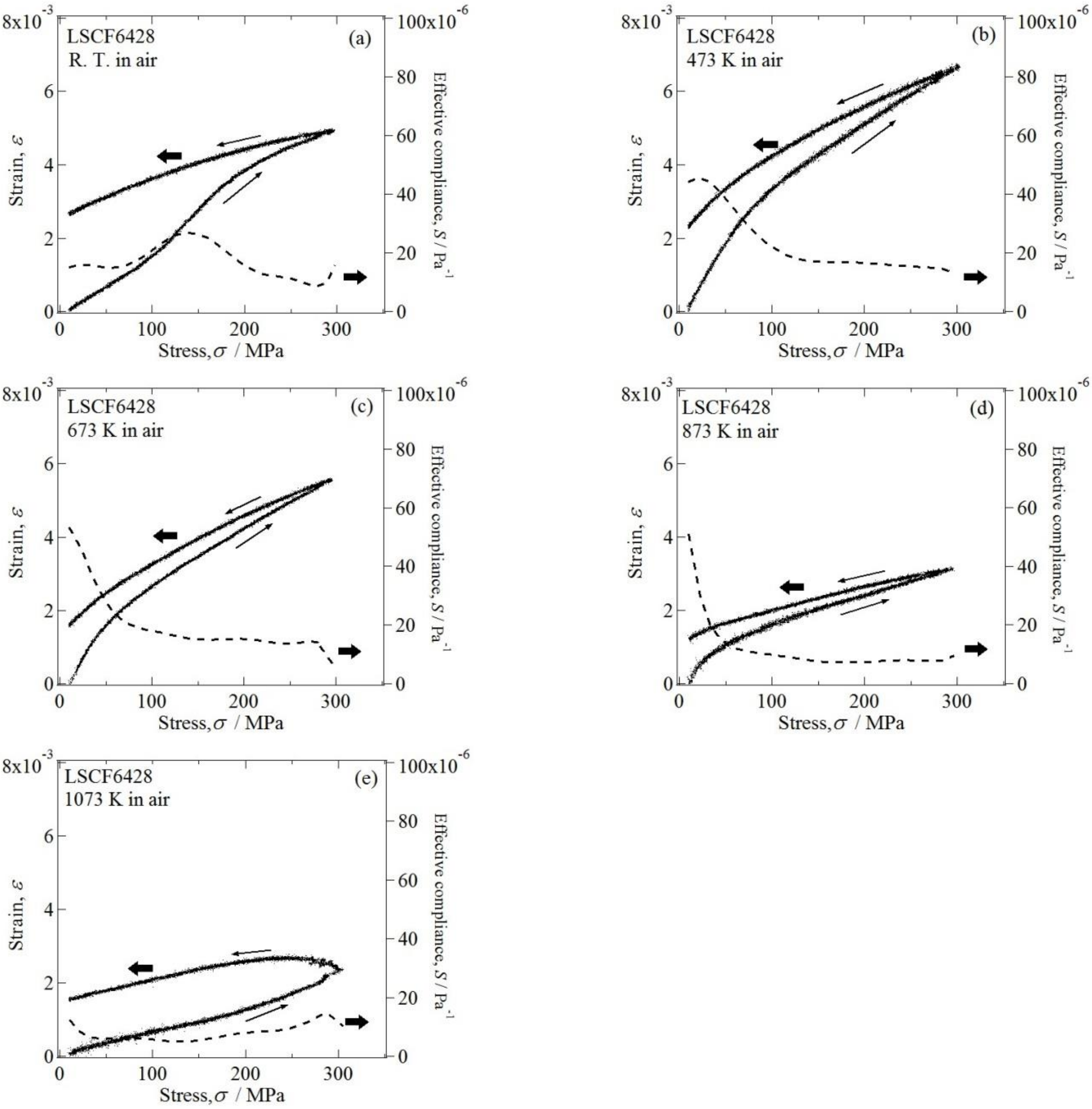

Figure 4.1. Stress-strain relationship and the effective compliance of $La_{0.6}Sr_{0.4}Co_{0.2}Fe_{0.8}O_{3-\delta}$ (LSCF6428) under loading at various temperatures in air. (a) room temperature, (b) 473 K, (c) 673 K, (d) 873 K and (e) 1073 K. The dashed line indicates the effective compliance.

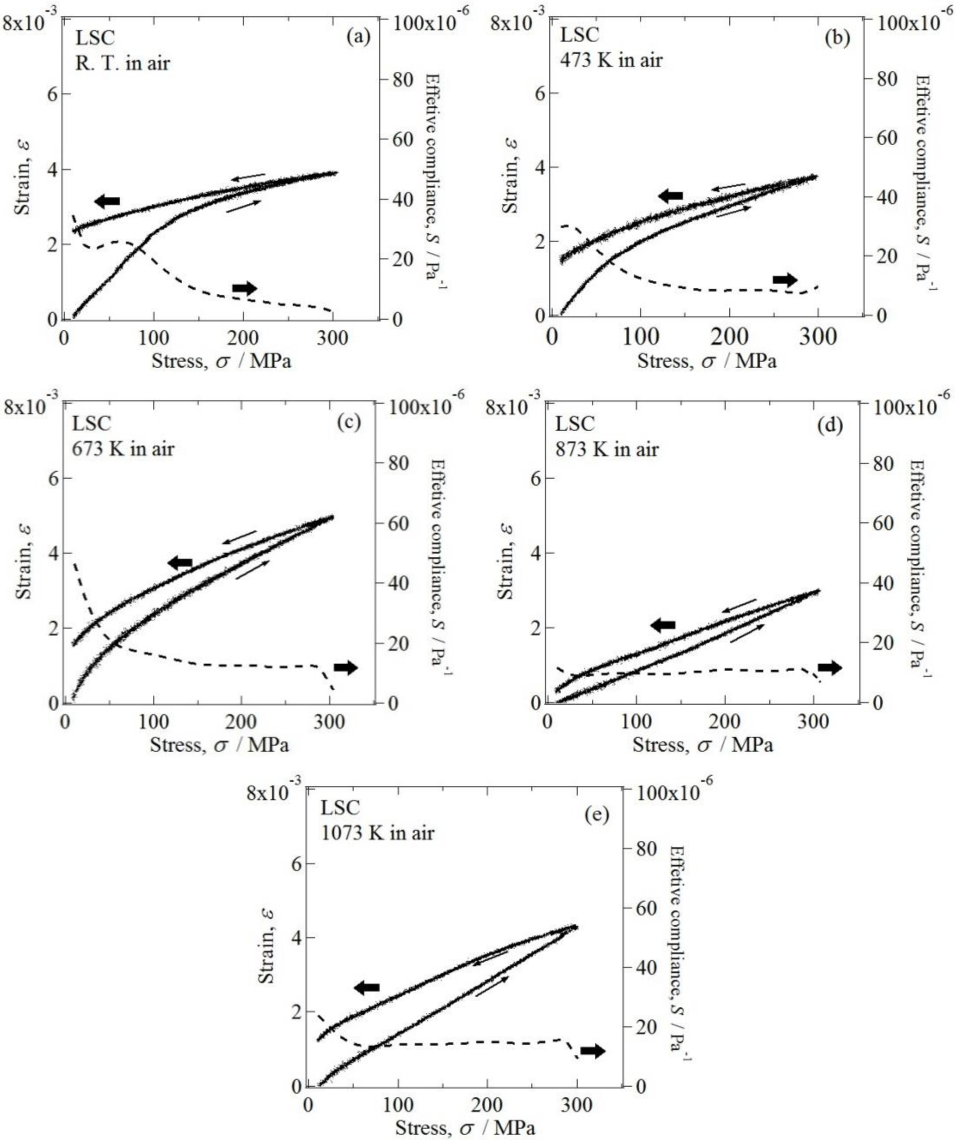

Figure 4.2. Stress-strain relationship and the effective compliance of $La_{0.6}Sr_{0.4}CoO_{3-\delta}$ (LSC) under loading at various temperatures in air. (a) room temperature, (b) 473 K, (c) 673 K, (d) 873 K and (e) 1073 K. The dashed line indicates the effective compliance.

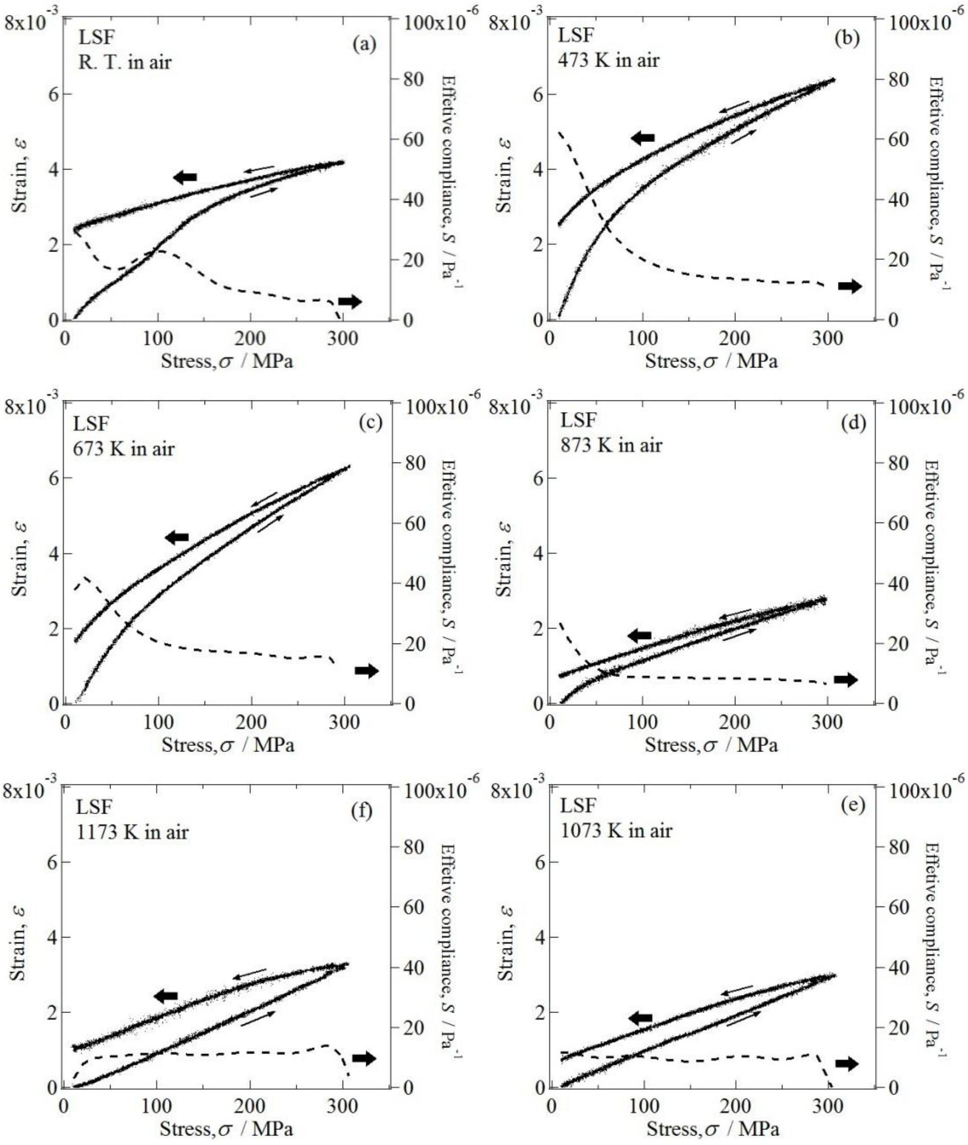

Figure 4.3. Stress-strain relationship and the effective compliance of $La_{0.6}Sr_{0.4}FeO_{3-\delta}$ (LSF) under loading at various temperatures in air. (a) room temperature, (b) 473 K, (c) 673 K, (d) 873 K, (e) 1073 K and (f) 1173 K. The dashed line indicates the effective compliance.

Cyclic tests of LSC

Figures. 4.4 (a)-(c) show the stress-strain relationship of LSC in loading-unloading cycles at room temperature, 873 K, and 1073 K, respectively. In these tests, the first and second loading-unloading cycles were subsequently performed without annealing the sample. At room temperature, the irreversible stress-strain relationship and a residual strain were observed in the first cycle. On the other hand, the stress-strain relationship was almost linear under both loading and unloading in the second cycle. No further residual strain was created after the second cycle. At 873 K, the stress-strain curve in the second cycle was almost the same as the one in the first cycle. The stress-strain relationship was linear in both the first and the second cycles and the residual strain was not observed after the unloading. At 1073 K, the width of the hysteresis in the second cycle was smaller compared with that of the first cycle. The maximum strain in the second cycle was slightly larger than that in the first cycle. The residual strain was also slightly increased after the second cycle.

The result of the cyclic test at room temperature can be explained by considering the ferroelastic domain switching. As mentioned in the previous section, it is considered that the ferroelastic domain switching was completed during the first loading and only the elastic deformation can occur after the first loading. Thus in the second cycle, the sample is considered to deform only elastically and thus the stress-strain curve was linear and no further residual strain was created. On the other hand, LSC has cubic symmetry at 873 K. Thus LSC deforms elastically and the stress-strain curve was linear with no residual strain. At 1073 K, The maximum strain in the second cycle was slightly larger than that in the first cycle. The residual strain was also slightly increased after the second cycle. This is possibly because LSC experienced a creep deformation at this temperature.

From the uniaxial compression tests and the cyclic tests, it was found that LSCF with rhombohedral symmetry shows the nonlinear stress-strain relationship, which can be well explained by the ferroelastic domain switching. This suggests that the apparent Young’s modulus of LSCF with rhombohedral symmetry depends on the applied stress. Above 473 K, the stress-strain relationship was nonlinear even starting from low stress levels. Therefore, the apparent Young’s modulus may be sensitive to the applied stress even the applied stress is very small above 473 K.

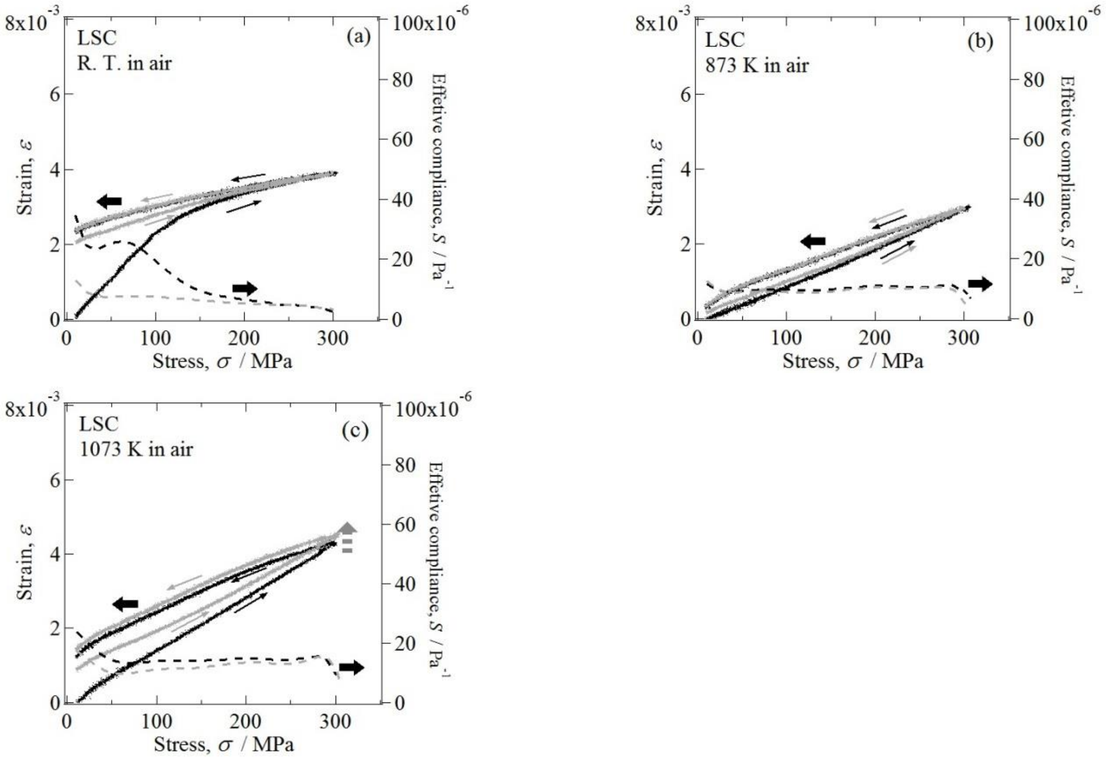

Figure. 4.4 Stress-strain relationship of LSC in the cyclic tests at (a) room temperature, (b) 873 K and (c) 1073 K. 1st and 2nd cycles of loading and unloading were subsequently repeated without annealing the sample.

4.3.2 Resonance method

Figure 4.5 (a) shows the Young's modulus of LSCF6428 as a function of the dynamic amplitude at each temperature measured by the resonance method. At room temperature and 1073 K, the Young's modulus of LSCF6428 was independent of the dynamic amplitude, while it gradually decreased with increasing the dynamic amplitude in the temperature range from 473 to 873 K. Figure 4.5 (b) shows the dynamic amplitude dependence of the internal friction of LSCF6428. The internal friction was constant at room temperature and 1073 K but it increased with increasing the dynamic amplitude between 473 and 873 K. Figures. 4.6 (a) and (b) show the Young's modulus and the internal friction of LN214 as a function of the dynamic amplitude at room temperature, 873 K, and 1073 K. Contrary to the case of LSCF6428, the Young's modulus and the internal friction of LN214 were independent of the dynamic amplitude at each temperature.

If the material is ideally elastic, the stress-strain relationship is linear and thus the Young's modulus measured by the resonance method should be independent of the dynamic amplitude. Furthermore, there is no energy loss in the material, thus the internal friction should be zero. This is considered to be the case of LN214. LN214 can be regarded to be almost ideally elastic in this measuring condition.

On the other hand, the stress-strain relationship of LSCF6428 with rhombohedral symmetry is nonlinear due to the ferroelastic domain switching. As shown in the previous section, at room temperature, LSCF6428 with rhombohedral symmetry deforms elastically if the applied stress is less than 70 MPa. However, the stress-strain relationship becomes nonlinear if the applied stress is above 70 MPa. Above 473 K, the stress-strain relationship of LSCF6428 with rhombohedral symmetry is nonlinear even the applied stress is very small.

Taking the above into account, the dynamic amplitude dependence of the Young's modulus and the internal friction of LSCF6428 can be explained as follows. At room temperature, the Young's modulus was independent of the dynamic amplitude. This is possibly because the applied stress was small and thus LSCF6428 deformed elastically. Therefore, the Young's modulus was independent of the dynamic amplitude and the internal friction was small. Above 473 K, the ferroelastic domain switching can occur even the applied stress is very small and the stress-strain relationship is nonlinear even starting from the lower stress level. Thus the Young's modulus depended on the dynamic amplitude. When the dynamic amplitude increases, the magnitude of the ferroelastic domain switching is considered to be more significant. Therefore, it is considered that the Young's modulus decreased and the internal friction increased with increasing the dynamic amplitude. Above 1073 K, LSCF6428 has cubic symmetry [4.14]. LSCF6428 with cubic symmetry deforms elastically. Thus the Young's modulus was independent of the dynamic amplitude and the internal friction is very small.

As described above, the dynamic amplitude dependence of the Young's modulus and the internal friction can be explained by considering the ferroelastic behavior of LSCF6428. Therefore, it is considered that the Young's modulus of LSCF6428 with rhombohedral symmetry measured by the resonance method can be affected by the ferroelastic domain switching.

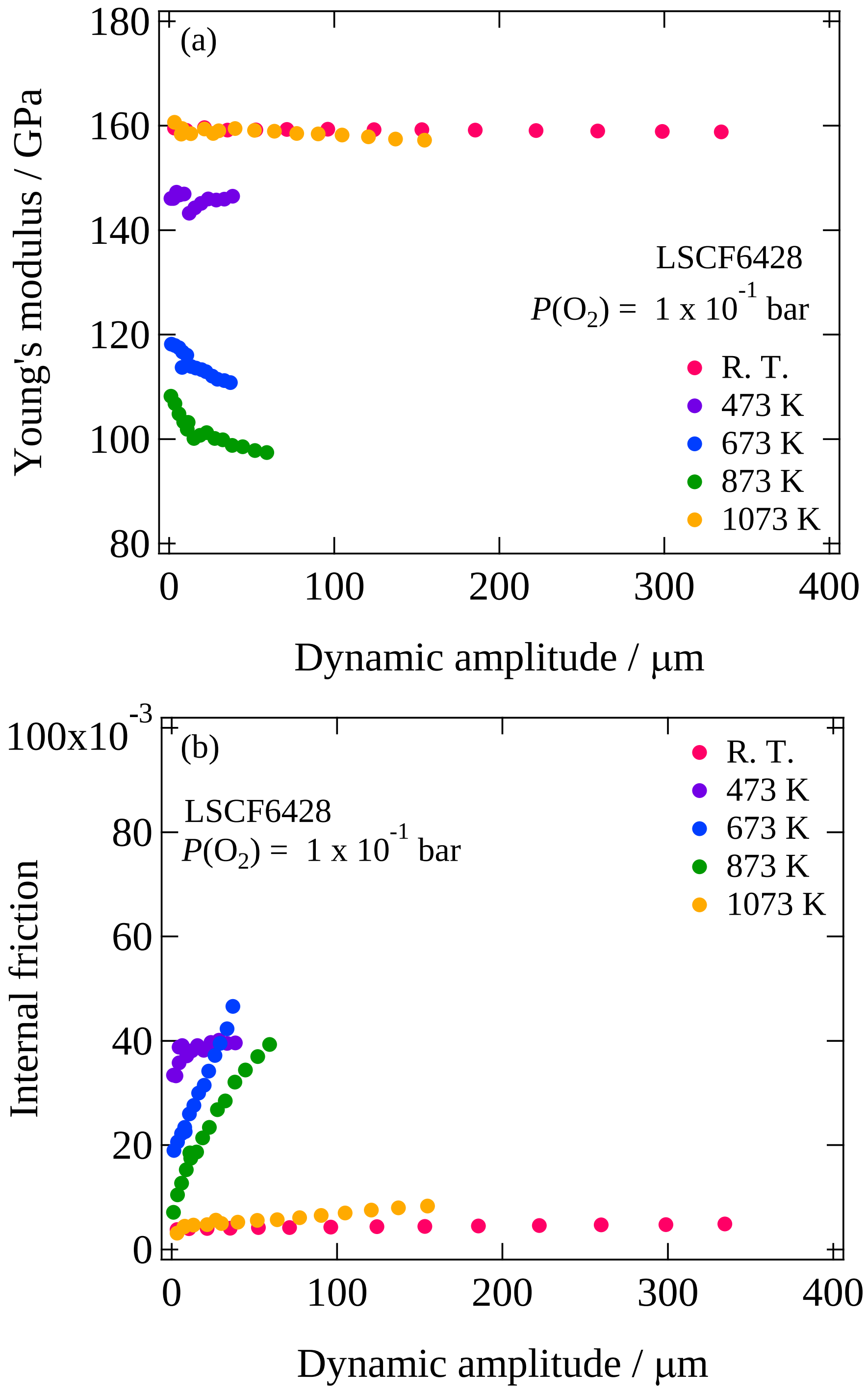

Figure 4.5. Dynamic amplitude dependence of (a) the Young's modulus and (b) the internal friction of $La_{0.6}Sr_{0.4}Co_{0.2}Fe_{0.8}O_{3-\delta}$ (LSCF6428) in the temperature range between room temperature and 1073 K under $P(O_2)$ of 1.0 x 10^{-1} bar measured by using the resonance method.

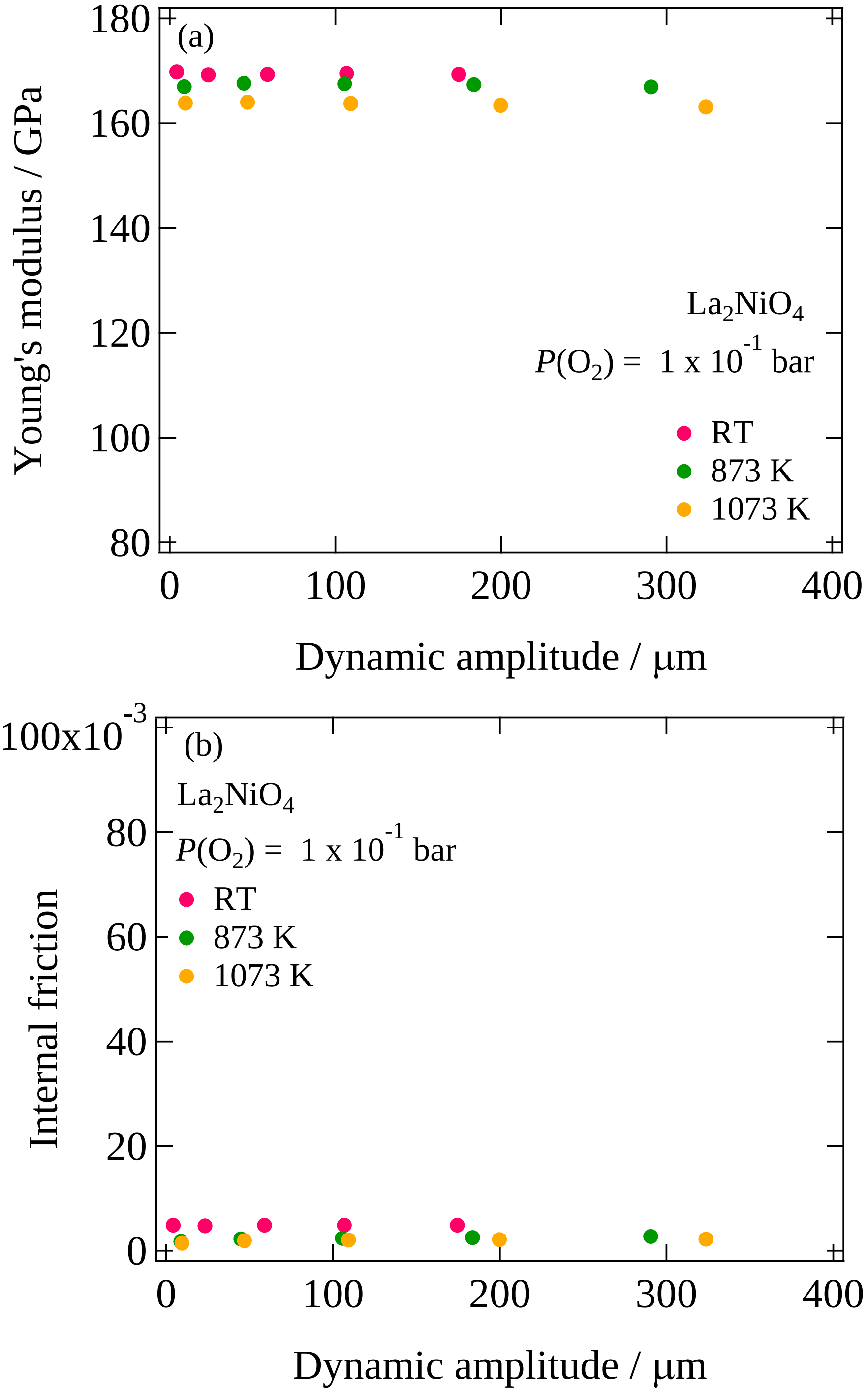

Figure 4.6. Dynamic amplitude dependence of (a) the Young's modulus and (b) the internal friction of La_2NiO_4 (LN214) in the temperature range between room temperature and 1073 K under $P(O_2)$ of 1.0 x 10^{-1} bar measured by using the resonance method.

4.3.3 Dynamic mechanical analysis

Dynamic mechanical analysis for perovskite and related oxides

Figure 4.7 shows the temperature dependence of the storage modulus and of the internal friction of the LN214. As well as the results by the resonance method, the storage modulus of LN214 monotonically decreased with increasing temperature. Although the internal friction slightly increased at around 500 K, it was very small over the whole temperature range.

Figure 4.8 shows the temperature dependence of the storage modulus and of the internal friction of the LSCF1. LSCF1 is considered to have the smallest oxygen vacancy concentration and thus to be the least influenced by the oxygen vacancies in the prepared three LSCF samples. The storage modulus first decreased slightly and then increased gradually with increasing temperature. It decreased drastically above 400 K, as is seen in the resonance measurement. The temperature at which the drastic decrease was observed shifted higher with increasing frequency. Two peaks were observed in the internal friction. A broad and asymmetric peak was observed above 400 K (P1) and a smaller peak was observed below 400 K (P2). The onset of the peak P1 and the drastic decrease of the storage modulus were observed at almost the same temperature for each frequency. The peak P1 shifted to higher temperature with increasing frequency. This means the cause of the peak P1 is a thermally activated process. Similar temperature dependence of the storage modulus and of the internal friction has been observed with $LaAlO_3$ with rhombohedral symmetry [4.6, 4.7]. The storage modulus of $LaAlO_3$ also decreases significantly with increasing temperature, and the decrease is accompanied by a broad peak which depended on frequency in the internal friction. Such a decrease in the storage modulus and a peak in the internal friction can be explained by the motion of the ferroelastic domains [4.6-4.9, 4.18, 4.19]. The motion of the ferroelastic domains is often approximately described by an anelastic relaxation [4.6, 4.8, 4.18]. The storage modulus, M', and the internal friction, Q^{-1}, of a standard anelastic solid can be given by;

$$M'(\omega) = M_{\mathrm{U}} - \frac{M_{\mathrm{U}} - M_{\mathrm{R}}}{1+\omega^2\tau_\varepsilon^2} \qquad [4.5]$$

$$Q^{-1}(\omega) = \frac{\Delta}{(1+\Delta)^{1/2}}\frac{\omega\tau}{1+\omega^2\tau^2} \qquad [4.6]$$

where $\omega = 2\pi f$ is the angular frequency of the DMA experiment, M_{U} is the unrelaxed modulus, M_R (< M_U) is the relaxed modulus, $\Delta = (M_U - M_R)/M_R$, τ is the relaxation time, and $\tau_\varepsilon = (1+\Delta)^{-1/2}\tau$ [4.20]. The domain wall unpinning is considered to be a thermally activated process [4.6, 4.8, 4.18]. Thus, the relaxation time for the motion of the ferroelastic domain walls, τ, follows the Arrhenius relationship;

$$\tau = \tau_0 \exp\left(\frac{E}{RT}\right) \qquad [4.7]$$

where τ_0, E, R, and T are a constant, the activation energy, the gas constant, and the absolute temperature, respectively. When the temperature is sufficiently low, *i.e.* $\omega\tau$, $\omega\tau_\varepsilon >> 1$, the relaxation time is too large and the ferroelastic domain walls are unable to unpin themselves on the timescale of the applied stress. Thus the ferroelastic domain walls are effectively frozen. In this case, the storage modulus is equal to the unrelaxed modulus, M_U. Conversely, when the temperature is high enough, *i.e.* $\omega\tau$, $\omega\tau_\varepsilon << 1$, the relaxation time is small enough and the ferroelastic domain walls can be moved by the applied stress. As a result, the storage modulus decreases from the unrelaxed value, M_U, to the relaxed value, M_R. The maximum in the internal friction occurs when $\omega\tau = 1$. Therefore, a peak in the internal friction accompanied by the decrease in the storage modulus is observed. However, the actual motion of the ferroelastic domain walls is controlled by various mechanisms, *e.g.* the interaction between domain walls and defects such as grain boundaries, dislocations, surfaces, and cation and anion vacancies [4.6-4.9]. Therefore, it is reported that there is a distribution of the relaxation time for the motion of the ferroelastic domain walls in perovskite oxides [4.7, 4.9, 4.19]. This distribution of the relaxation time can lead to a broad and asymmetric peak instead of a sharp symmetric peak described by eq. [4.6] in the internal friction [4.7, 4.9, 4.19]. Considering this, the broad and asymmetric peak (P1) in the internal friction of LSCF6428 may reflect on the distribution of the relaxation time for the motion of the ferroelastic domain walls.

Figure 4.9 shows the temperature dependence of the storage modulus and of the internal friction of the LSGM. The storage modulus of LSGM gradually decreased with increasing temperature below 500 K but it drastically decreased above 500 K. A peak which depended on frequency was observed in the internal friction above 500 K. LSGM is known to have orthorhombic symmetry below 500 K and rhombohedral symmetry above 500 K [--]. LSGM with orthorhombic is not ferroelastic while LSGM with rhombohedral is ferroelastic [--]. As well as the case of LSCF1, the drastic decrease and the peak in the internal friction which depends on frequency were observed in the temperature range where LSGM is ferroelastic. This results also support that the cause of the drastic decrease is the ferroelastic domain switching.

Further studies will be required to identify the cause of the peak P2 and the following anomaly in the storage modulus observed in the temperature range where the ferroelastic domains are likely to be frozen. They were not observed in the resonance measurement. In fact, such a small internal friction peak accompanied by the anomaly in the storage modulus was also observed with $LaAlO_3$ at low temperatures [4.7]. Harrison *et al*. investigated the temperature dependence of the storage modulus and the internal friction of $LaAlO_3$ with various dynamic amplitudes. They found that the storage modulus of $LaAlO_3$ monotonically decreases with increasing temperature without the anomaly in the storage modulus and the small internal friction peak when the dynamic amplitude is small. However, the small peak and the following anomaly in the storage modulus appeared when the dynamic amplitude was large. Harrison *et al*. attributed the cause of the small peak to the partial domain reorientation of weakly pinned domains [4.7]. They optically confirmed the small number of the ferroelastic domains could undergo small-amplitude displacements even at low temperatures. It is possible that there are weakly pinned domains also in LSCF6428 and the motion of these domains caused the peak P2.

Oxygen vacancy concentration dependence

Figure 4.10 (a) shows the temperature dependence of the storage modulus and of the internal friction of LSCF2. The storage modulus of LSCF2 decreased monotonically with increasing temperature and depended on frequency. The slight decrease and the subsequent gradual increase which were observed in the storage modulus of LSCF1 were not observed. The storage modulus of LSCF2 was significantly larger than that of LSCF1 particularly at low temperatures. The peaks P1 and P2 were not clearly observed in the internal friction of LSCF2. On the other hand, a small shoulder peak which depended on frequency was observed between 300 and 400 K (P3) as shown in Fig. 4.10 (b). Figure 4.11 (a) shows the temperature dependence of the storage modulus and of the internal friction of LSCF3. The storage modulus of LSCF3 decreased monotonically with increasing temperature and depended on frequency as is the case in LSCF2. However, it showed higher values than that of LSCF2. The peaks P1 and P2 in the internal friction were both barely observed while the peak P3 became more noticeable and it clearly depended on frequency as shown in Fig. 4.11 (b). From this result, it is suggested that the peak P3 is related with one or more relaxation processes and the peak height of the peak P3 depends on the oxygen vacancy concentration. Cordero has found that oxygen vacancies in $SrTiO_{3-\delta}$ with $\delta < 0.01$ can give rise to at least three anelastic relaxation processes associated with hopping of isolated vacancies, reorientation of pairs, and formation/dissolution of pairs and other clusters [4.23]. LSCF2 and LSCF3 is considered to have larger oxygen nonstoichiometry than $\delta = 0.01$. Therefore, it is likely that the peak P3 was caused by the above mentioned mechanisms, which were related with the movement of the oxygen vacancies in LSCF6428.

The reason that peaks P1 and P2 became smaller and the storage modulus became larger with increasing the oxygen vacancy concentration can be possibly explained by the pinning effect of oxygen vacancies [4.6-4.9]. If this occurs in LSCF 2 and 3, the motion of the ferroelastic domain walls is suppressed. This lead to the smaller peak in the internal friction and higher storage modulus, compared to those of LSCF6428 with no oxygen vacancies. It is also reported that the ferroelastic domain walls become increasingly insensitive to point defects as the domain wall thickness increases [4.7, 4.24]. The domain wall thickness increases with increasing temperature [4.7, 4.24]. This means that the domain walls become increasingly insensitive with increasing temperature. The storage moduli of LSCF2 and 3 exhibited similar values with that of LSCF1 at high temperatures although they were significantly larger than that of LSCF1 at lower temperatures. This may be because the effect of the domain pinning by the oxygen vacancies is significant in LSCF2 and 3 at lower temperatures while it becomes less influential at higher temperatures due to the growth of the thickness of the ferroelastic domain walls. The above discussion suggests that the oxygen vacancies play a vital role in determining the mobility of the ferroelastic domains in LSCF6428 especially at low temperatures. On the other hand, above 673 K, the diffusion time of oxygen diffusion becomes almost comparable to the total measuring time. Therefore, it is possible that the difference in the oxygen vacancy concentration of LSCF1, 2, and 3 became smaller at high temperatures. This could be also the reason why the storage moduli of LSCF2 and 3 exhibited similar values with that of LSCF1 at high temperatures. Furthermore, the internal friction and the storage modulus can be influenced by the crystal structure change, which was driven by a change in the oxygen vacancy concentration. It is reported that the crystal structure of LSCF becomes closer to cubic when the oxygen vacancy concentration in LSCF is higher [4.25, 4.26]. This was also demonstrated by our XRD analysis. The rhombohedral angles of LSCF1, LSCF2, and LSCF3 were 60.32, 60.28, and 60.17 degrees, respectively. The crystal structure is closer to cubic if the rhombohedral angle is closer to 60 degree. Therefore, the crystal structure of LSCF1, LSCF2, and LSCF3 were thought to be closer to cubic in the order of LSCF3, LSCF2, and LSCF1. The extent of the macroscopic strain due to the motion of the ferroelastic domains depends on the magnitude of the rhombohedral distortion. Thus the energy dissipation and the decrease in the storage modulus, due to the motion of the ferroelastic domains, are more suppressed if the crystal structure of LSCF6428 is closer to cubic.

It can be said that the motion of the ferroelastic domain walls and the oxygen vacancies have a strong influence on the storage modulus and the internal friction of LSCF6428 with rhombohedral symmetry, especially at low temperatures.

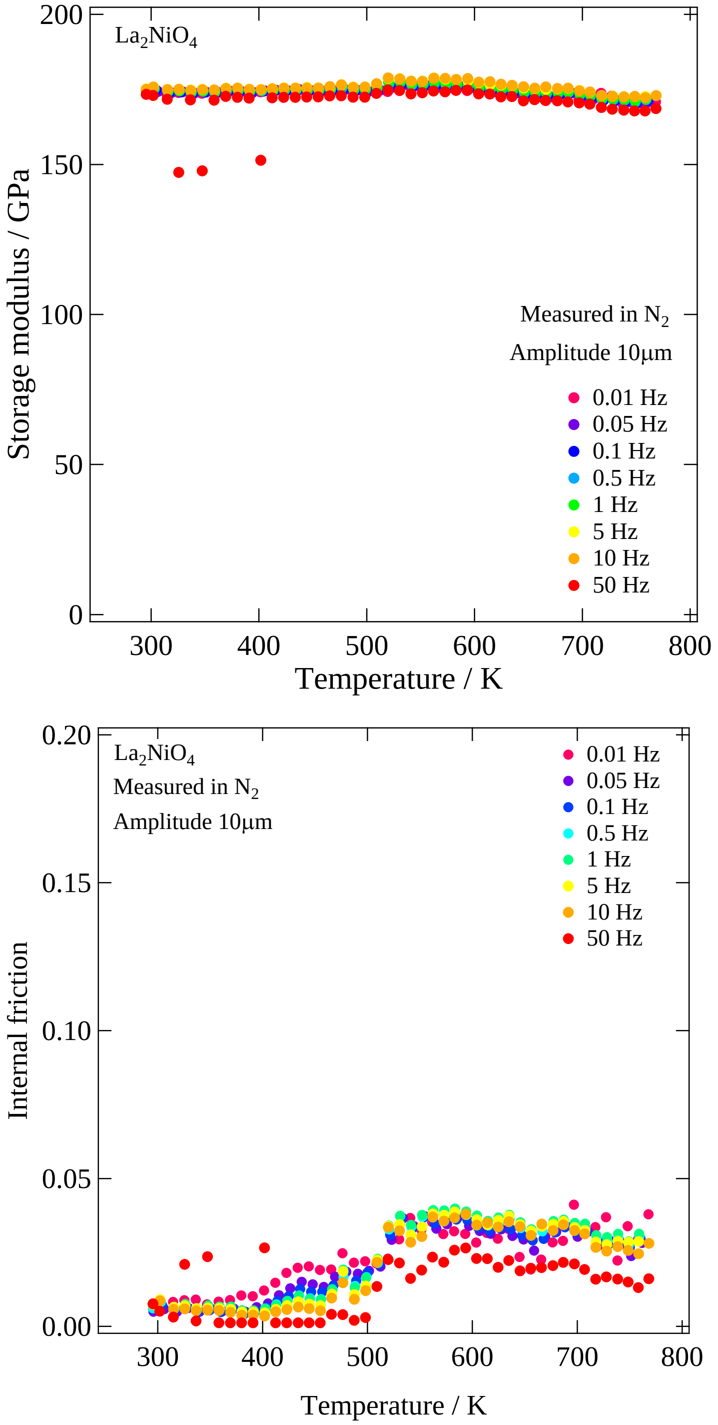

Figure 4.7. Temperature dependence of storage modulus (closed symbols) and of internal friction (open symbols) of La_2NiO_4 annealed at 873 K under the $P(O_2)$ of 1 bar (LSCF1) in the frequency range from 0.01 to 50 Hz.

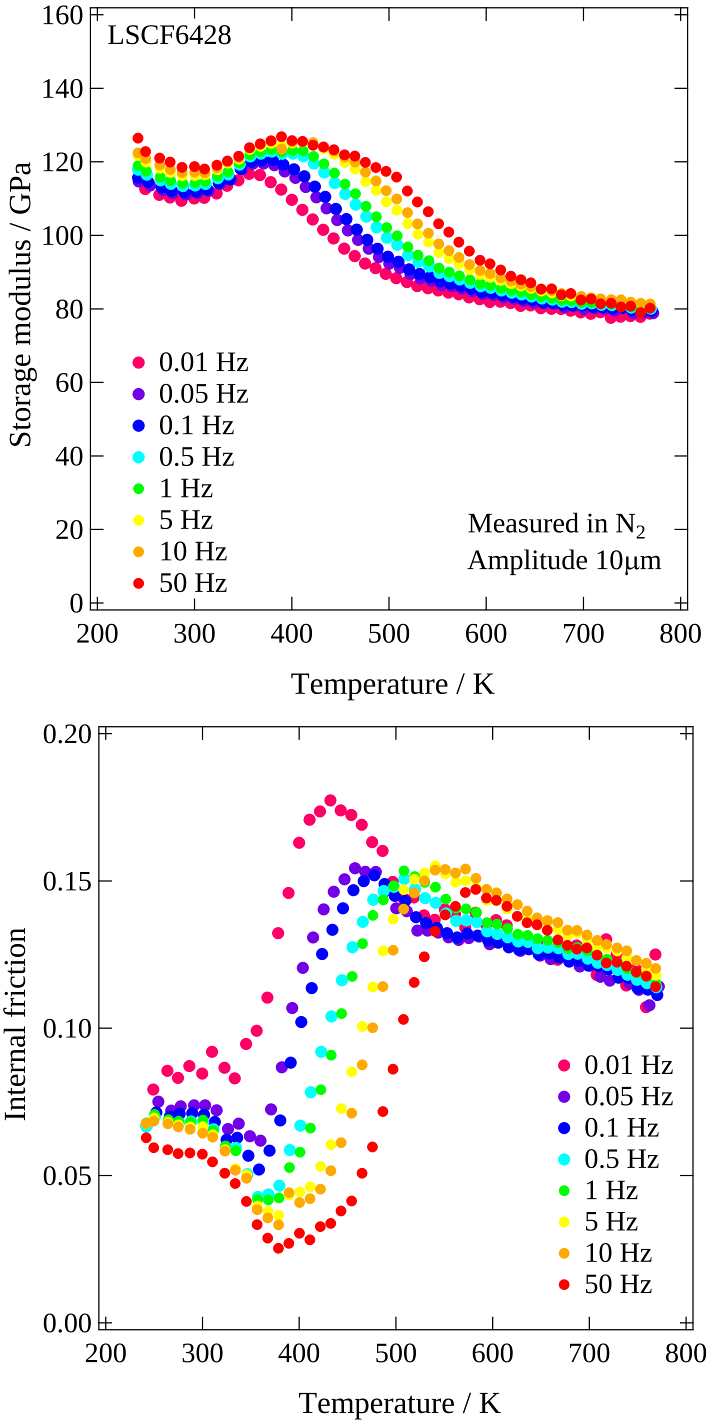

Figure 4.8. Temperature dependence of storage modulus (closed symbols) and of internal friction (open symbols) of LSCF6428 annealed at 873 K under the $P(O_2)$ of 1 bar (LSCF1) in the frequency range from 0.01 to 50 Hz.

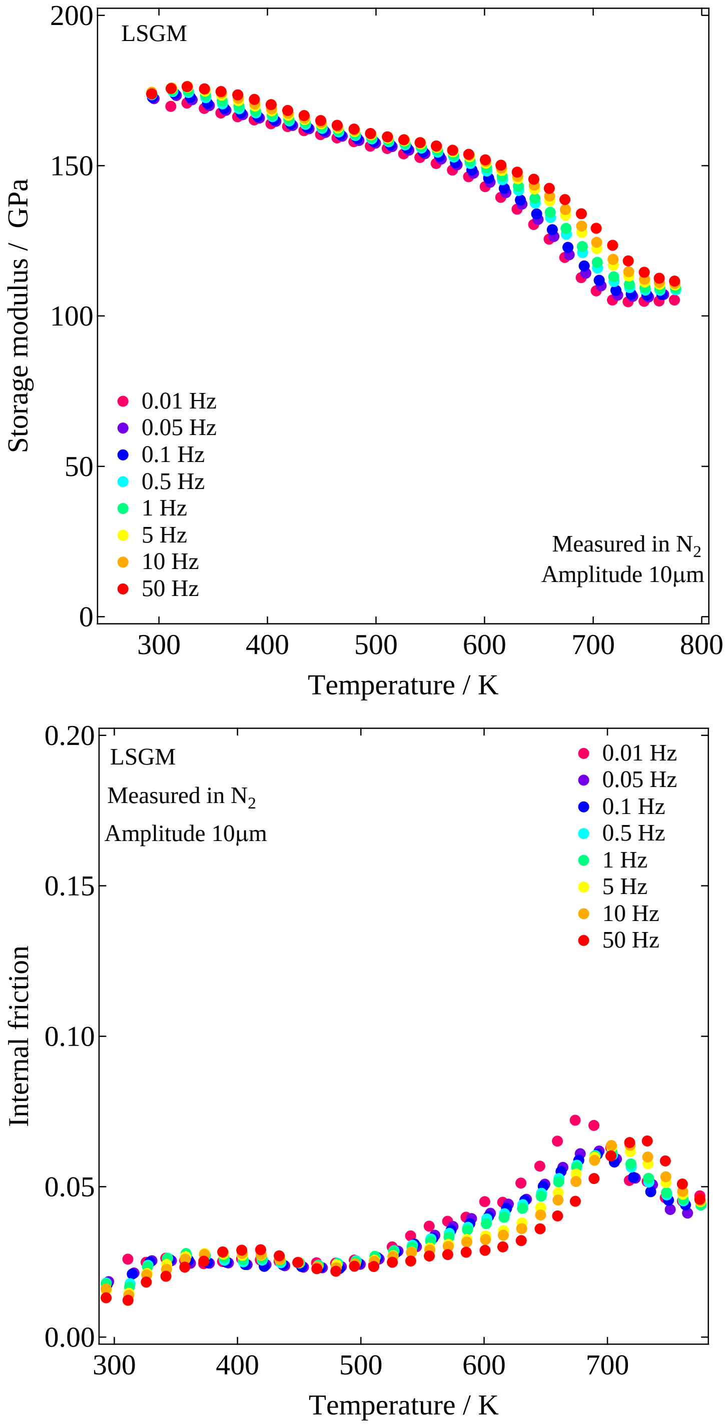

Figure 4.9. Temperature dependence of storage modulus (closed symbols) and of internal friction (open symbols) of LSGM annealed at 873 K under the $P(O_2)$ of 1 bar (LSCF1) in the frequency range from 0.01 to 50 Hz.

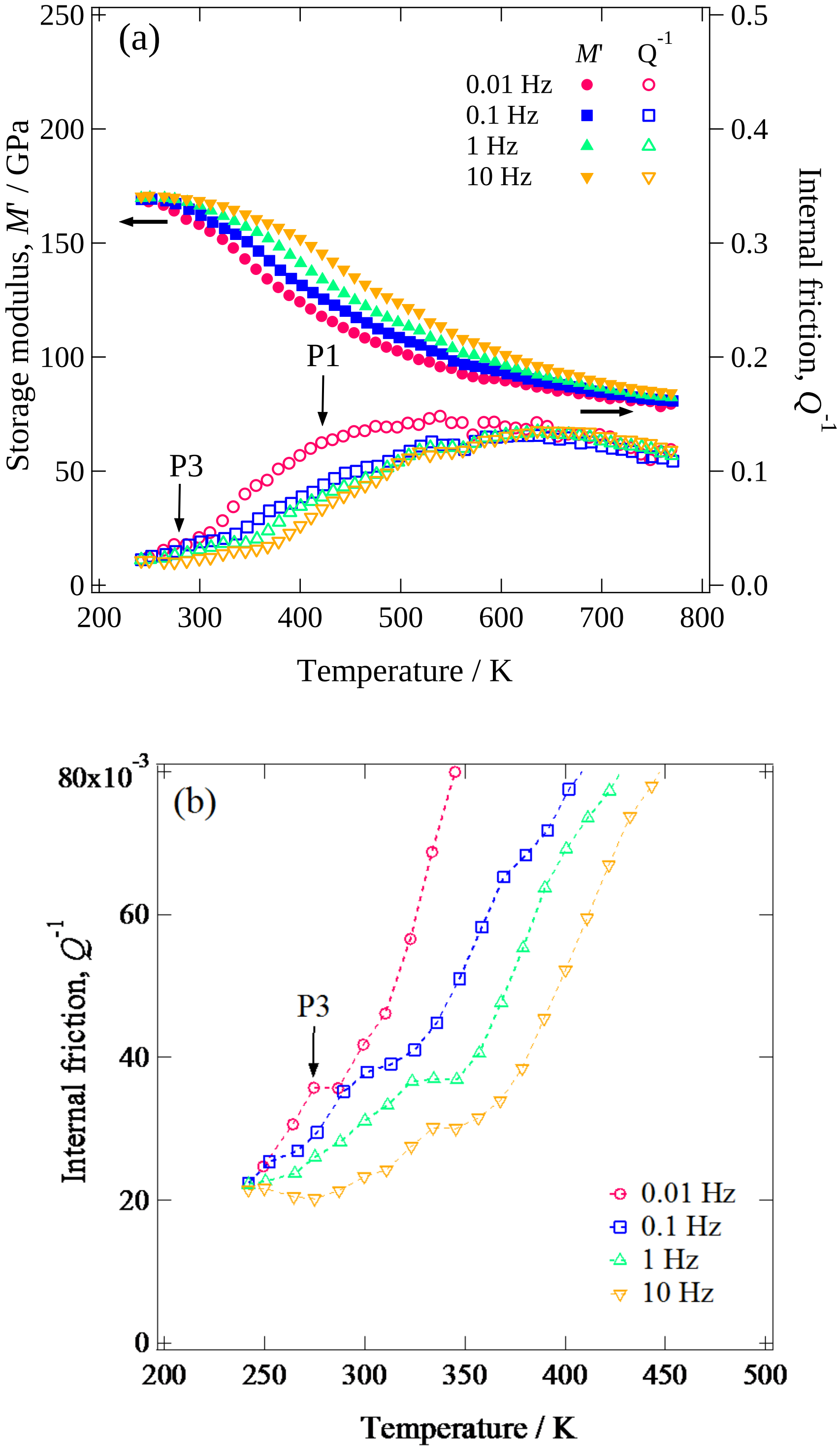

Figure 4.10. Temperature dependence of storage modulus (closed symbols) and of internal friction (open symbols) of LSCF6428 annealed at 973 K under the $P(O_2)$ of 10^{-2} bar (LSCF2) in the frequency range from 0.01 to 10 Hz.

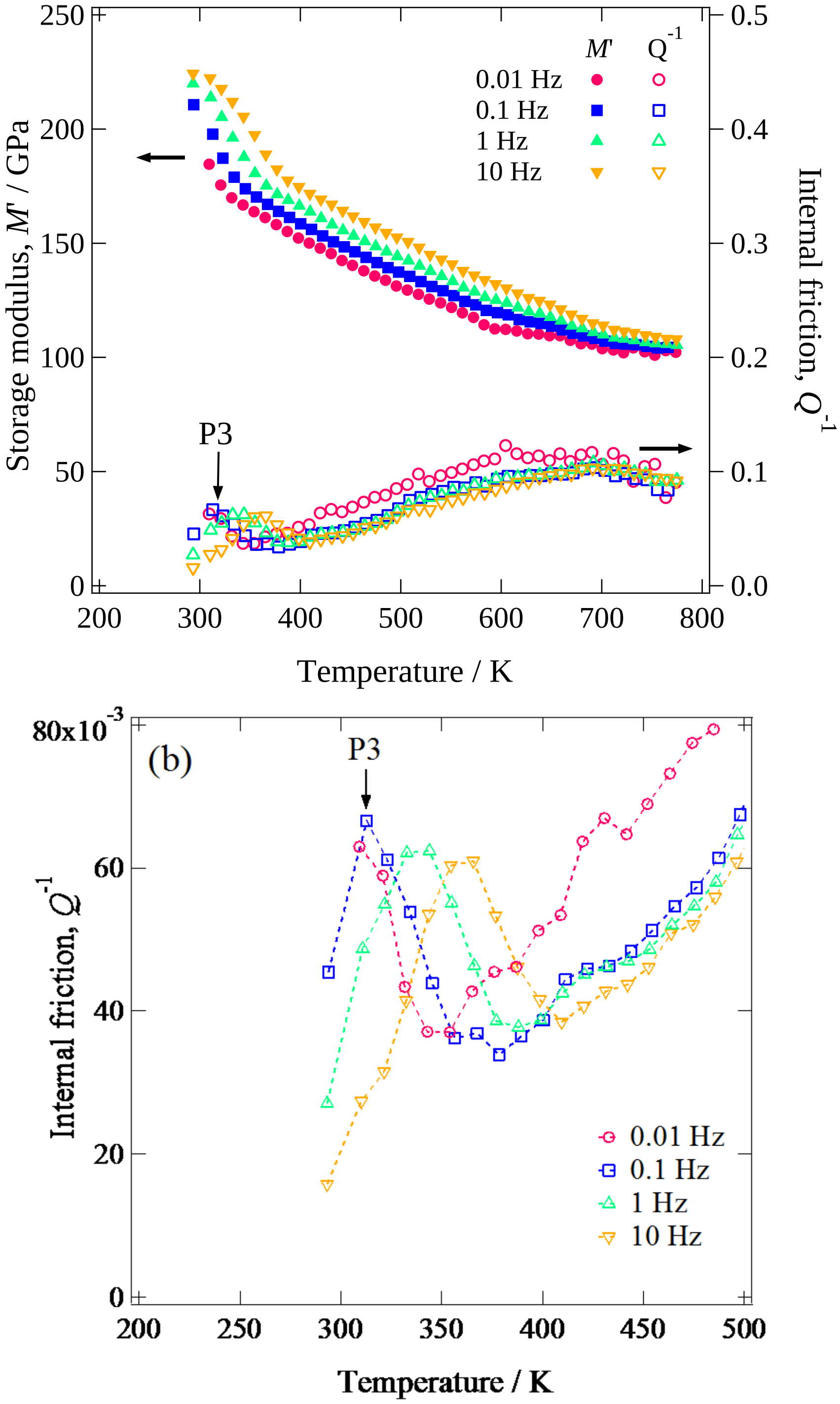

Figure 4.11. Temperature dependence of storage modulus (closed symbols) and of internal friction (open symbols) of LSCF6428 annealed at 973 K under the $P(O_2)$ of 10^{-4} bar (LSCF3) in the frequency range from 0.01 to 10 Hz.

4.4 Conclusions

The stress-strain relationship of LSC, LSCF6428 and LSF was evaluated by the uniaxial compression tests in the temperature range between room temperature and 1173 K. The nonlinear stress-strain relationship with a residual strain was observed below the phase transition temperature. On the other hand, the relationship was almost linear and almost no residual strain was observed above the phase transition temperature. Above 1073 K, the stress-strain relationship of LSCF seemed to be affected by a creep deformation. These results suggest that the stress-strain relationship of LSC, LSCF6428 and LSF is influenced by the ferroelastic domain switching below the phase transition temperature. Thus it is possible that the apparent Young's modulus of LSCF with rhombohedral symmetry depends on the applied stress. Above 473 K, the stress-strain relationship was nonlinear even starting from low stress levels. Therefore, the apparent Young's modulus may be sensitive to the applied stress even the applied stress is very small above 473 K.

The dynamic amplitude dependence of the Young's modulus and the internal friction of LSCF6428 and LN214 was evaluated. The Young's modulus and the internal friction of LN214 were independent of the dynamic amplitude at each temperature. The Young's modulus of LSCF6428 was independent of the dynamic amplitude at room temperature and 1073 K, while it gradually decreased with increasing the dynamic amplitude in the temperature range from 473 to 873 K. The internal friction was constant at room temperature and 1073 K but it gradually increased with increasing the dynamic amplitude between 473 and 873 K. The above dependence can be explained by the ferroelastic behavior of LSCF6428. Thus the drastic decrease in the Young's modulus observed in the resonance measurement at low temperatures may be associated with the ferroelasticity.

The temperature dependence of the dynamic Young's modulus and of the internal friction of LN214, LSCF6428, and LSGM was investigated by using the technique of dynamic mechanical analysis. The storage modulus of LN214 monotonically decreased with increasing temperature. Although the internal friction slightly increased at around 500 K, it was very small over the whole temperature range. The significant decrease in the storage modulus of LSCF6428 with low oxygen vacancy concentration (LSCF1) and a following broad and asymmetric peak (P1) was observed. Such a significant decrease in the storage modulus and a broad peak in the internal friction were also observed with LSGM with rhombohedral symmetry. This can be interpreted as due to the motion of ferroelastic domain walls with a distribution of the relaxation time. The storage modulus of the LSCF6428 with higher oxygen vacancy concentration (LSCF2 and 3) was significantly larger than that of LSCF1 particularly below at low temperatures. The P1 was barely observed while a small peak (P3) was observed in the internal friction of LSCF2 and 3. The peak height of P3 increased with increasing the oxygen vacancy concentration. It was suggested that the peak P3 was related with the movement of the oxygen vacancies. The increase in the storage modulus and the suppression of the peak P1 with increasing the oxygen vacancy concentration can be explained mainly by the pinning effect of the oxygen vacancies. This suggests that the oxygen vacancies play a vital role in determining the mobility of the ferroelastic domains in LSCF6428.

From the above measurement, it was found that the elastic modulus of ferroelastic perovskite oxides was strongly influenced by the ferroelastic domain switching. It is possible that the drastic decrease in the Young’s modulus of LSCF6428 observed in the resonance measurement at low temperatures is also associated with the ferroelasticity. Furthermore, it was suggested that the oxygen vacancies can influence the mechanical properties of LSCF even at low temperatures through the interaction with the ferroelastic domain walls.

References

[4.1] Y. Kimura, T. Kushi, S. Hashimoto, K. Amezawa, and T. Kawada, *J. Am. Ceram. Soc.*, **95**, 2608 (2012).

[4.2] J. B. Wachtman, Jr., W. E. Tefft, D. G. Lam, Jr., and C. S. Apstein, *Physical Review*, **122**, 1754 (1961).

[4.3] C. H. Kim, J. W. Jang, S. Y. Cho, I. T. Kim, and K. S. Hong, *Mater.*, *Physica B*, **262**, 438 (1999).

[4.4] P. E. Vullum, R. Holmestad, H. L. Lein, J. Mastin, M.–A. Einarsrud, and T. Grande, *Adv. Mater.*, **19**, 4399 (2007).

[4.5] W. Araki and J. Malzbender, *J. Euro. Ceram. Soc.*, **33**, 805 (2013).

[4.6] R. J. Harrison and S. A. T. Redfern, *Phys. Earth Planet. Inter.*, **134**, 253 (2002).

[4.7] R. J. Harrison, S. A. T. Redfern, and E. K. H. Salje, *Phys. Rev. B*, **69**, 144101-1 (2004).

[4.8] R. J. Harrison, S. A.T. Redfern, and J. Street, *Am. Mineral.*, **88**, 574 (2003).

[4.9] E. K. H. Salje and J. Zhang, *J. Phys.: Condens. Mater.*, **21**, 035901 (2009).

[4.10] M. Calleja, M. T. Dove, and E. K. H. Salje, *J. Phys.: Condens. Mater.*, **15**, 2301

(2003).

[4.11] S. Hashimoto, Y. Fukuda, M. Kuhn, K. Sato, K. Yashiro, and J. Mizusaki, *Solid State Ionics*, **181**, 1713 (2010).

[4.12] S. Faaland, T. Grande, M.-A. Einarsrud, P. E. Vullum, R. Holmestad, *J. Am. Ceram. Soc.*, **88**, 726 (2005).

[4.13] K. Yashiro, I. Nakano, M. Kuhn, S. Hashimoto, K. Sato, and J. Mizusaki, *ECS Trans.*, **35(1)**, 1899 (2011).

[4.14] B. X. Huang, J. Malzbender, R. W. Steinbrech and L. Singheiser, *Solid State Ionics*, **180**, 241 (2009).

[4.15] H. L. Lein, O. S. Andersen, P. E. Vullum, E. Lara-Curzio, R. Holmestad, M.-A. Einarsrud and T. Grande, *J. Solid State Electrochem.*, **10**, 635 (2006).

[4.16] J. Mastin, M.-A. Einarsrud and T. Grande, *Chem. Mater.*, **18**, 6047 (2006).

[4.17] A. Fossdal, M. Menon, I. Wærnhus, K. Wiik, M.-A. Einarsrud and T. Grande, *J. Am. Ceram. Soc.*, **87**, 1952 (2004).

[4.18] M. Zimmermann and W. Schranz, *J. Phys.: Condens. Mater.*, **8**, 7085 (2009).

[4.19] M. Daraktchiev, E. K. H. Salje, W. L. Lee, and S. A. T. Redfern, *Phys. Rev. B*, **75**, 134102 (2007).

[4.20] A.S. Nowick and B.S. Berry, *Anelastic Relaxtion in Crystalline Solids*, p. 55, Academic Press, New York, 1972.

[4.21] T. Okamura, S. Shimizu, M. Mogi, M. Tanimura, K. Furuya, F. Munakata, *J. Power Sources*, **130**, 38 (2004).

[4.22] K. Aizu, *J. Phys. Soc. Japan*, **27**, 387 (1969).

[4.23] F. Cordero, *Phys. Rev. B*, **76**, 172106 (2007).

[4.24] M. Daraktchiev, R. J. Harrison, E. H. Mountstevens, and S. A. T. Redfern, *Mater. Sci. Eng. A*, **442**, 199 (2006).

[4.25] A. Mineshige, M. Kobune, S. Fujii, Z. Ogumi, M. Inaba, T. Yao, and K. Kikuchi, *J. Solid State Chem.*, **142**, 374 (1999).

[4.26] M. Kuhn, S. Hashimoto, K. Sato, K. Yashiro, and J. Mizusaki, *Solid State Ionics*, **195**, 7 (2011).

Chapter 5

Simulation of the stress distribution in energy conversion devices with perovskite and related oxides

5.1 Introduction

So far we found that the mechanical properties of perovskite and related oxides significantly change at high temperatures and under controlled atmospheres due to the changes in defect concentrations and the ferroelastic domain switching. The changes in mechanical properties due to the changes in defect concentration and the ferroelastic domain switching can be a critical problem because those oxides are often used as components of the energy conversion devices and exposed to high temperatures and a certain oxygen potential gradient. Thus the actual stress distribution in the energy conversion devices during operation can be influenced by the change in the mechanical properties of perovskite and related oxides. So far, a number of numerical simulations have been performed in order to evaluate the stress distribution under operation and understand mechanisms of the mechanical degradation [1-5]. In most of such studies, however, the data of mechanical properties at room temperature in air have been frequently used [1-5], because the data at high temperatures and under controlled atmospheres are limited. It is thus important to evaluate the influence of the change in the mechanical properties on the stress distribution in the energy conversion devices.

It is considered that the change in the defect concentration will be more influential at higher temperatures. On the other hand, the influence of the ferroelastic domain switching becomes most significant in the low and medium temperature ranges because the low symmetry phase of the materials often exhibit the ferroelasticity.

Therefore, in this study, two cases of simulations were performed in order to separately examine the influence of the change in the defect concentration and the domain switching on the stress distribution in the energy conversion devices. In one simulation, the stress distribution in a simple planer SOFC cell was calculated, considering the $P(O_2)$ dependence of the mechanical properties of LSCF6428. In another study, the ferroelastic behavior of LSCF6428 was described by shape memory effect model and the stress distribution in a simple planer cell with LSCF cathode was calculated by ANSYS.

5.2 Influence of the change in oxygen vacancy concentration on the stress distribution in a simple planer SOFC cell

5.2.1 Modeling

The stress distribution in a simple electrolyte supported planer-type SOFC cell was calculated. The anode, the electrolyte, and the cathode of the cell were Ni-YSZ cermet (Ni-YSZ), 8% yittria stabilized zirconia (8YSZ), and LSCF6428, respectively. LSCF6428 and Ni-YSZ cermet were assumed to be baked on 8YSZ at 1273 K and then the cell was cooled to 873, 973, and 1073 K. The in-plane biaxial stress in each component was calculated at each temperature. The thicknesses of LSCF6428, 8YSZ, and Ni-8YSZ cermet were assumed to be 50, 100, and 50 μm, respectively (Fig. 5.1 (a)). We assumed that there was an effective reaction zone (ERZ) in the cathode, and for simplicity, the oxygen potential linearly changed in the ERZ. The thickness of the ERZ was assumed to be 4μm, according to literatures [6, 7]. The change in oxygen potential in the ERZ was set to be comparable to the overpotential, η, of 100 mV (Fig. 5.1 (b)). At 1273 K, LSCF6428 and Ni-YSZ cermet were jointed to 8YSZ and there was no stress in the cell. However, at 873, 973, and 1073 K, the strains resulting from the thermal and the chemical expansion generate stresses to maintain dimensional compatibility between materials. The cell was assumed to be simply supported and was free to deform without restraint. Also we assumed that the lateral dimension of the cell was much greater than its thickness and the bending was small with the curvature, κ. The general solution of this problem for the in-plane biaxial stress, σ, as a function of position from the origin, z, was given by L. B. Freund *et al.* [8, 9] as follows;

$$\sigma = \hat{E}(z)\left[\kappa(\bar{z} - z) - \varepsilon(z)\right] \qquad [5.1]$$

where $\hat{E}$ is the effective biaxial modulus, which is related to Young's modulus, E, and

Poisson's ratio, μ, by

$$\hat{E} = \frac{E}{1-\mu} \qquad [5.2]$$

The κ and $\bar{z}$ are given by the following equations, respectively;

$$\kappa = \frac{I_0 J_1 - I_1 J_0}{I_1^{\,2} - I_2 I_0} \qquad [5.3]$$

$$\bar{z} = \frac{\kappa I_1 + J_0}{\kappa I_0} \qquad [5.4]$$

In the above equations, I_n and J_n are given by;

$$I_n = \int_{h_1}^{h_2} \hat{E}(z) z^n dz \qquad [5.5]$$

and

$$J_n = \int_{h_1}^{h_2} \hat{E}(z) z^n \varepsilon dz \qquad [5.6]$$

where h_1 and h_2 are the z-position of each material and ε is strain. The origin of the z-axis was set at the interface between the anode and the cathode.

In order to evaluate the influence of the $P(O_2)$ dependence of the mechanical properties on the stress distribution, the following three cases are considered; the Young's modulus and the Poisson's ratio of LSCF6428 are independent of temperature and $P(O_2)$ and have the value at room temperature, 163 GPa and 0.29, respectively (case 1); the Young's modulus and the Poisson's ratio of LSCF6428 depend on temperature but independent of $P(O_2)$, and have the values under the $P(O_2)$ of 0.1 bar (case 2); the Young's modulus and the Poisson's ratio of LSCF6428 depend on both temperature and $P(O_2)$ (case 3). The Young's modulus and the Poisson's ratio of LSCF6428 and their $P(O_2)$ dependence were taken from the data in chapter 3. The Young's modulus and the Poisson's ratio of 8YSZ and Ni-YSZ, and the thermal expansion coefficients of LSCF6428, 8YSZ, Ni-YSZ were taken from literatures and summarized in Table 5.1.

Table 5.1 Components of the planer cell and their mechanical properties and thermal expansion coefficient.

Constants	LSCF6428	8YSZ	Ni-YSZ
Young's moudulus / GPa	**--**	**873 K: 139 [11]**	**873 K: 55 [13]**
	--	**973 K: 144 [11]**	**973 K: 55 [13]**
	--	**1073 K: 152 [11]**	**1073 K: 55 [13]**
Poisson's ratio	**--**	**873 K: 0.41 [11]**	**873 K: 0.39 [14]**
	--	**973 K: 0.40 [11]**	**973 K: 0.39 [14]**
	--	**1073 K: 0.41 [11]**	**1073 K: 0.39 [14]**
Thermal expansion coefficient / K^{-1}	**1.32×10^{-5} [10]**	**1.05×10^{-5} [12]**	**1.26×10^{-5} [15]**

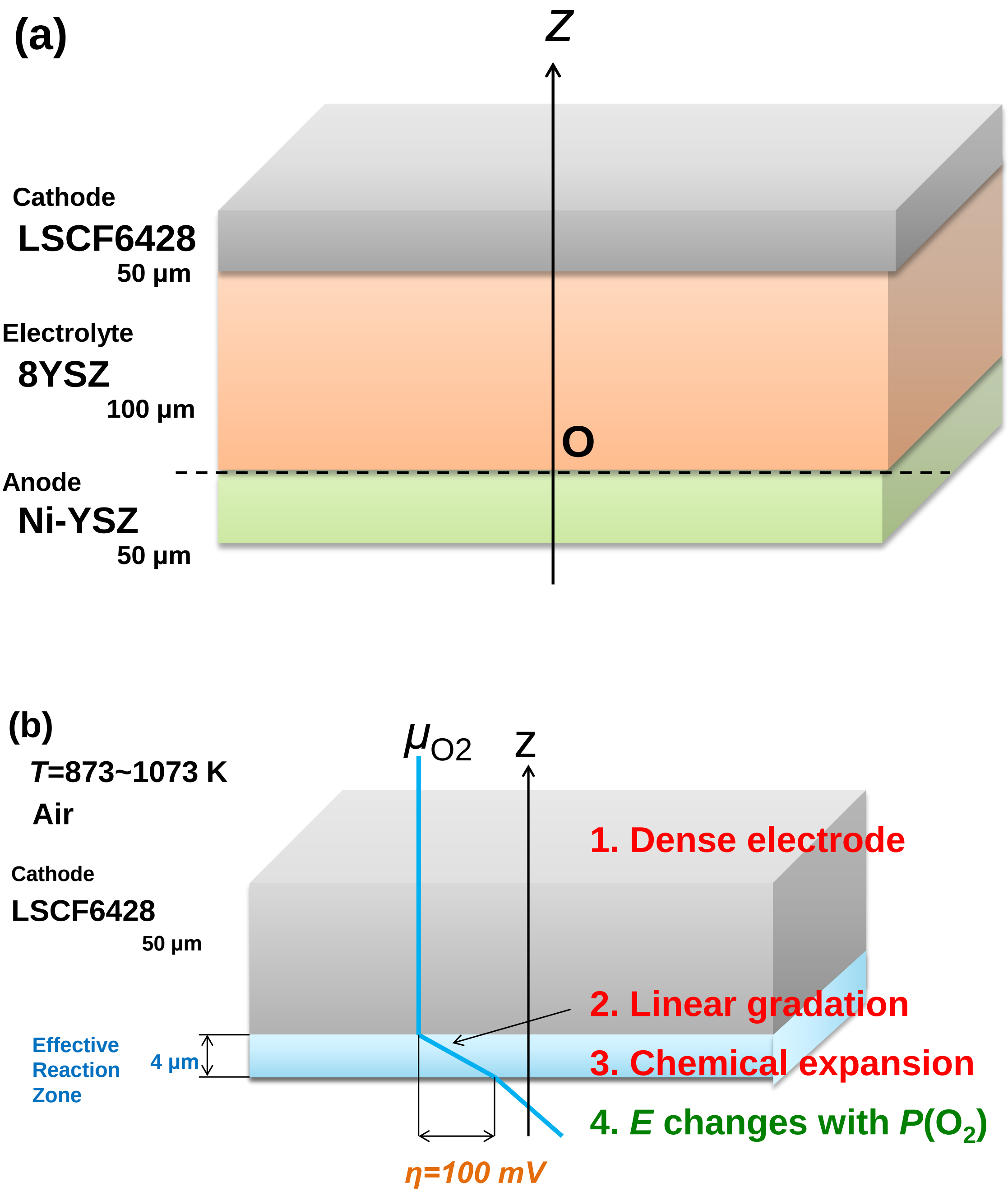

Fig. 5.1 (a) Overall view of the planer cell, (b) Cathode part and the effective reaction zone (ERZ) in the cathode of the planer cell.

5.2.2 Simulation results

Figures 5.2 (a)-(c) show the in-plane biaxial stress distribution in the planer cell along the *z*-axis at 873, 973, and 1073 K, respectively. At each temperature, the anode (Ni-YSZ) was exposed to a tensile stress while the electrolyte (8YSZ) was essentially exposed to a compressive stress. The stress discontinuously changed at the interface between the anode and the electrolyte. The stress gap at the interface between the anode and the electrolyte was larger at lower temperature. The stress distribution in the anode was almost the same in the three cases. In the electrolyte, the compressive stress became larger with approaching to the cathode (LSCF6428) at each temperature. At the interface between the electrolyte and the cathode, the stress discontinuously changed and the tensile stress was generated at the cathode-side. The tensile stress at the cathode side was largest at 1073 K and decreased with decreasing temperature. The tensile stress in the cathode significantly decreased in the ERZ with increasing distance from the interface. Outside the ERZ, the stress gradually decreased with increasing distance from the interface. At 873 K, the cathode was exposed to the tensile stress while it was mostly exposed to the compressive stress at 973 and 1073 K aside from the ERZ.

There was a certain difference in the stress distribution in case 3, and cases 1 and 2. This is because the effective biaxial modulus of LSCF6428 at room temperature is higher than the one at higher temperatures. The difference in the stress distribution was more significant near the cathode. The compressive stress in the electrolyte at the interface between the electrolyte and the cathode in case 3 was larger than that of cases 1 and 2. Accordingly, the tensile stress in the cathode at the interface and the compressive stress in the cathode in case 3 are also larger than those of cases 1 and 2. On the other hand, almost no difference in the stress distribution in case 1 and case 2 is observed at each temperature. This is not surprising at 873 and 1073 K since the Young’s modulus and the Poisson’s ratio of LSCF6428 have no great dependence on $P(O_2)$ and thus the effective biaxial modulus is also independent of $P(O_2)$. At 973 K, the Young’s modulus of LSCF6428 increases by approximately 40 % in the ERZ with approaching to the interface due to the changes in the oxygen potential. However, the difference in the tensile stress in the cathode at the interface in cases 1 and 2 was only ~ 10 MPa. This is partly because the Poisson’s ratio of LSCF6428 simultaneously decreases about 30 % with approaching to the interface. Thus the difference in the effective biaxial modulus at the interface and another edge of the ERZ is only approximately 20 %. This result suggests that the $P(O_2)$ dependence of the Young’s modulus and the Poisson's ratio of LSCF6428 does not have the significant influence on the stress distribution in SOFCs.

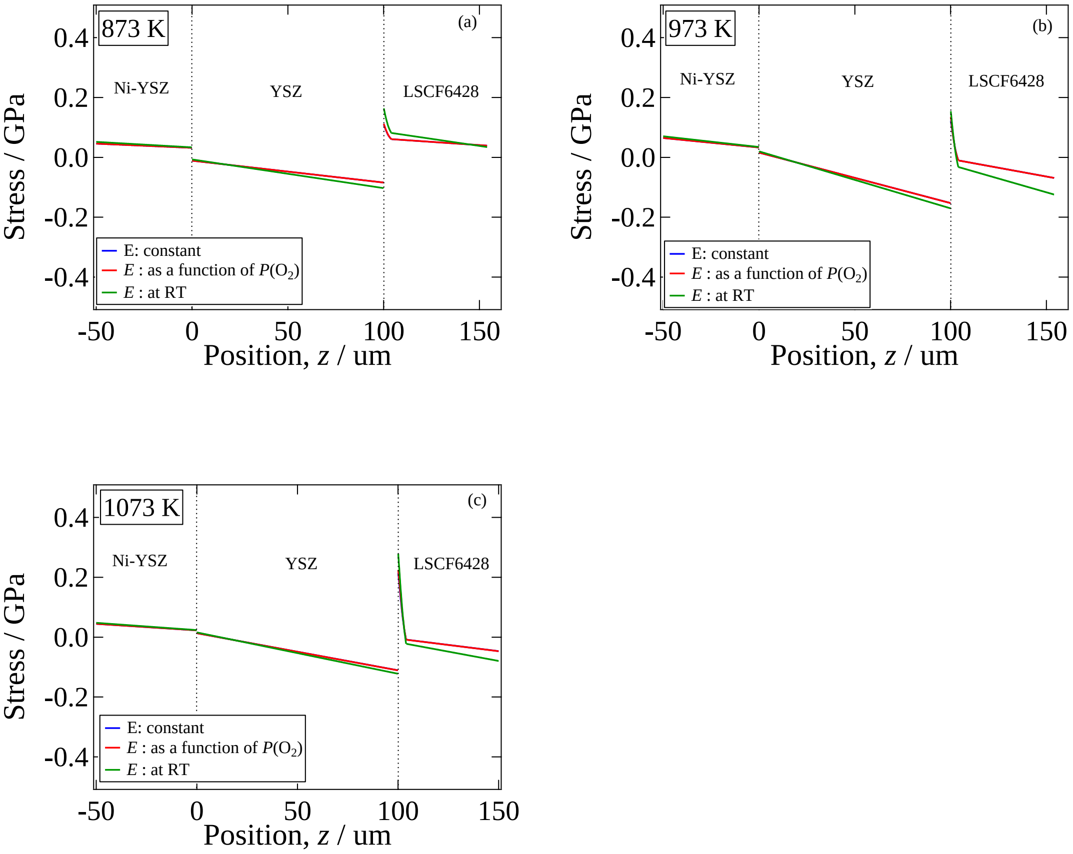

Fig. 5.2 Stress distribution in the planer cell along the *z*-axis (a) at 873 K, (b) at 973 K, and (c) at 1073 K. The *z*-axis lies perpendicular to the cell and the origin is at the interface between the anode and the electrolyte.

5.3 Influence of the ferroelastic domain switching on the stress distribution in a simple planer SOFC cell

5.3.1 Modeling using shape memory effect (SME) model

The ferroelastic materials have a characteristic stress-strain relationship. That is, under loading, the stress-strain relationship is linear when applied stress is low. However, it becomes nonlinear when the applied stress surpasses a certain value due to the ferroelastic domain switching. It again becomes linear after the ferroelastic domain switching is completed. Under unloading, the material deforms basically elastically, preserving the strain due to the ferroelastic switching. Thus the stress-strain relationship is linear under unloading and the residual strain is observed after unloading. If the material is successively exposed to a loading and unloading cycle again, then the material deforms only elastically. The residual strain will disappear and the material recovers its original shape if the material is heated above the phase transition temperature.

In order to describe such a characteristic stress-strain relationship, the shape memory effect model (SME) was applied in this study [16-18]. The shape memory alloy (SMA) is a metallic alloy that "remembers" its original shape. This alloy has high-symmetry austenite (A) phase at high temperatures and low stress. On the other hand, it has low-symmetry martensite (M) phase at low temperatures and high stress. The SMA undergoes a martensitic phase transformation between those two phases. This reversible martensitic phase transformation results in unique effects: the pseudoelasticity (PE) and the shape memory effect (SME). The pseudoelasticity is associated with a stress-induced phase transformation between a parent phase (austenite or twinned martensite) and a product phase (detwinned martensite) at constant temperature. Figure 5.1 (a) shows the stress-strain relationship of a pseudoelastic material. When the applied stress is low, the material is assumed to have its parent phase which presents an elastic behavior (line AB in Fig. 5.1 (a)). If the applied stress surpasses a certain value (σ_H) then the material undergoes a stress-induced phase transformation to the product phase (curve BC). At a sufficiently high stress (point C), the phase transformation is completed and further loading leads to an elastic behavior of the product phase (line CD). If the material is unloaded from D, then the material deforms elastically (line DE). If the parameter σ_L is positive, then an inverse transformation from the product phase to the parent one takes place until all the product phase disappears (curve EF). At the point F, the inverse transformation is completed. This means there is only the parent phase in the material. Thus the material deforms elastically under lower stress (line FA) and the material recovers completely its original shape. The parameters σ_H and σ_L decrease with decreasing temperature and the σ_L eventually becomes negative at a certain temperature. This case is shown in Figure 5.1 (b). A distinct feature of this case is that the material does not undergo the inverse transformation during unloading and the residual strain due to the twinning can be observed after unloading (Point E in Fig.5.1 (b)). If the material is heated to a certain temperature, then there exists only the parent phase in the material. Consequently, the residual strain disappears and the material recovers its original shape. This effect is called SME.

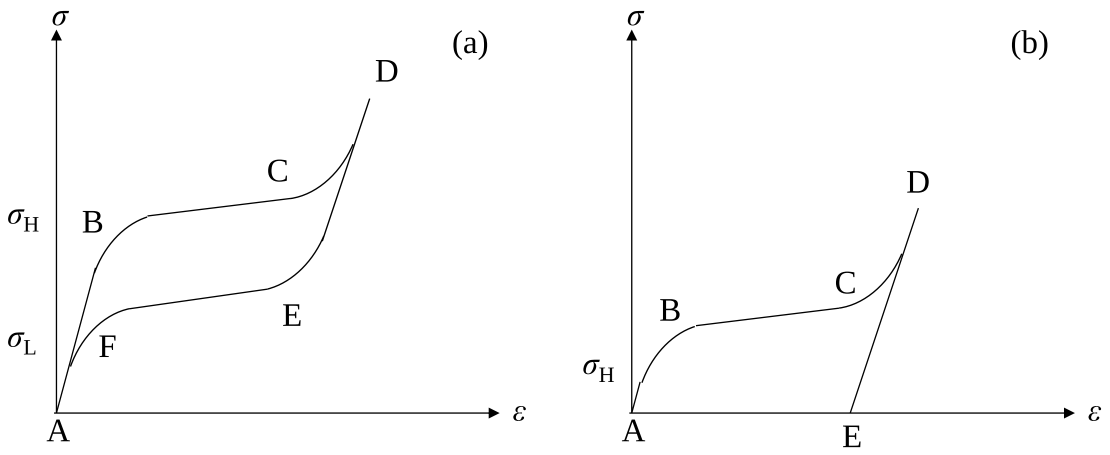

Fig. 5.3 Typical stress-strain curve of shape memory alloys (a) at high temperatures (PE) and (b) at low temperatures (SME).

Therefore, both of the SME and the ferroelastic behavior observed in perovskite and related oxides have essentially the same mechanism; both are related with the twinning in the low symmetry phase and the disappearance of the twins in the high symmetry phase. Thus it may be possible to describe the ferroelastic behavior of perovskite and related oxides by SME model.

An engineering simulation software, ANSYS, can simulate the SME behavior of shape memory alloys. Therefore, in this study, the ferroelastic behavior of LSCF6428 was simulated by using ANSYS. Figure 5.4 (a) shows a typical stress-strain curve of

SME behavior. In ANSYS, this behavior is modeled by a broken line as shown in Fig.5.4 (b). Also, the stress-temperature diagram of SMA is modeled as shown in Fig.5.4 (c). The lines AB and DE correspond to the elastic regions of twinned and detwined phases, respectively. The line BC indicates the region in which the twinning is undertaken. In ANSYS, such a stress-strain curve and the thermal loading behavior of SMA are determined by seven constants. Those seven constants are summarized in table 5.2. E_{m} is the elastic modulus, which is assumed to be identical for twinned and detwinned phases. $\bar{\varepsilon}_{\mathrm{L}}$ is the maximum transformation strain which determines the magnitude of a residual strain. R is the elastic limit, which determines the maximum stress below which the material can deform only elastically. h is the hardening parameter, which determines the slope of the line BC. m is the lode dependency parameter, which is related to the uniaxial elastic limit in compression σ_{H} and in tension σ_{T} by the relation;

$$m=\sqrt{\frac{27}{2}}\cdot\frac{\sigma_{\mathrm{H}}-\sigma_{\mathrm{T}}}{\sigma_{\mathrm{H}}+\sigma_{\mathrm{T}}} \qquad [5.7]$$

T_0 is the reference temperature. β is the temperature scaling parameter which determines the slope of the elastic limit above the reference temperature. In order to determine the above seven parameters, the stress-strain curve of LSCF6428, which was measured by the uniaxial compression tests, was fitted by a broken line using a broken line regression analysis program. Figure 5.5 shows the stress-strain curve of LSCF6428 and the fitting lines at each temperature. The obtained seven constants at each temperature were summarized in table 5.2. Since the elastic modulus is assumed to be identical for twinned and detwinned phases in ANSYS, the discrepancy was observed between the fitting lines and the experimental results under lower stress at room temperature. At higher temperatures, the nonlinear stress-strain relationship is observed from almost the onset of the loading. Because of this, the elastic limit was estimated to be higher than the actual ones. On the other hand, the residual strain was well described by fitting lines and the slope of the stress-strain curve under unloading also agreed well with the experimental results.

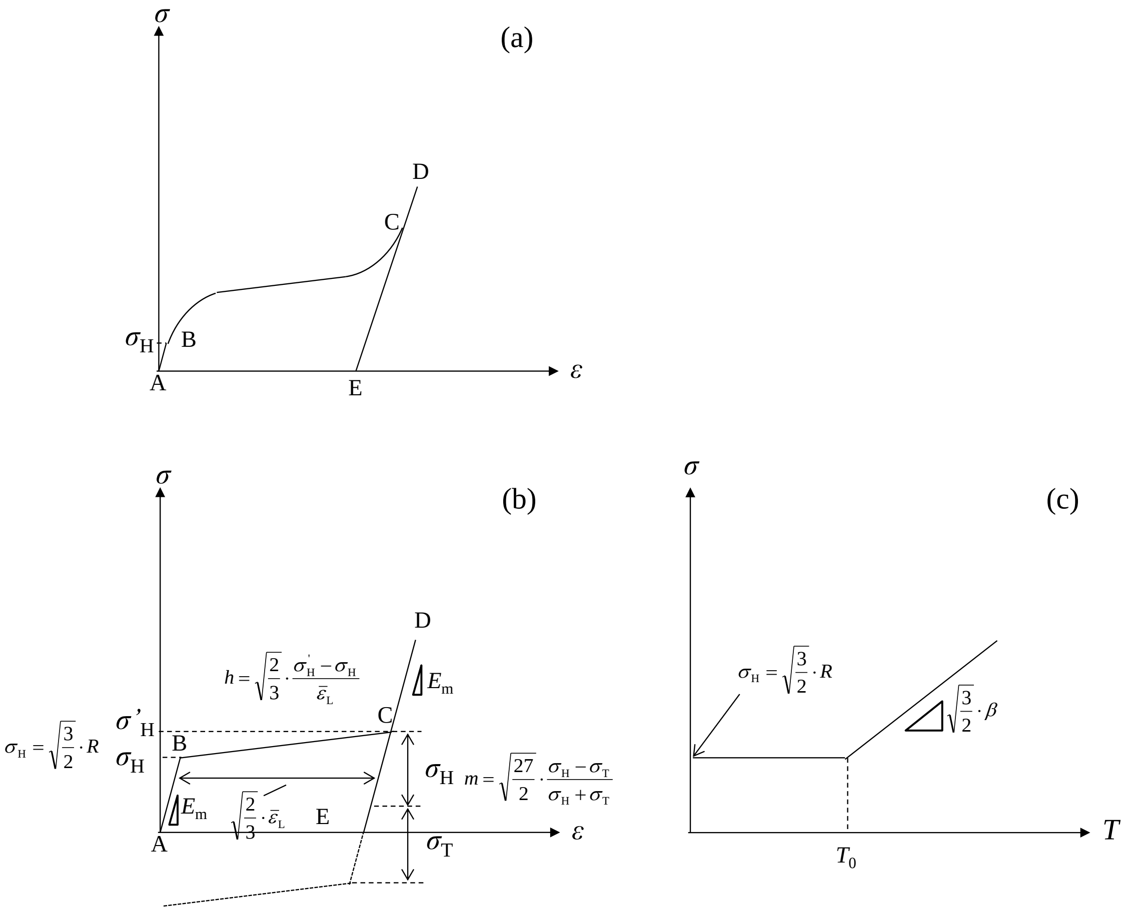

Figure 5.4 (a) shows a typical stress-strain curve of SMA; (b) the stress-strain curve of SMA modeled by ANSYS; and (c) stress-temperature diagram of SMA.

Table 5.2 Constants to model the shape memory effect.

Constants	Properties
$\boldsymbol{E_m}$	**Elastic modulus**
$\boldsymbol{\bar{\varepsilon}_L}$	**Maximum transformation strain**
$\boldsymbol{R}$	**Elastic limit**
$\boldsymbol{h}$	**Hardening parameter**
$\boldsymbol{m}$	**Lode dependency parameter**
$\boldsymbol{T_0}$	**Reference temperature**
$\boldsymbol{\beta}$	**Temperature scaling parameter**

Table 5.3 Constants to model the shape memory effect at each temperature determined from the stress-strain curve of LSCF6428.

Temperature /	E_m		R	h	m	T_0	B
K	/ MPa	$\bar{\varepsilon}_L$	/ MPa	/ MPa		/ K	/ MPa・K^{-1}
298	112	0.00325	78.0	23.6	0	653	1E+10
473	68.5	0.00316	30.1	10.7	0.06	653	1E+10
673	73.0	0.00219	26.5	13.8	0.08	653	1E+10
873	135	0.00139	16.1	12.8	0.01	653	1E+10

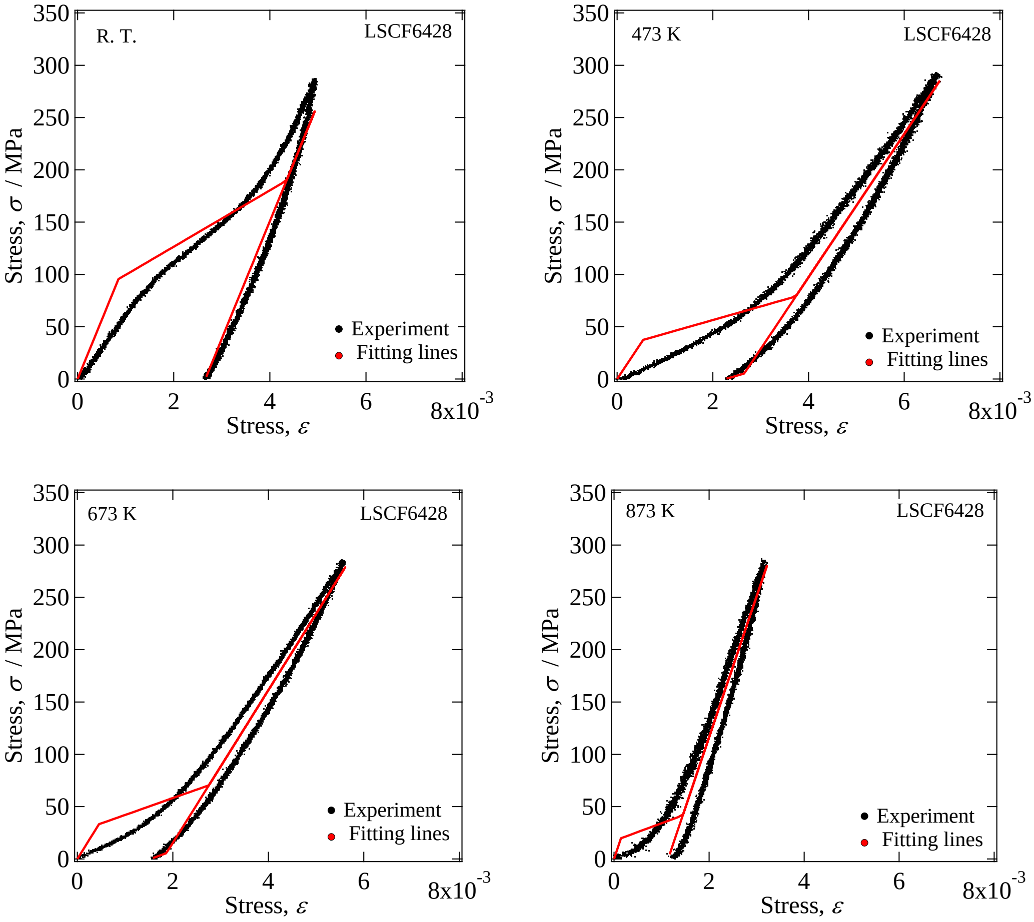

Fig. 5.5 The stress-strain curve of LSCF6428 and the fitting lines at each temperature.

5.3.2 Simulation of uniaxial compression tests and a thermal cycle

The uniaxial compression tests of LSCF6428 and a thermal cycle were simulated by ANSYS, using the seven parameters obtained by the fitting, in order to see if the SME model can describe the characteristic ferroelastic behaviors of LSCF6428. The sample dimension in the simulation was set to be the same as the one used in the uniaxial compression tests performed in the chapter 4; radius 2.5 mm × height 10mm. Considering the axial symmetry, the behavior of the rectangle shape with the dimension of 2.5 mm × 10mm was simulated as shown in Fig. 5.6. The frictionless support was applied on one short side and one long side of the rectangle. A time-dependent pressure was applied to another short side of the rectangle from 0 to 350 MPa. Figure 5.7 shows the uniaxial compression test at room temperature. Not surprisingly, the stress-strain curve was the same as the fitting curve. After the first loading and unloading cycle, which was drawn by a blue line, the second loading and unloading cycle was subsequently applied. In the second cycle, then the sample deformed only elastically, preserving the residual strain. This result agrees well with the result of the actual cyclic uniaxial compression tests. Similarly, the stress-strain curve was the same as the fitting curve and the results of the cyclic tests were well described at other temperatures.

The effect of the thermal cycle was also simulated with the same sample model. Figure 5.8 (a) shows the loading and thermal history of this simulation as a function of normalized time. The sample was first exposed to a loading and unloading cycle at room temperature and then heated to 1173 K and cooled to room temperature without stress. Figure 5.8 (b) shows the compressive stress and the compressive strain of the sample. After the loading and unloading cycle ($t = 0.5$), the residual strain was observed. During heating, the sample expanded linearly but when the temperature reached at 973 K, which was assumed to be the phase transition temperature, the strain of the sample discontinuously changed, this means that the strain due to the ferroelastic twinning was released at the phase transition temperature. Above 973 K, the sample again expanded linearly. After the cooling, the sample completely recovered its original shape. Thus the strain due to the twinning which was generated in the loading process was completely released after the thermal cycle.

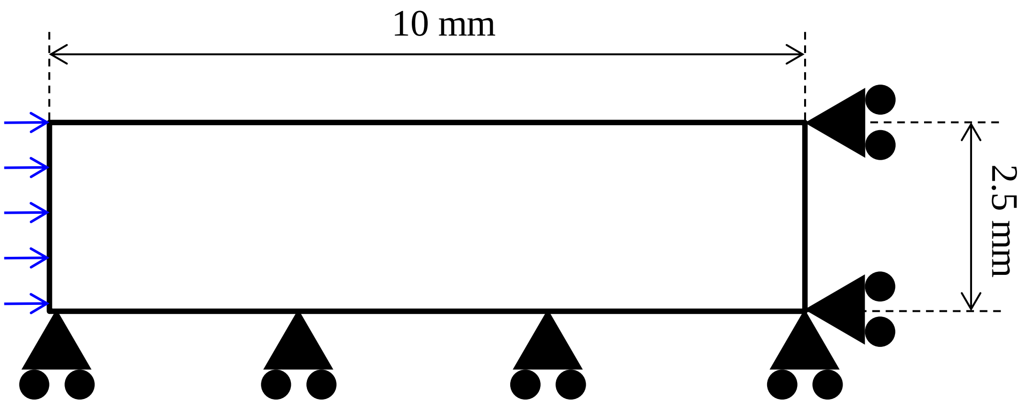

Fig. 5.6 Geometry of the model for the uniaxial compression tests

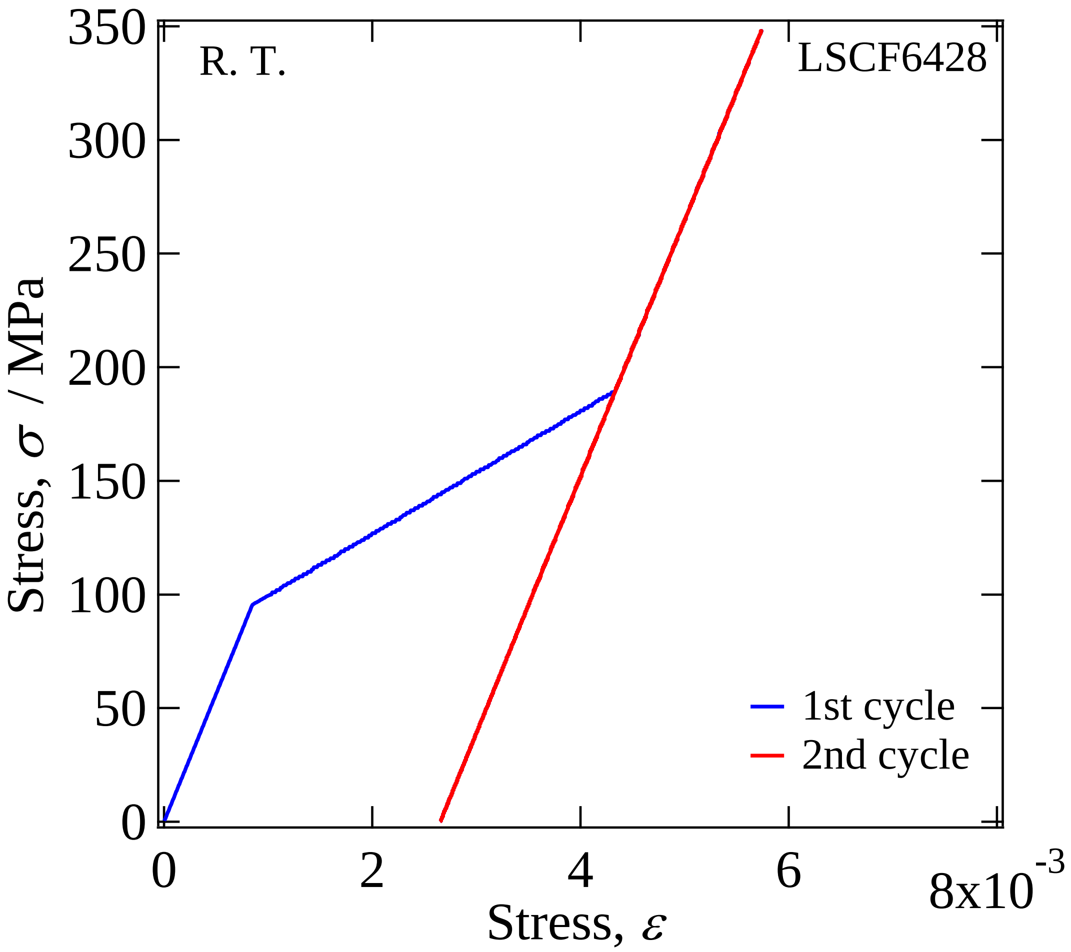

Fig. 5.7 Simulation result of the cyclic uniaxial compression test

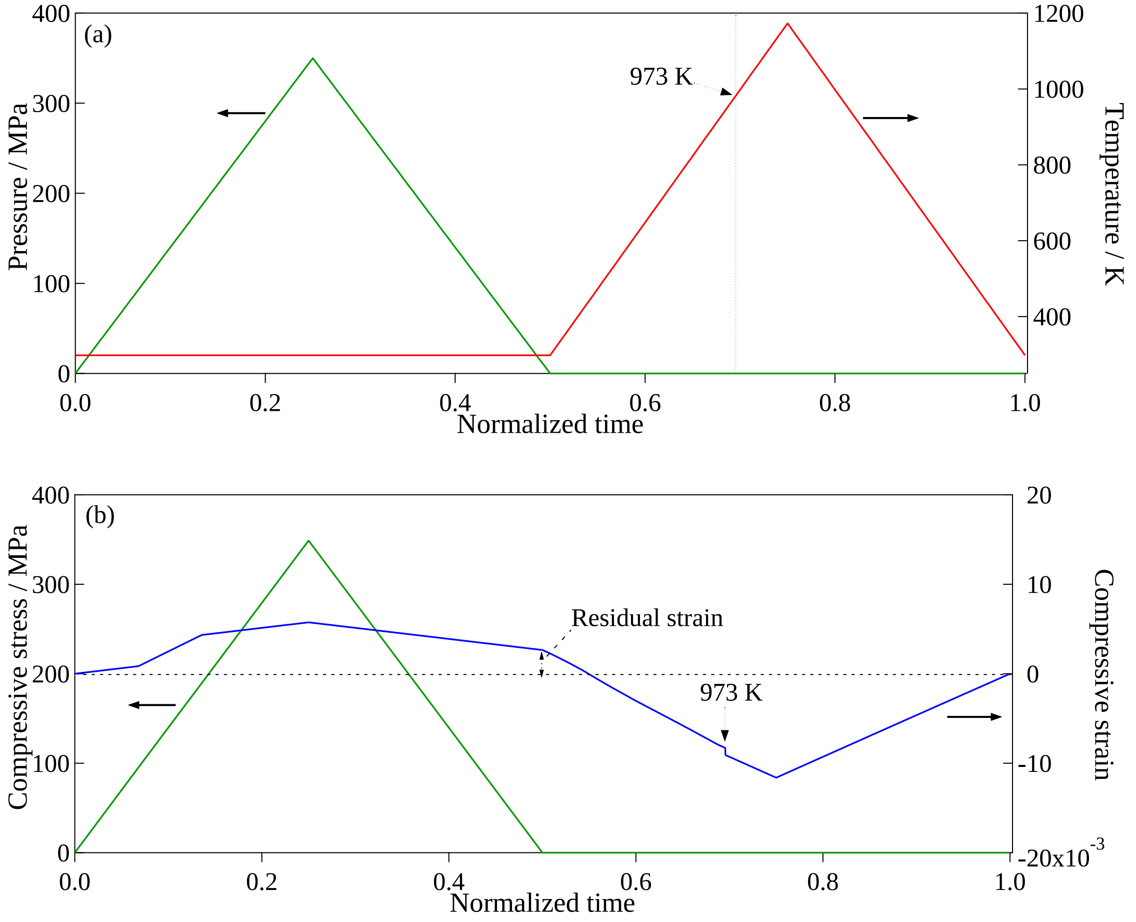

Figure 5.8 (a) Loading and thermal history on the sample, (b) compressive stress and compressive strain of the sample as a function of normalized time.

5.3.3 Simulation of the stress distribution in a simple planer cell during cooling process

The stress distribution in a simple planer cell during cooling process was simulated. The cell was an anode-supported cell and composed of Ni-8YSZ cermet, 8YSZ, 10 % gadolinium doped ceria (10GDC), and LSCF6482, which were used as an anode, an electrolyte, a diffusion layer, and a cathode of the cell, respectively. Figure 5.9 (a) shows the geometry of the model of the planer cell. The length of the cell was 40 mm and the thicknesses of an anode, an electrolyte, a diffusion layer, and a cathode were 400, 12, 3, 22 μm, respectively. Considering the symmetry of the cell, the half part of the two dimensional cell was simulated. The frictionless support was applied on one short side of the cell and the movement in direction of *y*-axis of bottom-right vertex of the cell was fixed (Fig. 5.9 (b)). The following condition was considered; the cell was cooled from 873 K to 298 K. At 873 K, there is no stress in the cell while the stress is generated in the cell during cooling due to the shrinkage of each component with different TEC. The values of the Young's modulus, the Poisson's ratio, and TEC of Ni-8YSZ cermet [15, 19], 8YSZ [11, 12], 10GDC [11, 20] were taken from literatures. The Young's modulus and the Poisson's ratio of the above materials were assumed to be temperature dependent. In order to evaluate the influence of the ferroelasticity of LSCF6428, the following 2 cases were considered. In case 1, the SME model was applied for LSCF6428. In case 2, LSCF6428 was assumed to be elastic and have the values of the Young's modulus and Poisson's ratio at room temperature. The phase transition temperature was assumed to be 973 K [21].

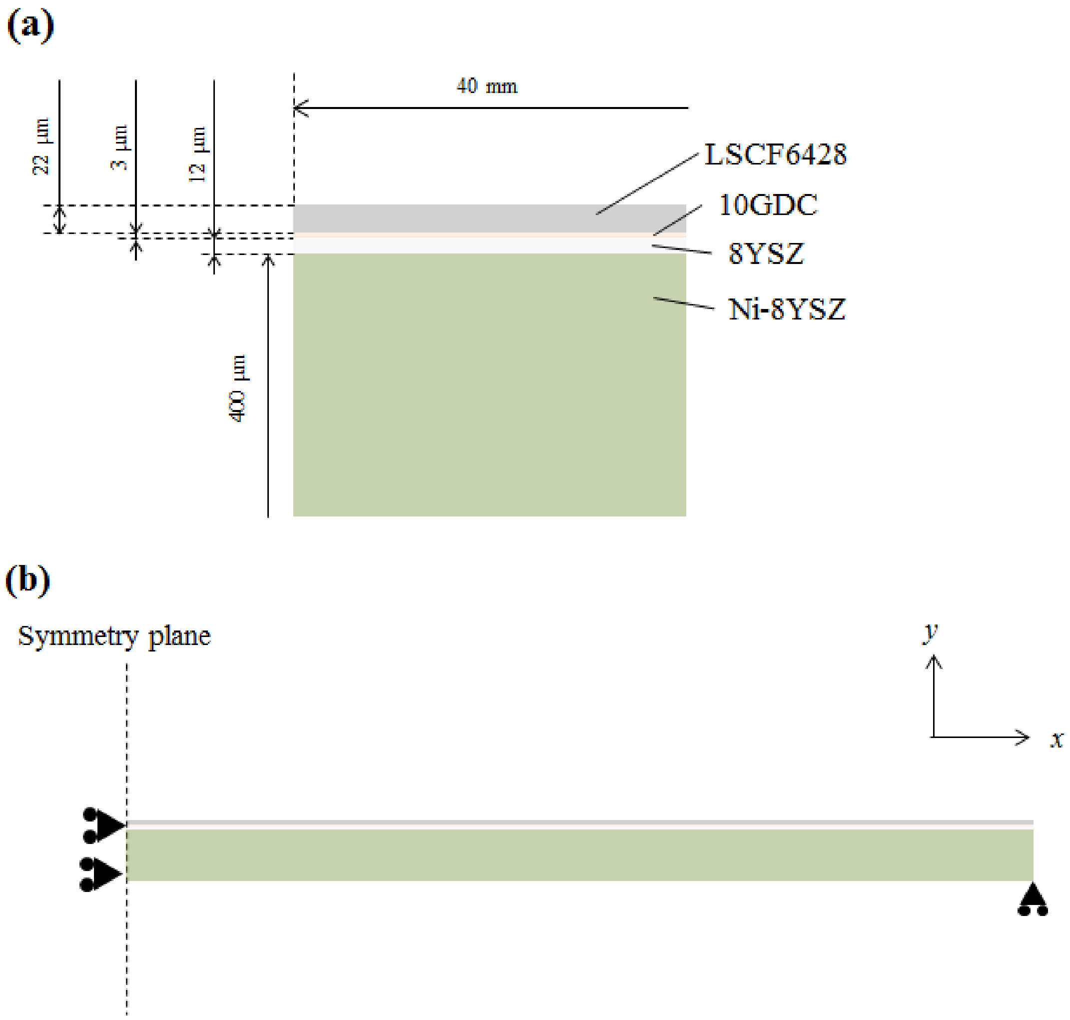

Fig. 5.9 (a) Components of the planer cell and (b) Boundary condition of the planer cell.

Figures 5.10 (a) and (b) show the contour plot of the displacement of the cell in *y*-direction in cases 1 and 2, respectively. The black solid line shows the original shape of the sample. In both cases, the displacement in *y*-direction was larger at the center of the cell and the cell was convexed upward. Figures 5. 11 (a)-(b) show the contour plot of the maximum and minimum principle stress in the cell in cases 1 and 2. In both cases, the tensile stress was generated in cathode layer and was almost uniformly distributed in the cathode layer. On the other hand, the electrolyte layer was exposed to a compressive stress and the compressive stress is also almost uniformly distributed in the electrolyte layer. Figure 5.12 (a) and (b) show the tensile stress and the displacement at the center of the cell (upper left corner of the model) in *y*-direction as a function of temperature in case 1 and 2, respectively. In case 2, the tensile stress linearly increased with decreasing temperature, while it non-linearly increased with decreasing temperature in case 1. Over the whole temperature range, the tensile stress in case 2 was larger than that in case 1. The difference between both cases was most significant at around 473 K. At this temperature, the tensile stress in case 2 was almost two times larger than that in case 1. At room temperature, the tensile stress in case 2 was about 30% larger than that in case 1. The displacement in *y*-direction in case 1 was always larger than that in case 2 over the whole temperature range. At room temperature, the displacement in case 1 was almost 40% larger than that in case 2. Figure 5.13 shows the compressive stress at the center part of the electrolyte layer (left edge of the model) as a function of temperature in case 1 and 2. Over the whole temperature range, the compressive stress in case 2 was larger than that in case 1. However, the difference between these two cases was small. At room temperature, the compressive stress in case 2 was about 4 % larger than that in case 1. The above results suggest that the ferroelastic domain reorientation can affect the stress distribution in the planer cell and deformation of the cell. This effect is significant in the tensile stress in the cathode and deformation of the cell, while the ferroelastic domain switching does not have the large influence in the compressive stress in the electrolyte.

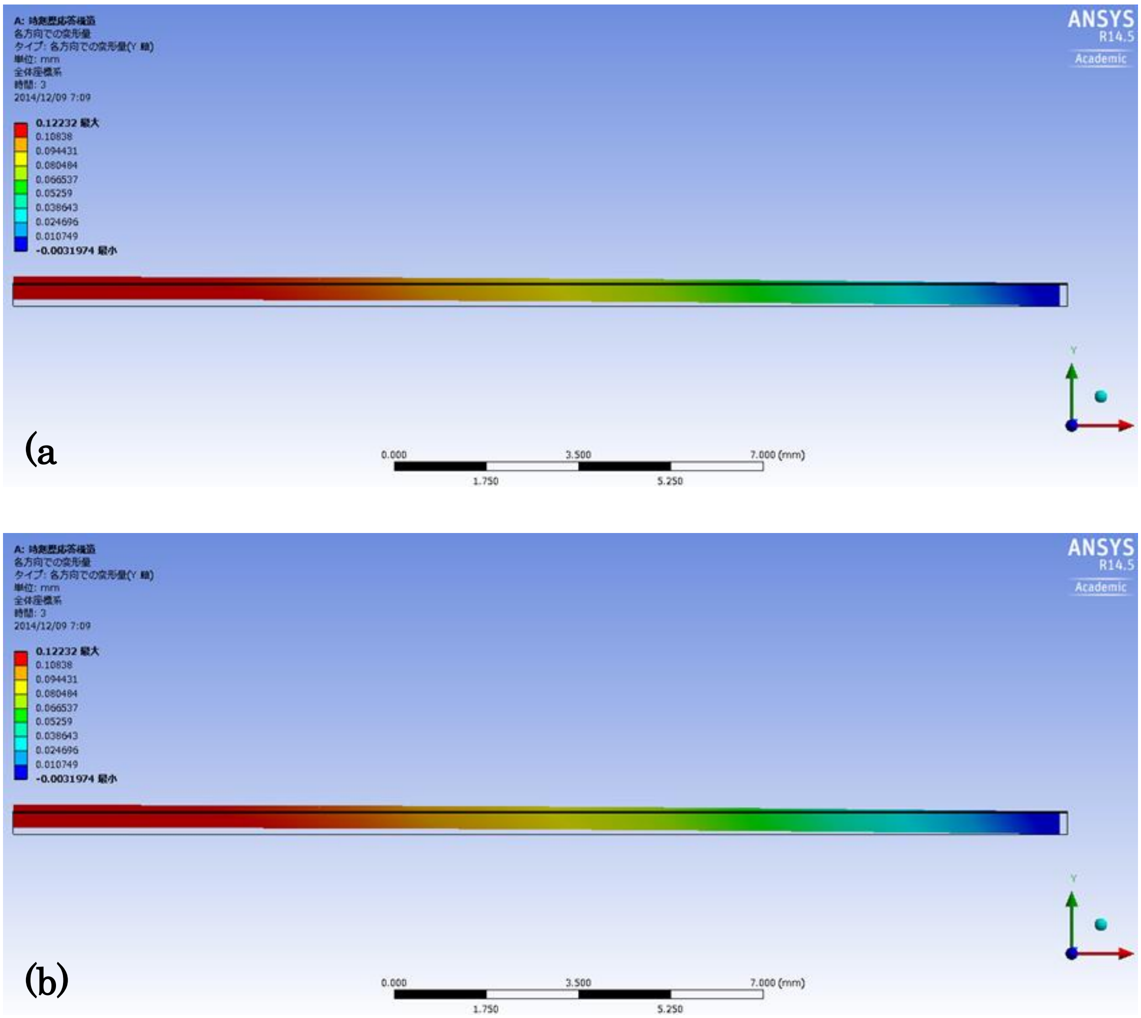

Fig.5. 10 Contour plot of the displacement of the cell in *y*-direction (a) in case 1 and (b) in case 2.

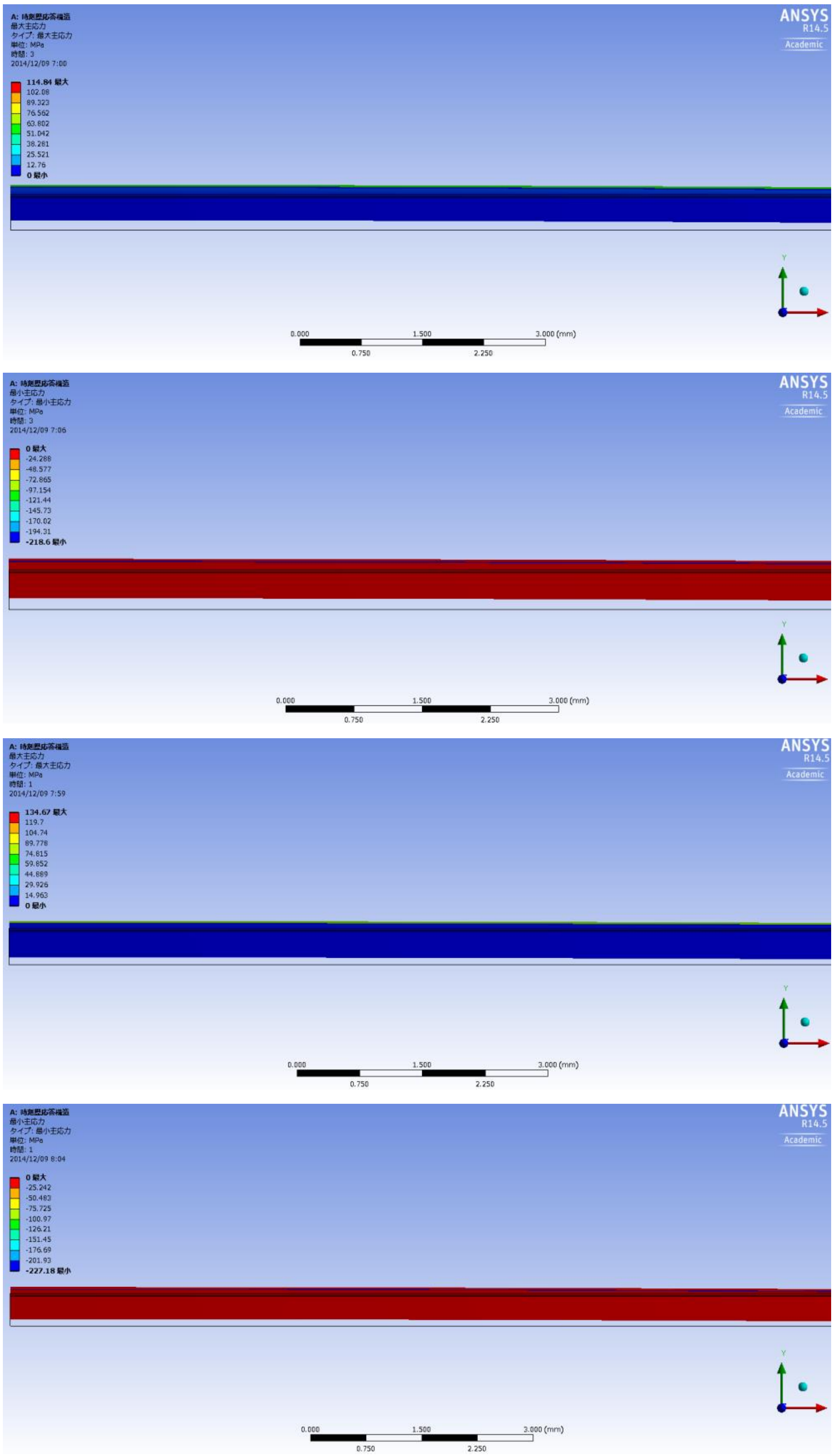

Fig. 5.11 Contour plot of (a) maximum principle stress in case 1, (b) minimum principle stress in case 1, (c) maximum principle stress in case 2, and (d) minimum principle stress in case 2.

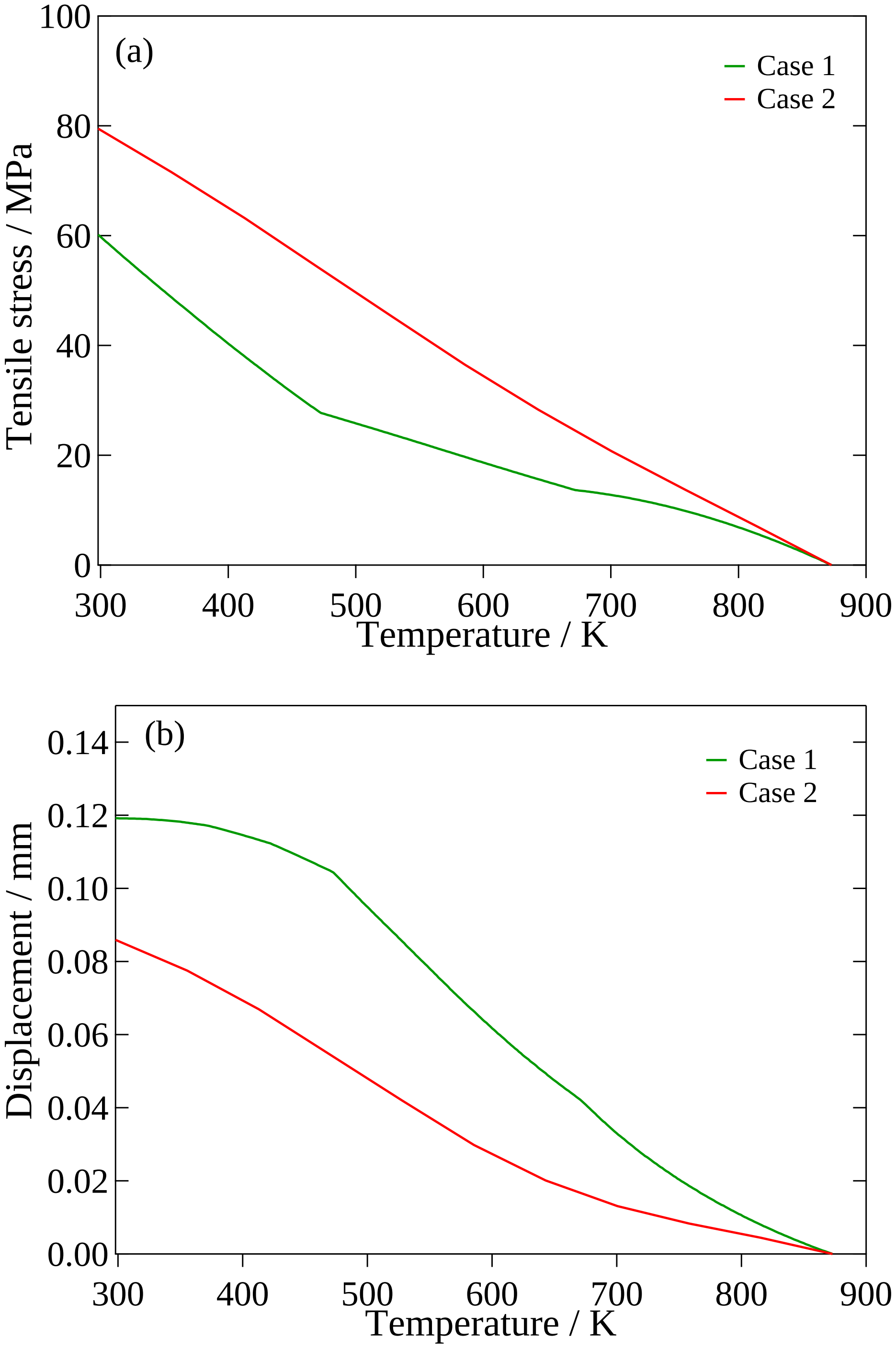

Fig. 5.12 Tensile stress and displacement at the center of the cell (upper left corner of the model) in *y*-direction as a function of temperature in case 1 and 2.

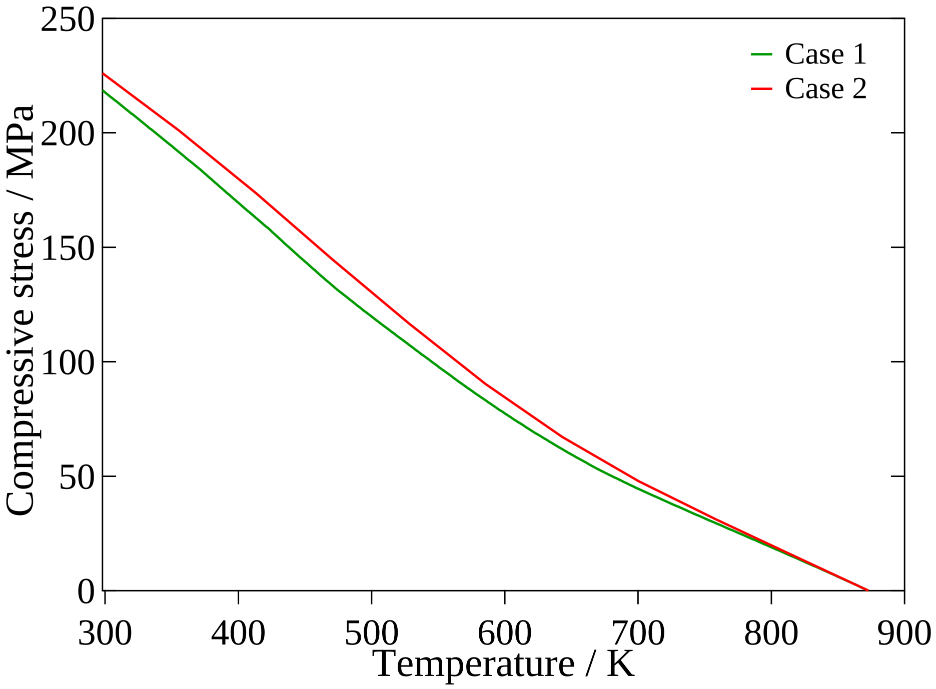

Fig. 5. 13 Compressive stress at the center part of the electrolyte layer (left edge of the model) as a function of temperature in case 1 and 2.

5.4 Conclusion

Two cases of simulations were performed in order to separately examine the influence of the change in the defect concentration and the domain switching on the stress distribution in the energy conversion devices.

In one simulation, the stress distribution in a simple planer SOFC cell was calculated, considering the $P(O_2)$ dependence of the mechanical properties of LSCF6428. It was suggested that the $P(O_2)$ dependence of the mechanical properties of LSCF6428 had no significant influence on the stress distribution in a SOFC cell. This is because the $P(O_2)$ dependence is not great at 873 and 1073 K. Although the Young's modulus of LSCF6428 becomes significantly larger with decreasing $P(O_2)$ at 973 K, the Possion's ratio also decreases with decreasing $P(O_2)$. Therefore, the effective biaxial elastic modulus does not greatly depend on $P(O_2)$ at 973 K.

In another study, the ferroelastic behavior of LSCF6428 was described by shape memory effect model (SME) and the stress distribution in a simple planer cell with LSCF cathode was calculated by ANSYS. The SME model could well reproduce the results of the uniaxial compression tests and the thermal cycle. The simulation of stress distribution in a simple SOFC planer cell suggests that the ferroelastic domain switching can relax the tensile stress in the cathode and lead to larger deformation of the cell but does not have a strong influence on a compressive stress in the electrolyte.

5.5 References

[1] H. Yakabe, T.Ogiwara, M. Hishinuma, and I. Yasuda, *J. Power Sources*, **102**, 144 (2001).

[2] H. Yakabe and I. Yasuda, *J. Electrochem. Soc.*, **150** (1), A35 (2003).

[3] A. Nakajo, Z. Wuillemin, J. V. Herle, and D. Favrat, *J. Power Sources*, **193**, 203 (2009).

[4] L. K. Chiang, H.-C. Liu, Y.-H. Shiu, C.-H. Lee, and R.-Y. Lee, *J. Power Sources*, **195**, 1895 (2010).

[5] A. Atkinson, *Solid State Ionics*, **95**, 249 (1997).

[6] Y. Fujimaki, To be published.

[7] S. B. Adler, J. A. Lane, and B. C. H. Steele, *J. Electrochem.*, **143**, 3554 (1996).

[8] L. B. Freund, *J. Crys. Growth*, **132**, 341 (1993).

[9] L. B. Freund, *J. Mech. Phys. Solids*, **44**, 723 (1996).

[10] S. Hashimoto, Y. Fukuda, M. Kuhn, K. Sato, K. Yashiro, and J. Mizusaki, *Solid State Ionics*, **186**, 37 (2011).

[11] T. Kushi, K. Sato, A. Unemoto, S. Hashimoto, K. Amezawa, T. Kawada, *J. Power Sources*, **196**, 7989 (2011).

[12] K. Eguchi, *Development of Solid Oxide Fuel Cells*, p. 149, CMC Press, Tokyo, 2005.

[13] H. Kitahara, *Mechanical Properties of Anode Materials Based on Ni-YSZ in Solid Oxide Fuel Cells Operating Conditions*, Master thesis, Graduate School of Engineering, Tohoku University, (2011).

[14] M. Pihlatie, A. Kaiser, and M. Mogensen, *J. Eur. Ceram. Soc.*, **29**, 1657 (2009).

[15] F. Tietz, F.J. Dias, B. Dubiel, H.J. Penkalla, *Mater. Sci. Engng.*, **B68**, 35 (1999).

[16] A. C. Souza, E. N. Mamiya, and N. Zouain, *Eur. J. Mech. A/Solids*, **17**, 789 (1998).

[17] F. Auricchio and L. Petrini, *Int. J. Numer. Meth. Engng.*, **61**, 807 (2004).

[18] F. Auricchio, S. Morganti, A. Reali, and M. Urbano, *J. Mater. Eng. Perform.*, **20**, 712, (2011).

[19] S. Watanabe, T. Miyasaka, S. Sukinou, K. Amezawa, T. Kawada, K. Sato, T. Hashida, *“ Effect of temperature on the mechanical properties of Ni/NiO-YSZ cermets for SOFC anodes”*, JSME Tohoku, Presentation No.178, Sendai Japan, 13/3/2012.

[20] S. Wang, M. Katsuki, T. Hashimoto, and M. Dokiya, *J. Electrochem. Soc.*, **150** (7), A952 (2003).

[21] B. X. Huang, J. Malzbender, R. W. Steinbrech and L. Singheiser, *Solid State Ionics*, **180**, 241 (2009).

Chapter 6

General conclusion

In this thesis, the mechanical properties of perovskite and related oxides for energy conversion devices are evaluated at high temperatures and under controlled atmospheres.

In chapter 2, the Young's and the shear moduli, the internal friction, and the Poisson's ratio of La_2NiO_4 (LN214), $La_{0.6}Sr_{0.4}CoO_{3-\delta}$ (LSC), $La_{0.6}Sr_{0.4}Co_{0.8}Fe_{0.2}O_{3-\delta}$ (LSCF6482), $La_{0.6}Sr_{0.4}Co_{0.2}Fe_{0.8}O_{3-\delta}$ (LSCF6428), and $La_{0.6}Sr_{0.4}FeO_{3-\delta}$ (LSF) were evaluated as a function of temperature under a constant $P(O_2)$ of $1 \text{ x } 10^{-1}$ or $1 \text{ x } 10^{-4}$ bar by using the resonance method and the small punch tests. Whereas the Young's and the shear modulus of LN214 monotonically decreased with increasing temperature and the internal friction was very small, the Young's and the shear moduli of LSCF significantly decreased with increasing temperature at lower temperatures and drastically increased at intermediate temperatures. The Young's modulus of LSC, LSCF6482, and LSF gradually decreased with increasing temperature at further higher temperatures. The abrupt change in the Young's and the shear moduli of LSCF at intermediate temperatures is considered to be associated with the phase transition. The abrupt change in the Young's and the shear moduli were phenomenologically explained based on the polynominal Gibbs free energy and the coupling theory.

In chapter 3, the Young's and the shear moduli and the Poisson's ratio of $La_{0.6}Sr_{0.4}Co_{0.2}Fe_{0.8}O_{3-\delta}$ (LSCF6428) and $La_2NiO_{4+\delta}$ (LN214) were evaluated as a function of $P(O_2)$. The Young's and the shear moduli of LSCF6428 showed a different $P(O_2)$ dependence in response to temperature. The $P(O_2)$ dependence was qualitatively explained by complex influences of the phase transition, the chemical expansion and the variation of the oxygen nonstoichiometry and the cation mean valence. On the other hand, the mechanical properties of the Young's and the shear moduli of LN214 were almost independent of $P(O_2)$. This is possibly because the decrease in the amount of excess oxygen atoms leads to the decrease in the elastic constant C_{33} and simultaneously the increase in the elastic constants, C_{11} and C_{22}. Therefore, the Young's modulus and the shear modulus is not macroscopically influenced by the change in the amount of excess oxygen atoms.

In chapter 4, the stress-strain relationship of LSC, LSCF6428 and LSF was evaluated by the uniaxial compression tests in the temperature range between room temperature and 1173 K. Also, the dynamic amplitude dependence of the Young's modulus and the internal friction of LSCF6428 and LN214 was evaluated. Further, the temperature dependence of the dynamic Young's modulus and of the internal friction of LN214, LSCF6428, and LSGM was investigated by using the technique of dynamic mechanical analysis. From the above measurements, it was found that the elastic modulus of ferroelastic perovskite oxides was strongly influenced by the ferroelastic domain switching. It is possible that the drastic decrease in the Young's modulus of LSCF6428 observed in the resonance measurement at low temperatures is also associated with the ferroelasticity. Furthermore, it was suggested that the oxygen vacancies can influence the mechanical properties of LSCF even at low temperatures through the interaction with the ferroelastic domain walls.

In chapter 5, two cases of simulations were performed in order to separately examine the influence of the change in the defect concentration and the domain switching on the stress distribution in the energy conversion devices. It was suggested that the $P(O_2)$ dependence of the mechanical properties of LSCF6428 had no significant influence on the stress distribution in a SOFC cell. Further, the simulation of stress distribution in a simple SOFC planer cell suggests that the ferroelastic domain switching can relax the tensile stress in the cathode and lead to larger deformation of the cell but does not have a strong influence on a compressive stress in the electrolyte.

Through the work in this thesis, the mechanical properties of perovskite and related oxides at high temperatures and under controlled atmospheres were measured and the influence of oxygen defects and ferroelasticity on the mechanical properties was successfully evaluated. Although further work is necessary to obtain deeper understanding about the microscopic mechanisms through which the oxygen defects and ferroelasticity affect the mechanical properties, the author is confident that the results shown in this thesis contribute to both scientific and industrial fields. From the industrial point of view, this thesis provided the fundamental data of mechanical properties of perovskite and related oxides. Also this thesis proposed a methodology to evaluate the influence of oxygen defects and ferroelasticity on the stress distribution in the energy conversion devices. And from the scientific point of view, the methodology and the techniques to evaluate the mechanical properties used in this study are also valid to examine other functional materials.

Acknowledgement

First of all, I wish to express my gratitude to my supervisor Professor Tatsuya Kawada for his inspiration, excellent guidance and never-ending support during these three years. I am also very grateful to my co-supervisers Associate Professor Shin-ichi Hashimoto and Associate Professor Keiji Yashiro for all the encouragements, the positive attitude and the valuable comments on my work.

I would like to thank co-examiners of this dissertation, Professor Toshiyuki Hashida, Professor Hideaki Matsubara, and Professor Koji Amezawa for their comments and advice.

I would like to thank Emeritus Professor Junichiro Mizusaki, Associate Professor Kazuhisa Sato, Associate Professor Fumitada Iguchi, Assistant Professor Takashi Nakamura, Assistant Professsor Atsushi Unemoto, Mr. Satoshi Watanabe who always took care and helped my research activities.

I would like to acknowledge Professor Mari- Ann Einarsrud, Dr. Julian Tolchard, and Professor Tor Grande of Institute for Materials Technology, Norwegian University of Science and Technology for accepting me as a short-term exchange student, giving solid supports and precious comments.

I would like to acknowledge financial support from Japan Society for the Promotion of Science (JSPS) and GCOE program “World Center of Education and Research for Trans-disciplinary Flow Dynamics”.

I would like to acknowledge all the support from Environmental Leader Program, Graduate school of Environmental studies, Tohoku University.

I would like to thank current and former members of Kawada lab.. The present study would never be completed without their countless supports and valuable comments: Mr. Shin Yu-cheol, Mr. Riyan Achmad Budiman, Ms. Hyun-jin Hong, Mr. Zhao Fei, Ms. Xingwei Wang, Mr. Yuki Gonoi, Mr. Taiki Shindo, Mr. Hiroki Sato, Mr. Toshiki

Watanabe, Ms. Abhilasha S. Devaraj, Mr. Mirai Takeda, Mr. Issei Susuta, Mr. Yusuke Okamoto, Mr. Yasuaki Nakagawa, Mr. Dan Nonami, Mr. Hiroki Akabane, Mr. Shunsuke Noda, Mr. Kohei Shishido, Mr. Shun Hatakeyama, Mr. Takayasu Uchi, Mr. Junichi Sakuraba, Mr. Takaya Hoshi, Mr. Tenyo Zukawa, Mr. Rafael Moreira Garcia, Ms. Yuko Kawamura, Ms. Mie Sasaki and former members.

Finally, I would like to thank my friends and my family for their support and encouragement.

January, 2015 Yuta Kimura

List of Publications

Original Papers on the subject of This Study

Papers

1. Y. Kimura, T. Kushi, S. Hashimoto, S. Watanabe, K. Amezawa, T. Kawada, Y. Fukuda, A. Unemoto, K. Sato, K. Yashiro, J. Mizusaki, and T. Hashida, “Mechanical Properties of $La_{0.6}Sr_{0.4}Co_{1-y}Fe_yO_{3-\delta}$ under Various Temperatures and Oxygen Partial Pressures”, *ECS. Trans*, **35**(1), 2429 (2011).

2. Y. Kimura, T. Kushi, S. Hashimoto, K. Amezawa and T. Kawada, “Influences of Temperature and Oxygen Partial Pressure on Mechanical Properties of $La_{0.6}Sr_{0.4}Co_{1-y}Fe_yO_{3-\delta}$”, *J. Am. Ceram. Soc.*, **95**, 2608 (2012).

3. Y. Kimura, J. Tolchard, M.-A. Einarsrud, T. Grande, K. Amezawa, M. Fukuhara, S. Hashimoto and T. Kawada, “Anelastic properties of $La_{0.6}Sr_{0.4}Co_{1-\mathrm{y}}Fe_{\mathrm{y}}O_{3-\delta}$ at high temperatures”, *Solid State Ionics*, **262**, 337 (2014).

4. Y. Kimura, J. Tolchard, M.-A. Einarsrud, T. Grande, K. Amezawa, S. Hashimoto, and T. Kawada,” The Effect of Ferroelasticity of $La_{1-X}Sr_xCo_{1-Y}Fe_yO_{3-\delta}$ on the Mechanical Stability of Solid Oxide Fuel Cells”, *ECS Trans.*, **57**(1), 635 (2013).

5. Y. Kimura, K. Yashiro, S. Hashimoto, and T. Kawada, ” Ferroelastic Domain Reorientations and Its Influence on Mechanical Properties of $La_{0.6}Sr_{0.4}Co_{0.2}Fe_{0.8}O_{3-\delta}$”, *J. Electrochem. Soc.*, **161**(11), F3079, 2014.

Proceedings

1. Y. Kimura, T. Kushi, S. Hashimoto, S. Watanabe, K. AMezawa, T. Kawada, Y.

Fukuda, A. Unemoto, K. Yashiro, J. Mizusaki, K. Sato, and T. Hashida, “Effects of Temperature and Oxygen Partial Pressure on Mechanical Properties of $La_{0.6}Sr_{0.4}Co_{1-y}Fe_yO_{3-\delta}$“, *Proc. 8th International Conference on Flow Dynamics*, 734 (2011).

2. **Y. Kimura**, T. Kushi, S. Hashimoto, K. Yashiro, J. Mizusaki, K. Amezawa, and T. Kawada, “EFFECTS OF A PHASE TRANSITION AND OXYGEN NONSTOICHIOMETRY ON ELASTIC MODULUS OF $La_{0.6}Sr_{0.4}Co_{1-y}Fe_yO_{3-\delta}$,” *Proc. 13th Conference on Asian Solid State Ionics*, 235 (2012) .

Original Papers on the Related Subjects

1. T. Kawada, T. Masumitsu, **Y. Kimura**, S. Watanabe, S. Hashimoto, K. Yashiro, and K. Amezawa,” Transient shift of local oxygen potential in nonstoichiometric oxides upon application of mechanical stress”, *J. Electroceram.*, **32**, 78 (2014).

2. Y. Gonoi, **Y. Kimura**, K. Yashiro, S. Watanabe, S. Hashimoto, and T. Kawada, “Effect of Mechanical Stress on Oxygen Potential of Transition Metal Oxides”, *J. Electrochem. Soc.*, **161**(11), F3111, 2014.